Ultra-Wideband for Communications: Spatial Characteristics and Interference Suppression

Vivek Bharadwaj

Thesis submitted to the faculty of the
Virginia Polytechnic Institute and State University
in partial fulfillment of the requirements for the degree of

MASTER OF SCIENCE
In
Electrical Engineering

Dr. R Michael Buehrer (Chair)
Dr. Jeffrey H. Reed
Dr. Charles W. Bostian

April 21st 2005
Blacksburg, Virginia

Keywords: Ultra-wideband, spatial channel modeling, deconvolution, interference mitigation, antenna array, selection diversity

Ultra-Wideband for Communications: Spatial Characteristics and Interference Suppression

Vivek Bharadwaj

ABSTRACT

Ultra-Wideband Communication is increasingly being considered as an attractive solution for high data rate short range wireless and position location applications. Knowledge of the statistical nature of the channel is necessary to design wireless systems that provide optimum performance. This thesis investigates the spatial characteristics of the channel based on measurements conducted using UWB pulses in an indoor office environment. The statistics of the received signal energy illustrate the low spatial fading of UWB signals. The distribution of the Angle of arrival (AOA) of the multipath components is obtained using a two-dimensional deconvolution algorithm called the Sensor-CLEAN algorithm. A spatial channel model that incorporates the spatial and temporal features of the channel is developed based on the AOA statistics. The performance of the Sensor-CLEAN algorithm is evaluated briefly by application to known artificial channels.

UWB systems co-exist with narrowband and other wideband systems. Even though they enjoy the advantage of processing gain (the ratio of bandwidth to data rate) the low energy per pulse may cause these narrow band interferers (NBI) to severely degrade the UWB system's performance. A technique to suppress NBI using multiple antennas is presented in this thesis which exploits the spatial fading characteristics. This method exploits the vast difference in fading characteristics between UWB signals and NBI by implementing a simple selection diversity scheme. It is shown that this simple scheme can provide strong benefits in performance.

Acknowledgements

This thesis has been an enjoyable and rewarding experience. This was possible due to excellent backing and support from a variety of people.

First and foremost I wish to express my sincere gratitude to my advisor Dr. R Michael Buehrer. His guidance, patience and insight have been instrumental in shaping the end product. In addition to being a noble professor he is a splendid human being and I have been thoroughly enriched working under and knowing him. I also thank Dr. Jeffrey H. Reed and Dr. Charles W. Bostian for serving on my committee and providing helpful comments and corrections that have enhanced this work immensely.

My colleagues at MPRG have responded with ready and quality assistance on numerous occasions. Special mention goes to Brian Donlan with whom I conducted the measurement campaign and held many discussions with; Swaroop Venkatesh for help with the verification of the channel model; Jihad Ibrahim for suggesting the course of action for the theoretical framework in the interference diversity scheme; the omnipresent Chris Anderson, whose help and direction made the measurement process easier and David Mckinstry who tutored me on the basics at the outset.

My appreciation goes to the people at the Time Domain Labs at Virginia Tech for their help with the equipment and the staff at MPRG for ensuring a great working environment and running everything smoothly. Also to the motley group of roommates and friends whose wishes have contributed in its own special way.

Lastly, where would I be without the endless unconditional love from my parents, sister, grandparents and other family members all far away in India? They have been there for me every step of the way and their encouragement has been a significant factor in the completion of this thesis.

List of Acronyms

AOA	Angle of Arrival
BER	Bit error Rate
CDF	Cumulative distribution function
CDMA	Code division multiple access
CIR	Channel impulse response
DSO	Digital Sampling Oscilloscope
FCC	Federal Communications Commission
LOS	Line of sight
NBI	Narrowband band interference
NLOS	Non line of sight
OFDM	Orthogonal frequency division multiplexing
PDF	Probability distribution function
PRF	Pulse repetition frequency
PSD	Power Spectral Density
SINR	Signal to interference and noise ration
SIR	Signal to interference ratio
SNR	Signal to noise ratio
SOD	Set of Delays
TOA	Time of Arrival
UWB	Ultra Wideband
VNA	Vector network analyzer

Table of Contents

List of Figures

List of Tables

Chapter 1. Ultra-Wide Bandwidth (UWB) Systems

1.1 Background

In recent years, Ultra-wideband (UWB) signals have received significant attention for use in communications and ranging applications. UWB communications systems can be defined as wireless communications systems with a fractional bandwidth greater than 0.20 or a bandwidth greater than 500 MHz measured at the -10 dB points [Fow90]. Fractional bandwidth is defined as $B_f = 2\dfrac{f_H - f_L}{f_H + f_L}$ where f_H and f_L are the upper and lower -10 dB points of the signal spectrum respectively. The center frequency of the transmission is defined as $(f_H + f_L)/2$. Traditional communications systems typically use signals having a fractional bandwidth less than 0.02.

On February 14, 2002, the United States Federal Communications Commission (FCC) adopted the First Report and Order [FCC02] that permitted the marketing and operation of certain types of new products incorporating UWB signals. A band for UWB from 3.1 GHz – 10.6 GHz was allotted and two different spectral masks for UWB systems were provided for indoor handheld devices and outdoor devices as shown in Figure 1-1. The mask is required to provide protection to existing narrowband/wideband services that co-exist in the spectrum allotted for UWB.

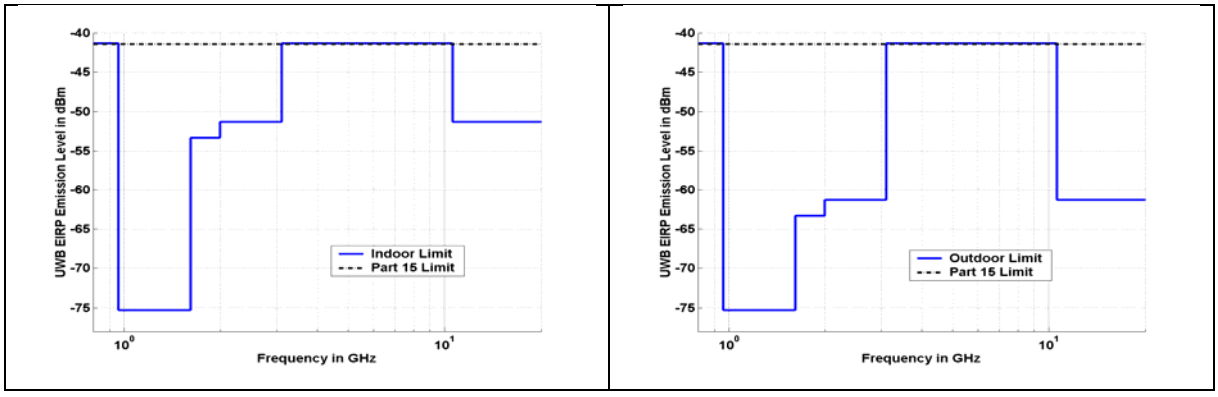

Figure 1-1 UWB spectral mask for indoor and outdoor UWB applications

The potential advantages of UWB include:

1. A wide bandwidth means more resolvable multipath and greater frequency diversity (i.e., greater resistance to multipath fading).
2. Due to the low power spectral density (PSD) in conforming to the FCC specifications the probability of detection/intercept is low.
3. The fine time resolution allows for greater precision in position location and radar type applications.
4. Co-existence with existing narrowband and wideband services which potentially leads to greater overall spectral efficiency.

Since the FCC specification does not impose any restriction on the approach used to generate and transmit the UWB signal, different methods have been proposed for utilizing the available UWB spectrum. The two main techniques (in terms of current standardization efforts) are:

1. Multi-band orthogonal frequency division multiplexing (OFDM)
2. Impulse radio (or direct sequence spread spectrum)

In the multi-band OFDM approach, a 500MHz OFDM signal hops between multiple frequency bands for an overall spectral occupancy of a few GHz. Multiple users are supported by providing them with different hopping patterns. [Bat03] [Kum04]. OFDM is a mature and well developed technology and the multi-band standardization approach has spawned from OFDM development efforts.

Impulse Radio involves the use of extremely short (sub-nanosecond) pulses to transmit information [Scho97]. The pulse generates a very wide instantaneous bandwidth signal according to the time scaling properties of the Fourier transform relationship between time and frequency. Information is sent by modulating the pulses in the time domain. These pulses typically resemble a Gaussian function or one of its derivatives. They may also be multiplied by a sinusoid to obtain a 'Gaussian modulated sinusoid'. This is typically done to ensure that the signal energy is within the allocated UWB band.

Modulation of these pulses can be achieved in many ways.

1. Varying the amplitude of the pulse (pulse amplitude modulation)
2. Positioning the pulse at different instances of time (pulse position modulation)
3. Changing the polarity of the pulse (bi-phase Modulation)

4. Combination of the above techniques for higher order schemes.

The different modulation schemes have been discussed in [Mck03a][Kum04].Bi-phase modulation is used in most of the simulations presented in this thesis and will be discussed briefly. It is similar to BPSK modulation except that in this case the change of 'phase' is accomplished by flipping the transmitted pulse to indicate a '0' or a '1'. This is illustrated in Figure 1-2. Only 1 bit of information is carried by the pulse in this scheme. Since this is an antipodal modulation scheme, the probability of error is identical to BPSK i.e. $P_e = Q\left(\sqrt{\frac{2E_b}{N_o}}\right)$ where E_b is the energy in one UWB bit and $N_o/2$ is the noise Power Spectral Density. As compared to other binary modulation schemes, Bi-phase offers the best energy efficiency [Wel01].

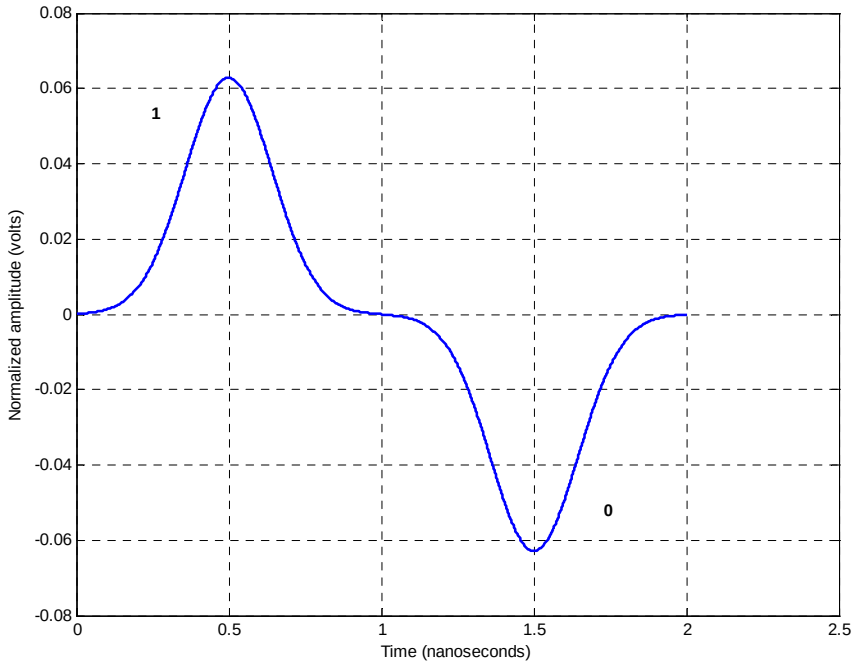

Figure 1-2 Normalized Amplitudes of the Bi-phase modulated UWB pulse when '1' and '0' are sent. Note that the diagram is just a representation of the voltage waveform seen in the output terminals of the Digital Sampling Oscilloscope.

Typically one information bit may be spread over multiple pulses in a manner similar to repetition coding to improve the energy per bit of the received signal (i.e., since the

power is limited by the FCC, additional energy can only be obtained by integrating over a longer duration.) The Pulse Repetition Frequency (prf) is the rate at which pulses are transmitted, i.e. number of pulses per second. The prf affects the interference UWB signals cause to other narrowband and wideband systems.

In order to accommodate many users in the system, both time-hopping and direct sequence spreading have been proposed for UWB. In time-hopping impulse radio [Scho98] the pulse position of each user's data is pseudo-randomly shifted at each pulse period. The modulation due to the data stays the same for multiple pulses. Each user is given a unique code which is used to identify transmission from that particular user. In direct sequence UWB [Foer02c], [Ham 02] one data bit is spread over multiple pulses, where the number of pulses represents the amount of repetition of the data.

One of the most common receiver structures for UWB (or spread spectrum) signals is the Rake receiver. A Rake receiver collects energy from the multipath components of the channel by using multiple correlators (called 'fingers') each tuned to a specific time delay. Each finger of the Rake receiver corresponds to a resolvable multipath component that can be collected. In the case of UWB, due to the fine time resolution of the pulses, a large number of resolvable multipath components arrive at the receiver, thus providing a kind of 'time diversity' which can be exploited by a Rake receiver. While Rake receiver structures for conventional wideband systems has been dealt with extensively in literature, its application specific to the UWB domain is a little more complicated due to the smaller pulse widths. Different receiver structures for UWB based on the Rake receiver have been proposed [Win02].

The spectral properties of UWB signals depend on the pulse waveform as well as the width of the pulse. Additionally, the antennas modify the shape of the generated pulse and its effect can often be modeled as a differentiation operation. Hence the pulse waveforms in the channel are typically first derivatives of the generated pulse. Figure 1-3 shows the Gaussian pulse and its various derivatives. For maximum SNR at the receiver, it is highly desirable to correlate the received pulse with a pulse shape that incorporates the distortion due to the transmit and receive antennas.

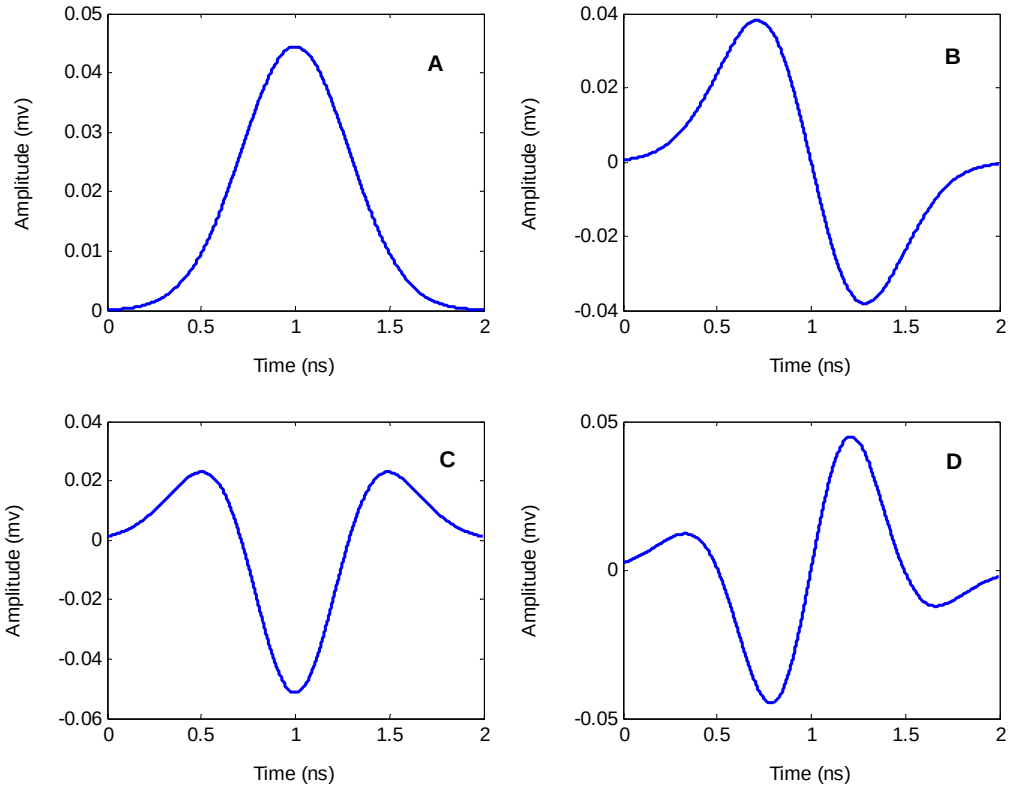

Figure 1-3 The Gaussian pulse (A) and its derivatives

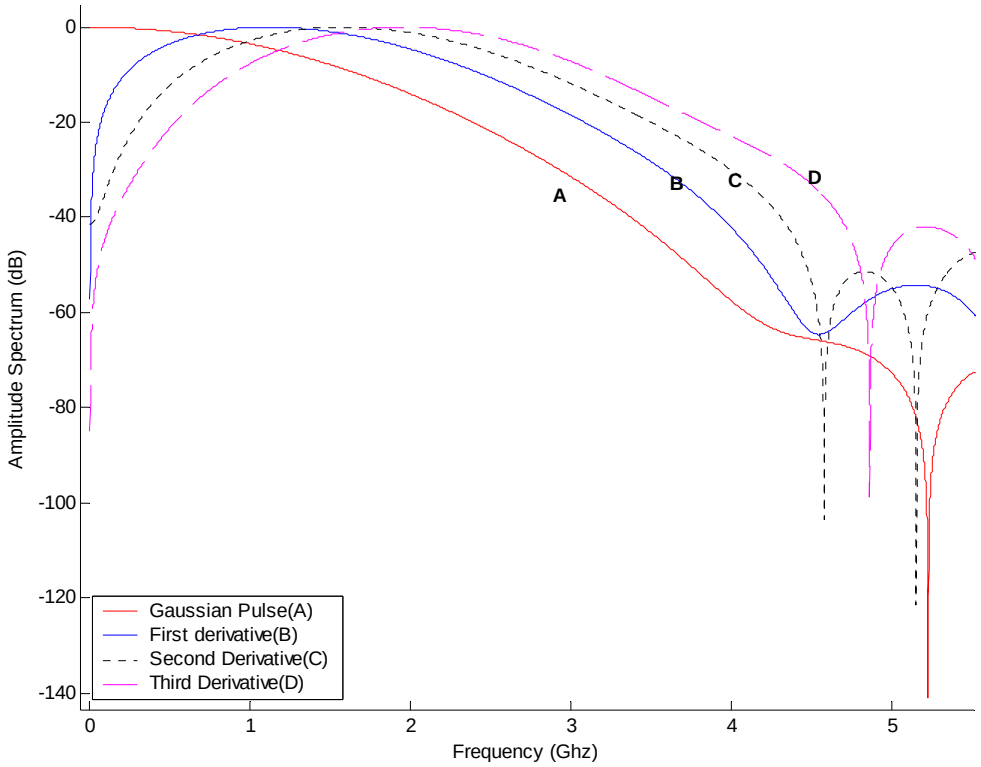

Figure 1-4 Spectra of the various pulses

It can be seen from Figure 1-4 that the center frequency of the pulse increases with higher-order derivatives of the pulse. However the shape of the spectra remains roughly the same. Reference [Ham02] suggests the use of the Gaussian doublet which essentially consists of 2 Gaussian pulses of opposite polarity separated in time. This introduces nulls in the spectrum, the frequency of which can be changed by varying the separation between the pulses. This property can be used to avoid interferers at certain frequencies.

Various applications involving the use of UWB have been proposed. UWB has been popular with the radar community for many years. References [Tayl95] [Tayl00] provide a wealth of information on UWB radar. The wide bandwidth of the signal (due to the narrow pulse-widths) provides fine resolution (and consequently accurate ranging) and makes UWB signals desirable for applications such as radar and position location. Additionally, information about the channel can be gleaned by observing distortions in

the pulse shape and the delays between the resolvable multipath components. Through-the-wall-motion-detection and ground-penetrating radar are other examples of proposed non-communication applications that utilize this characteristic which is not enjoyed by traditional communication signals based on sinusoidal carriers. The wide bandwidths give rise to immense possibilities in high data rate applications like wireless USB. The current UWB standard proposal [Bat03] supports data rates as high as 480 Mbps. Additionally low data rate applications like sensor networks, tactical communications, etc., can use UWB as the physical layer.

The advent of UWB communications brings with it new challenges in designing complete communication systems. Some areas of research (such as the ones listed below) have been thoroughly invigorated with the recent interest in UWB communications.

- *Channel Characterization efforts:* Traditional channel models typically cannot be applied to UWB signals which span a wide range of frequencies. A lot of effort is focused on obtaining easy to use channel models that can be used in simulations of end-to-end UWB systems.
- *Receiver Design:* Indoor UWB channels are typically characterized by rich multipath environments. UWB pulses typically face frequency distortion due to the channel and the antennas. Developing Rake receiver structures that are able to achieve near perfect correlation is an exciting area of research.
- *Interference Analysis and Cancellation:* The wide bandwidths and low energy per pulse makes UWB systems prone to interference from other narrowband systems. Techniques to avoid and/or mitigate interference caused by these systems is also a an area that needs further investigation

1.2 Thesis Organization

This thesis investigates spatial characteristics of UWB signals based on a large set of indoor measurements and generates a statistical channel model that includes spatial characteristics. A scheme to exploit the spatial characteristics to mitigate Narrow Band Interference (NBI) is also presented.

In Chapter 2, the UWB indoor measurement campaign at MPRG is detailed. The measurements were based in the time domain using a sampling oscilloscope and two

different baseband pulse generators. Much of the channel characterization work presented in this thesis is drawn from this measurement data. The measurements are processed using a two-dimensional deconvolution technique based on the Sensor-CLEAN algorithm [Cram02a]. A brief analysis of this algorithm is presented in this chapter.

In Chapter 3, the spatial characteristics of the UWB channel are investigated based on the obtained measurements. Understanding the spatial characteristics of the UWB channel facilitates the development of the space-time channel model. Energy distributions and amplitude statistics of the UWB signal are specifically investigated. Based on these results and intuitive observations, a spatial channel model for UWB communications is presented. This statistical model incorporates the Time-of-Arrival (TOA) and the Angle-of-Arrival (AOA) information in a joint model. The veracity of the model is verified using spatial and temporal correlation statistics.

In Chapter 4, a simple narrow band interference (NBI) mitigation scheme for UWB signals using multiple receive antennas is introduced. The low spatial fading characteristic of UWB signals is exploited to select the signal with the lowest power in an antenna array. The distribution of the Signal-to-Interference Ratio (SIR) at the receiver is obtained and the performance improvement of the scheme in mitigating NBI is demonstrated through BER simulations.

Chapter 5 presents conclusions. Some potential issues for further study are highlighted and the original contributions of the thesis are presented.

Chapter 2. UWB Channel Measurements and Processing

In a wireless system the mechanisms governing radio wave propagation are complex and varied. They are typically characterized by reflections, diffractions and scattering. Reflection occurs when the propagating electromagnetic wave impinges upon an obstruction with dimensions much larger than its wavelength. Diffraction occurs due to the formation of secondary waves by Huygens's principle when there is an obstruction in the transmitter-receiver path. Finally, scattering takes place when energy is re-radiated in different directions due to the presence of objects whose dimensions are of the order of the wavelength of the propagating wave. The result of these interactions is the presence of many signal components or multipath signals at the receiver.

The design of communication systems requires a basic understanding of the channel. In other words, models that incorporate the major features of the channel under consideration are essential in order to enable the system designer to predict the performance of the system for various modulation and coding schemes and receiver structures. An inaccurate channel model leads to incorrect system performance predictions. The accuracy of the channel model is generally traded for complexity. The average system designer would prefer not to use a channel model which places a premium on computational complexity or one which is cumbersome to use.

Channel models are essentially divided into two groups. The first class consists of statistical channel models that statistically describe the impact of the channel on the transmitted signal. The simplicity and ease of use of such models is offset by their relative lack of accuracy compared with 'deterministic' models which attempt to comprehensively model electromagnetic interactions in the channel. This second class of models is however, extremely location specific, often unwieldy to use and required a large amount of information about the channel of interest. Channel models are also classified according to the type of the environment being modeled. Thus, the most common classifications include stationary indoor channel models, stationary outdoor channel models and mobile channels (outdoor and time varying) [Rapp02].

This thesis focuses on statistical channel models for indoor stationary channels. Stationary in this context means that the channel varies very slowly relative to the data rate. Furthermore, indoor channels are relatively short range (few meters to tens of meters) and are characterized by a large number of scattering objects.

While the subject of channels models for narrowband and wideband systems has received a significant amount of attention in the literature, channel models for UWB are still undergoing considerable refinement and it is still an exciting area of research. Efforts focusing on developing channel models pertinent to UWB signals have been detailed (amongst others) in [Cram02a][Win02][Mck03a].

Channel measurement techniques may be broadly classified as time domain and frequency domain techniques. In time domain measurement techniques, a pulse in the time domain is transmitted into the channel. The receiver typically consists of a digital sampling oscilloscope. In the frequency domain, channel measurements can also be performed using a vector network analyzer (VNA). The VNA performs a sweep of discrete frequency tones. The S-parameters of the wireless channel are calculated at each of the frequencies in the sweep. The different measurement techniques and the relative advantages and demerits of each technique are summarized in [Muq03].

This section briefly describes the UWB measurements conducted at MPRG by the author and Brian Donlan on the campus of Virginia Tech under the DARPA NETEX program [DARP04]. Much of the results and observations drawn in this thesis are based on the measurements detailed in this chapter.

2.1 Measurement procedure and setup

The primary purpose of the measurement campaign was to characterize the indoor channel with emphasis on office environments. Indeed, most of these measurements were performed in the MPRG offices at Durham Hall. Durham Hall is primarily constructed using steel reinforced concrete and cement block. The MPRG office consisted of metal cubicle partitions and either concrete walls or walls made of plaster wallboard. A better description of the measurement environment can be obtained from the measurement

campaigns conducted at the same location using different transmitter characteristics in [Muqa03][DARP04]

The measurement setup is shown in Figure 2-1

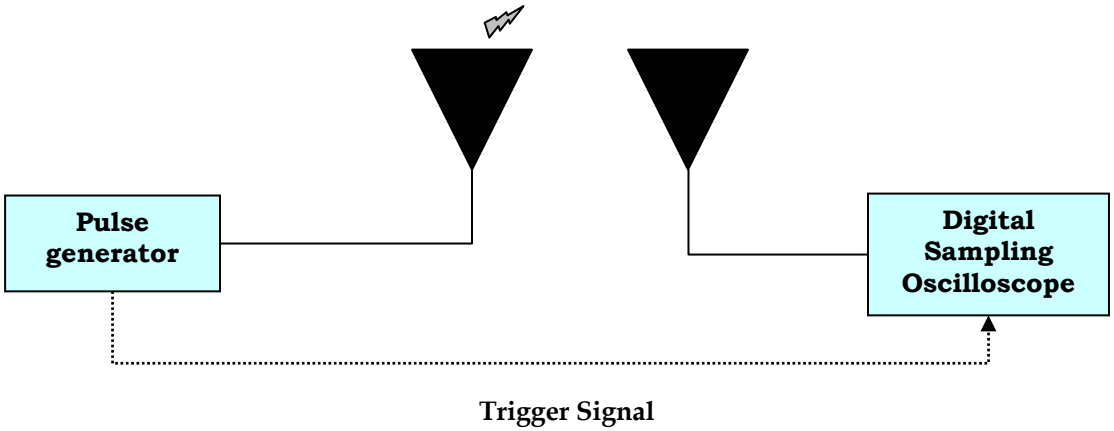

Figure 2-1 Simplified Block diagram of the measurement system

The transmitter was a *Picosecond Pulse Labs* pulse generator that generates two different pulses. The two different pulse shapes that were used to probe the channel in this work differed in the time duration and pulse shape. One generator created a 'trapezoidal' pulse with a width of approximately 2 ns. The second generator produced a 'Gaussian' pulse with a width of about 200 ps.

The receiver consisted of a *Tektronix CSA800* Digital sampling oscilloscope (DSO). The trigger signal from the pulse generator was used to synchronize the DSO to record the measurements. The SNR was improved through the use of averaging. Specifically, between 50 and 100 samples per record were used to reduce the impact of noise.

The antennas used were bi-conical antennas which are omni-directional in the azimuth plane. These antennas were characterized by the Virginia Tech Antenna Group and the antenna characteristics can be found in [Muq03].

The information about the pulse shapes used and the number of measurements taken are briefly summarized in Table 2-1.

Table 2-1 Information about pulse shapes used in measurements

Pulse type	Width (ps)	Number of locations	Measurements per location	Total number of measurements
Trapezoidal	2000	15	49	735
Gaussian	200	6[1]	49	294

In all 21 different Transmitter-Receiver location pairs were used. At each location, 49 different measurements were performed by moving the receive antenna over a 7 x 7 grid whose points were spaced 15 cm apart, as shown in Figure 2-2. The channel was assumed to be stationary while recording the measurements. Most measurements were performed during low activity periods including nights and weekends.

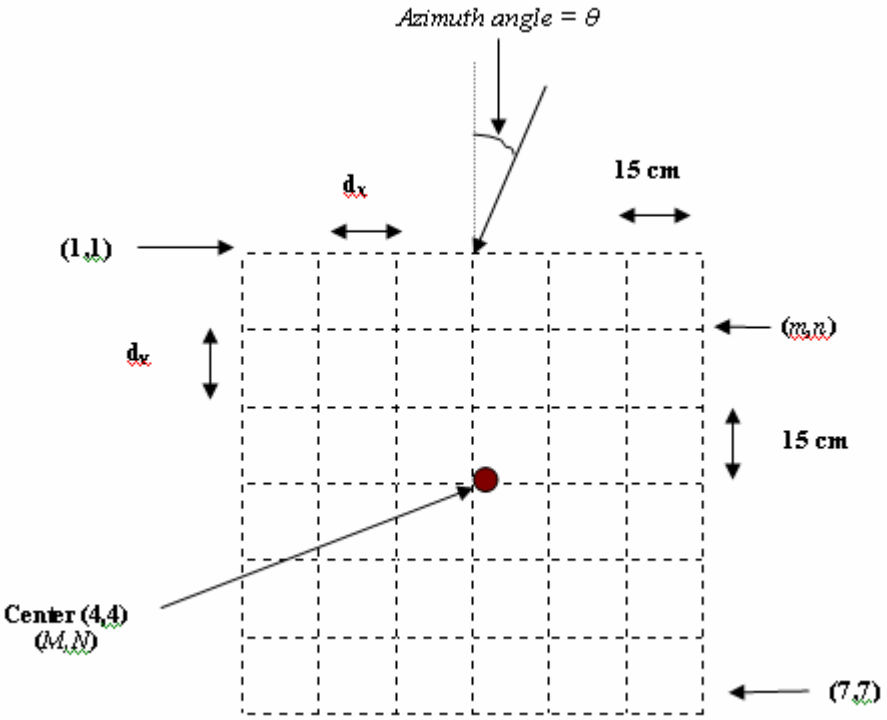

Figure 2-2 Measurement array of 7x7 positions

[1] Note that, for the Gaussian pulse there were additional measurements involving LOS locations and other specific measurements (e.g. only through concrete walls etc). For the purpose of developing the spatial channel model presented in Chapter 3, only the NLOS measurements (i.e. 6) have been considered.

The generated Gaussian pulse and its spectrum are shown in Figure 2-3 and Figure 2-4.

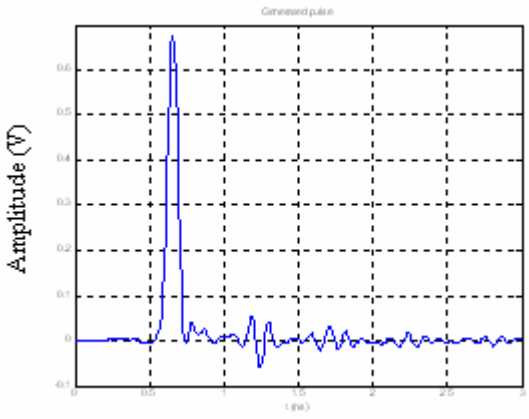

Figure 2-3: Generated Gaussian Pulse

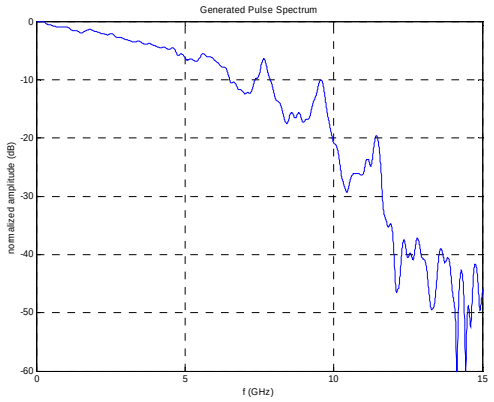

Figure 2-4: Generated Gaussian Pulse Spectrum

The received signal profiles were filtered in the time domain [Muq03] to reduce interference from undesired sources. The 3 db cutoff points for this filter were 0.1 GHz and 12 GHz. In addition there was a low frequency component (~30 MHz) generated by the pulse generator's internal circuitry which was picked up by the biconical antenna. This was also eliminated in the filtering process. Note that for the Trapezoidal profiles only the upper frequency cutoff of around 0.75 Ghz was used. This was done to avoid filtering out the significant passband energy of the Trapezoidal pulse, concentrated in the frequency span upto 500 MHz. Also the Gaussian pulse generator did not radiate a low frequency component.

2.2 Temporal Deconvolution

Temporal Deconvolution is the process of extracting the channel impulse response (CIR) from the received signal. This channel impulse response contains the information of the TOA of the different multipath components and their amplitudes. References [Mck03a][Yang04] provide some detailed information on various deconvolution techniques used and also a thorough description and analysis of the CLEAN algorithm, a widely used temporal deconvolution technique[Hogb74]. This

method involves the use of a LOS pulse to deconvolve the effects of the channel from the received signal. A reference measurement was performed outdoors to obtain a clean LOS pulse to be used in the deconvolution processes. The measured LOS pulse (voltage) at a distance of 1m when transmitting the Gaussian pulse using a Bicone antenna at the transmitter and the receiver is shown in Figure 2-5 while the spectrum of the received pulse is shown in Figure 2-7.

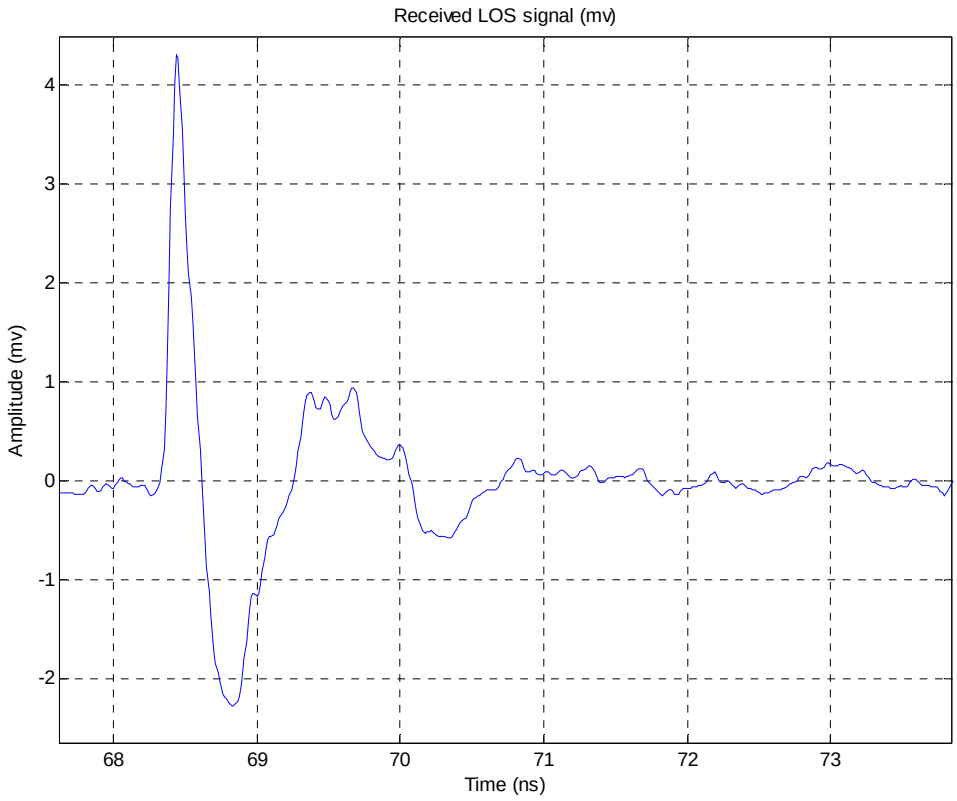

Figure 2-5: Received LOS pulse with Bicone Antenna (used for path loss and deconvolution)

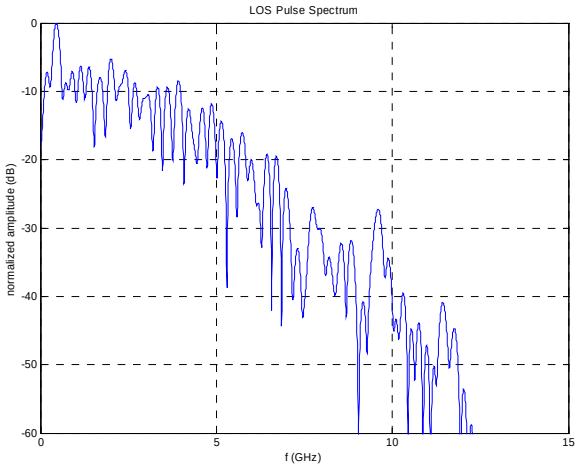

Figure 2-6 Received Gaussian Pulse Spectrum with Bicone Antenna

2.3 Spatial and Temporal Deconvolution

In indoor channels multipath components reach the receiver from all directions, (shown in Figure 2-7) each characterized by an angle-of-arrival (AOA). In order to use statistical models in simulating or analyzing the performance of systems employing spatial diversity combining, MIMO or other multi-antenna techniques, information about AOA statistics is required in addition to TOA information. In order to extract the AOA information from the spatial measurements, a variant of the Sensor-CLEAN algorithm [Cram02a] was used. The resulting AOA statistics are presented in Chapter 3 and used to develop a spatial channel model which is also described in Chapter 3.

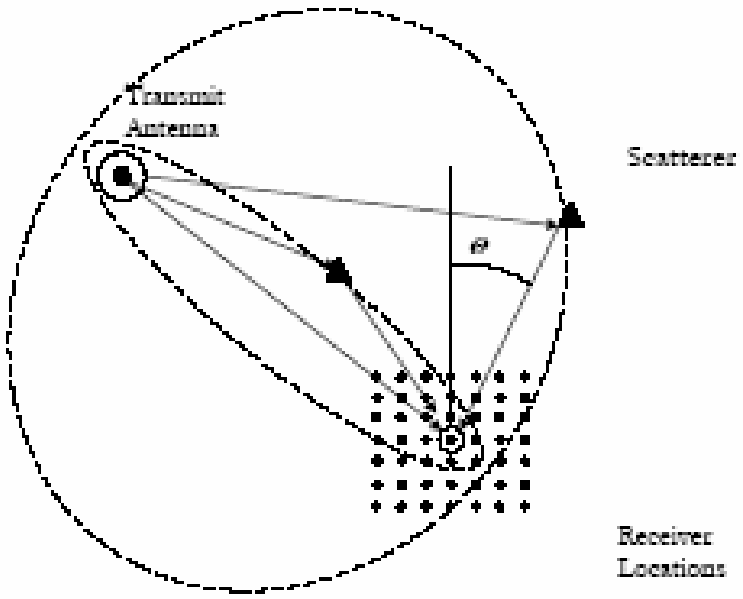

Figure 2-7 Transmitter, receiver and elliptical scatter model

2.3.(1) Sensor-CLEAN algorithm

The Sensor-CLEAN algorithm, given a grid of temporal measurements, produces a single CIR for each measurement location (assumed to be seen at the center of the grid), with each multipath component having an associated AOA. The algorithm is described in [Cram02a] to obtain the TOA and the AOA of multipath components from time domain measurements. In this thesis, some simplifications have been incorporated into the original algorithm. These simplifications were based on the test setup that was used to record the measurements. This is explained further in this section. The algorithm can be summarized using the following steps.

1. The input to the Sensor-CLEAN algorithm is the set of received signals in a local area using the same transmitted pulse. Also it is assumed that the channel remains static during the interval the measurements are recorded. The different steps towards obtaining

the TOA and the AOA are as follows. Note that the 'grid' in the ensuing text implies the measurement grid (in our case 49 points) used to take the measurements. This is shown in Figure 2-2

2. The TOA of a multipath component at a particular position on the grid is dependent on the orientation of that position in relation to the reference position *(M,N)* (i.e. 4, 4), the orientation of the grid with respect to the transmitter and the azimuth and elevation angles of the multipath component reaching the antenna situated on the grid.

3. Note that a bi-conical antenna was used in the measurement campaign. The gain of the antenna is essentially omni-directional in the azimuth plane and directional in the horizontal direction in the elevation plane. In other words the antenna is only omni-directional in the azimuth plane. Hence, it is assumed that the multipaths reaching the antenna all possess a 90° AOA in the elevation plane but differing AOA's in the azimuth plane. Depending on the AOA of the path the same multipath would reach a different position of the grid at different delays.

4. A set of delays (SOD) associated with every position in the grid is calculated for different reference angles in steps of 1 degree. This is evaluated only once and can be likened to a template waveform that is used in 1-dimensional CLEAN deconvolution [Mck03a]. To clarify, consider Figure 2-8 in which the delay associated with a path having a particular AOA at position (1,4) is $-x$ and with (7,4) is $+y$. This means that with reference to point (4,4) the multipath component arrives x samples earlier at (1,4) and y samples later at (7,4).

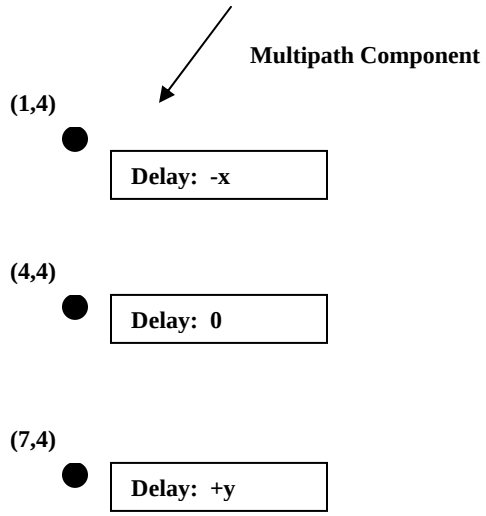

Figure 2-8. Illustration of delays at 3 different points on the grid

5. The delay t_d in seconds can be obtained from Equation (2.1).

$$t_d = (M-m)\frac{d_x}{c}\cos\theta + (N-n)\frac{d_y}{c}\sin\theta \tag{2.1}$$

In this equation M, N are the co-ordinates of the grid origin while m, n are the grid co-ordinates of the point under consideration. Note that equation (2.1) is valid as long as the grid positions are numbered as shown in Figure 2-2. Appropriate changes can be made in the equation for different grid orientations.

Figure 2-9, Figure 2-10 and Figure 2-11 denote a sample LOS measurement showing the shift in the signal at different points on the grid. It can be seen from the shift in the profiles that (1, 4) is closest to the transmitter and (7, 4) is the furthest away. If we select (4,4) as the reference point with zero delay (1,4) would have negative delay and (7,4) would have a positive delay value.

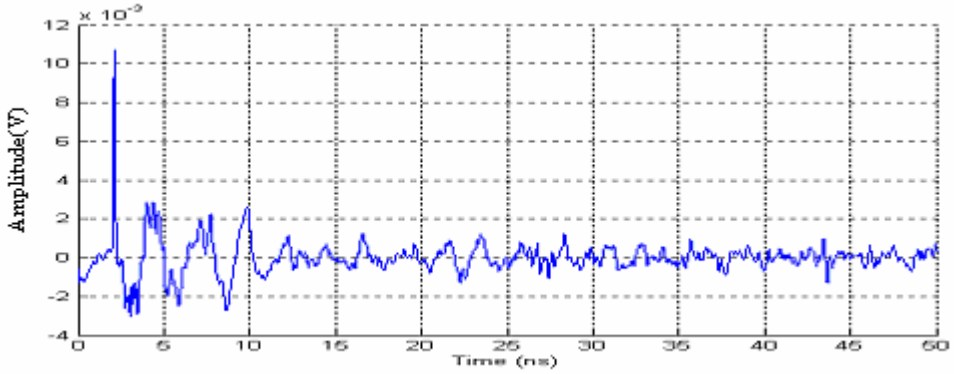

Figure 2-9 Sample LOS signal at (1,4)

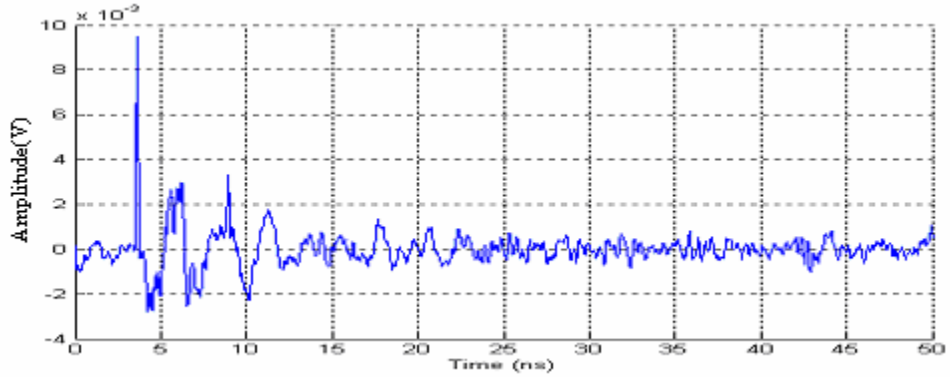

Figure 2-10 Sample LOS signal at (4,4)

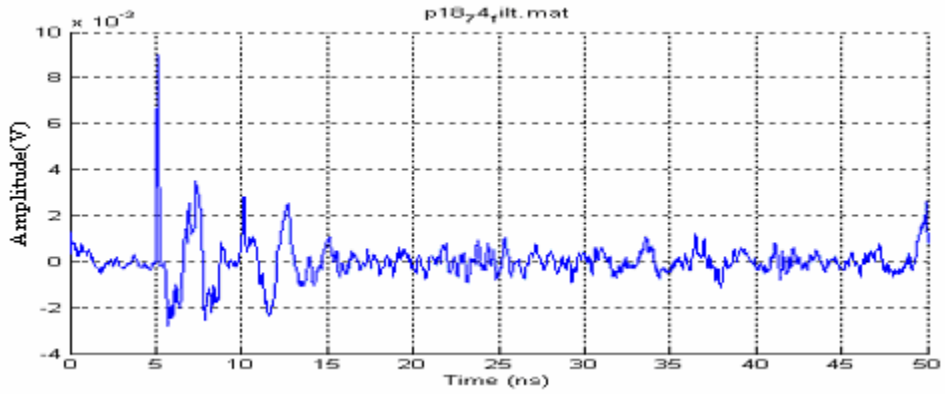

Figure 2-11 Sample LOS signal at (7,4)

6. For each AOA associated with the SOD, each of the 49 received signals are shifted equivalent to the delay indicated in the SOD. If the delay value is positive the signal is shifted left and vice versa if negative. The shifted signals are summed together and stored as the joint correlation outputs for that angle. This is calculated for each AOA in the SOD.

7. The maximum of the absolute value of the correlation matrix is identified. The TOA and the AOA of the identified joint correlation peak is stored and the amplitude of the component is calculated from the point (4,4) (the reference point) at that delay in the same manner as the 1-D CLEAN.

8. The delay and AOA are then translated to delays of each of the 49 points and subtracted. If the delay associated with that component is outside the permissible range it means that the multipath component was not included in the observation profile of that component. This occurs towards the end of the profile where components associated with certain locations would not have been captured in the given fixed observation time window.

9. The process is repeated until a threshold criterion in either the number of iterations or the minimum signal level is met. Note that due to errors in the measurements the Sensor-CLEAN algorithm can identify false paths, due to past correlation peaks not being removed completely. Thus, with respect to the CLEAN algorithm there is an increase in the number of paths generated with the Sensor-CLEAN. A flow diagram of the algorithm is shown in Figure 2-12

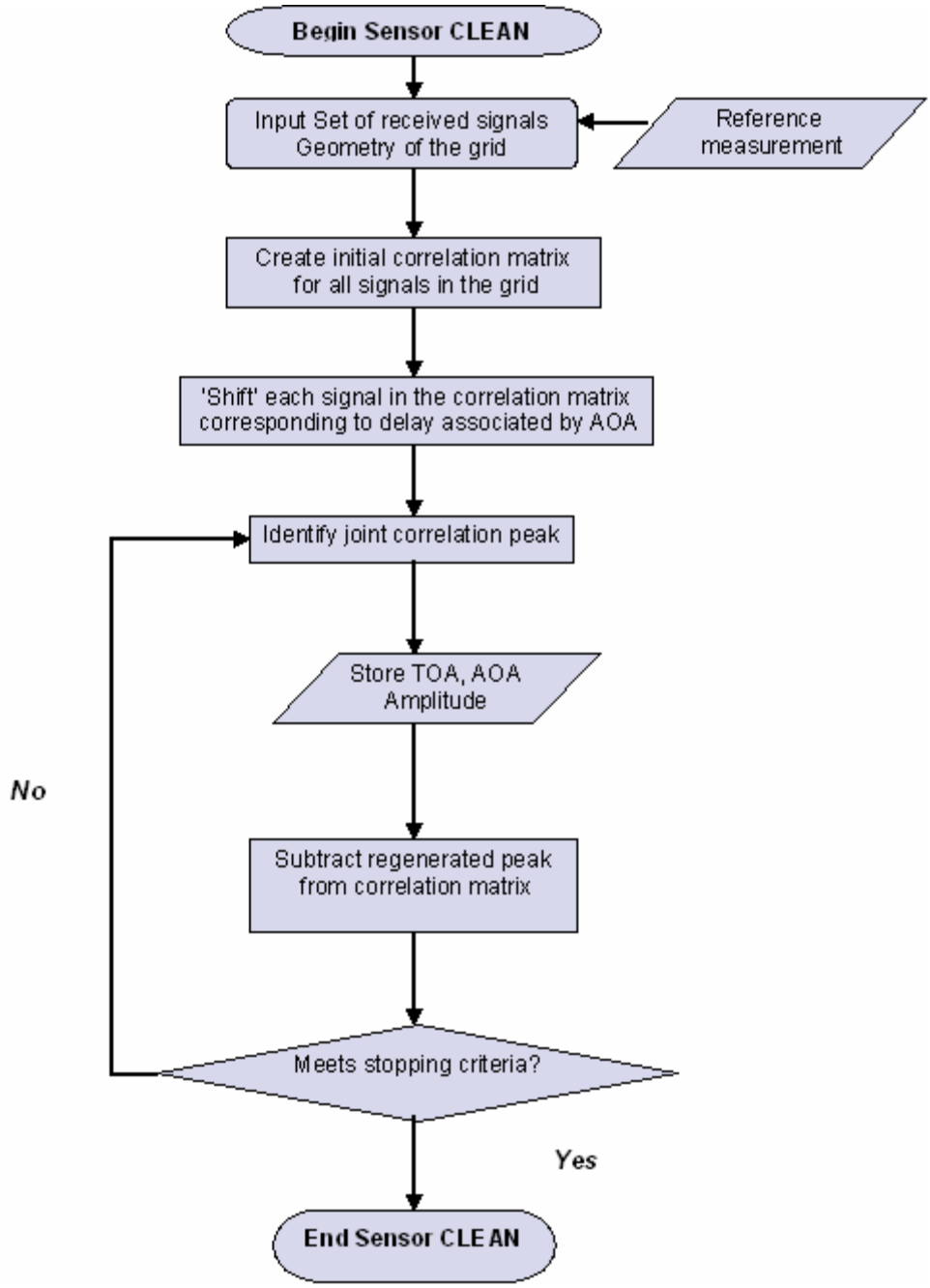

Figure 2-12 Flow diagram of the Sensor-CLEAN algorithm

2.3.(2) Evaluation of the performance of 2-D CLEAN

The performance of the Sensor-CLEAN algorithm was tested to verify its accuracy by applying it to known channels in the absence of noise. Two types of test channels were considered.

1. 2 path channel
2. Multiple path scenario

(i) Two path channel

In this scenario, a CIR containing 2 multipath components is generated for every position in the 7x7 grid shown in Figure 2-2 using knowledge of the distance between the grid points and the orientation of the grid with respect to the transmitter. The AOA of the first path is set to $0°$ in the Azimuth plane and $90°$ in the elevation plane while the AOA of the 2^{nd} path is kept at $90°$ in the Elevation plane and varied in the Azimuth plane. A set of 49 CIRs are obtained and convolved with the reference pulse. The result is a set of 49 received signals at each point in the 2-dimensional grid. The Sensor-CLEAN algorithm is applied to this array of signals and the CIR obtained through Sensor-CLEAN is compared to the original CIR at 4,4. Various cases are generated with different inter-path spacing and azimuth angle separations

Case 1: Temporal Separation > Half the Pulse Width

When the separation between the paths is greater than half a pulse width, both the TOA and AOA match their true values, irrespective of AOA separation between the multipath components as shown in Figure 2-13 and Figure 2-14. In short, the algorithm has no difficulty in identifying the paths (TOA and AOA) for any angular separation provided the two paths are separated temporally by more than half a pulse width.

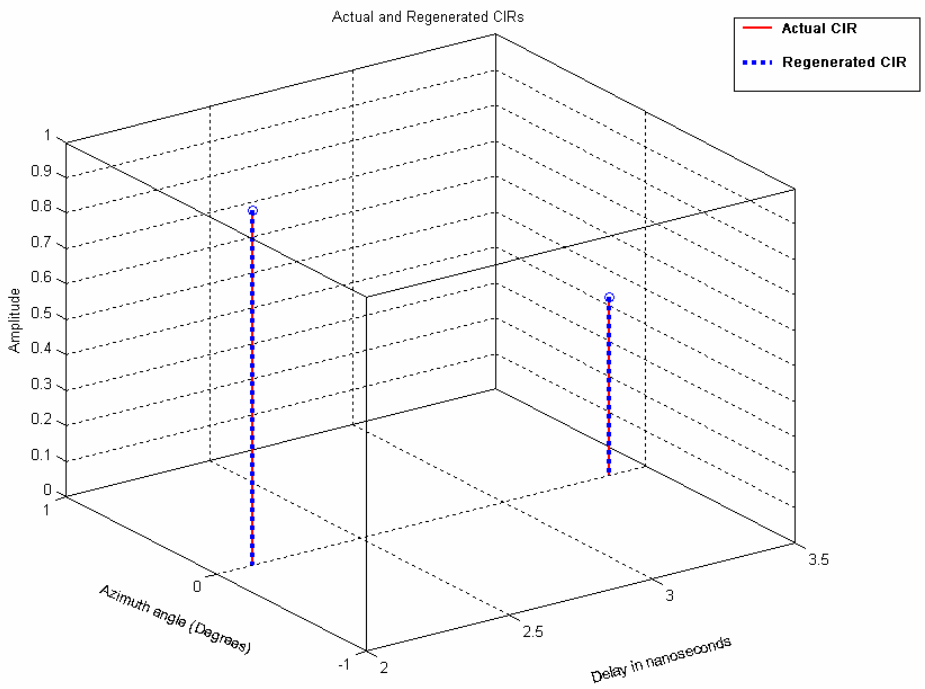

Figure 2-13 Original and Resulting CIRs when path separation is greater than half a pulse width,

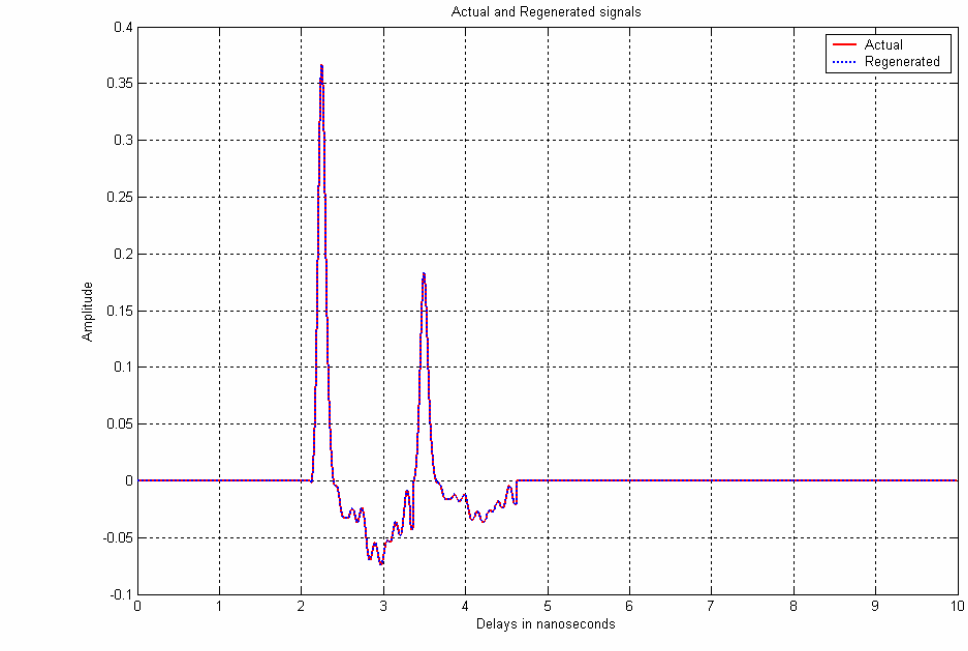

Figure 2-14 Actual and regenerated signals for path separations greater than half a pulse width

Case 2: Temporal Separation < Half the Pulse Width

When the multipath components at (4,4) are separated temporally by less than half the pulse width, the accuracy of the Sensor CLEAN algorithm is a function of the angular separation between the multipath components. It was found that as long as the separation between the paths in the azimuth plane was greater than 5 degrees the TOA and AOA were estimated correctly as shown in Figure 2-11 and 2-12.

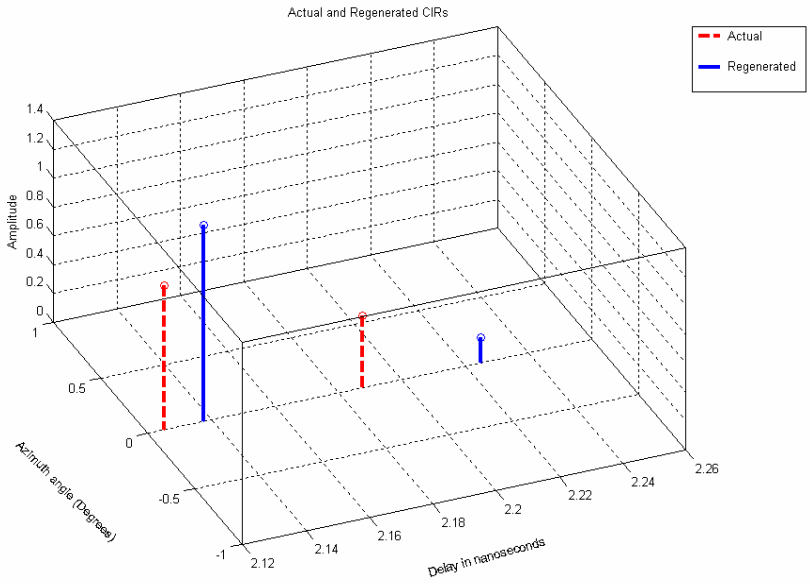

Figure 2-15 Angular Path separation of 0 degrees

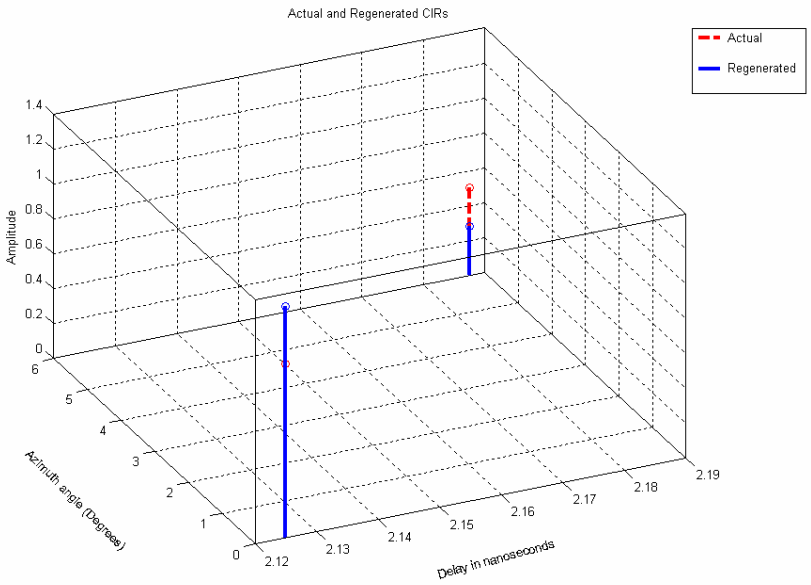

Figure 2-16 Angular Path separation of 6 degrees

(ii) Sensor-CLEAN algorithm applied to multiple paths

In this scenario a CIR is generated randomly using the Saleh-Valenzuela model [Sale87]. This CIR is designated as the CIR at location (4,4) of the 49 element grid of Figure 2-2. Each path in this CIR is assigned a random AOA in the azimuth plane based on the spatial channel model to be discussed in Chapter 3. For now it is sufficient to state that the initial 20ns of the profile has an AOA distribution whose angle spread is lower than the rest of the signal. Based on the grid geometry, CIRs for the other locations are calculated in a fashion similar to the earlier section. The CIRs are then convolved with the reference pulse to produce a set of 49 signals. The 2-D Sensor CLEAN algorithm is then run on this set of signals.

Figure 2-17 shows the Amplitudes versus the TOA plotted for both the original and the estimated CIRs (generated CIRs and the values obtained from the 2-D Sensor CLEAN) for one run of. It can be seen that most of the TOA's are identified correctly. In some cases at very low temporal separations, there is mismatch either in the TOA or the strength of the multipath component.

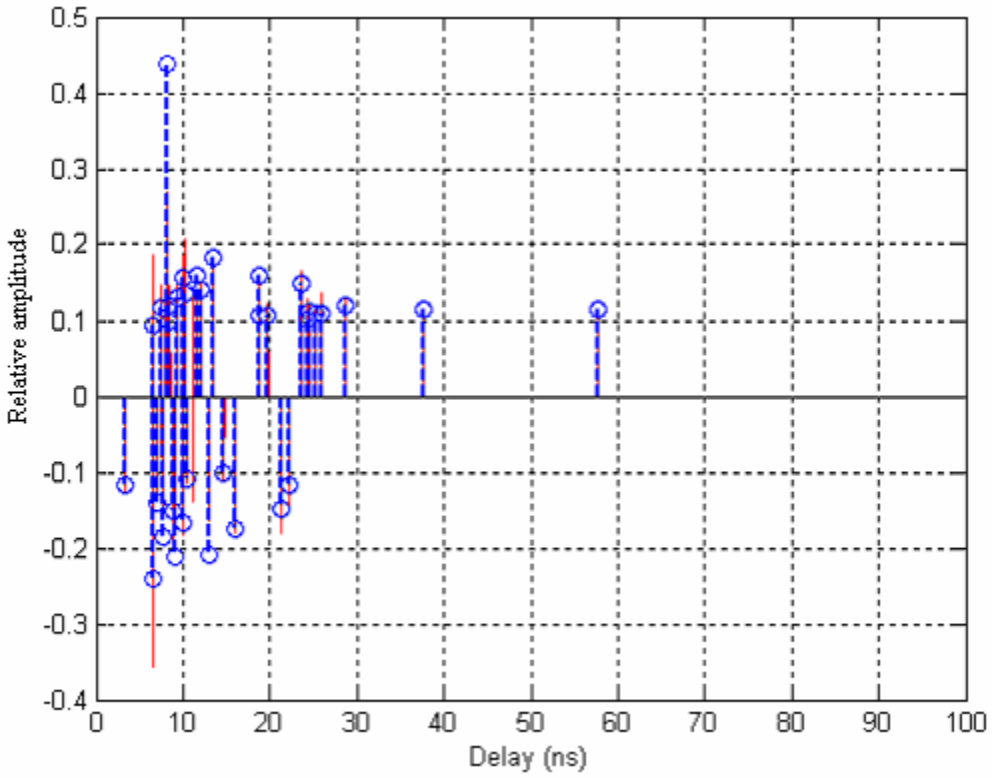

Figure 2-17. Plot of the Amplitudes versus the delays for the original and regenerated CIRs

Figure 2-18 provides a 3-D plot showing TOA, AOA and the amplitudes of the true and the estimated CIRs. Again the AOAs register correctly for all cases except where the path separation is less than half a pulse width. Figure 2-19 shows the amplitudes versus the AOA for greater clarity. The mean delay spread and the mean angle spread of the original and regenerated signals are presented in Table 2-2 for multiple runs of the Sensor-CLEAN algorithm. It can be seen that the original and the regenerated signal are well matched in terms of delay and angle spreads.

Table 2-2 Delay and angle spread for the original and regenerated signals

	RMS Delay spread (ns)	**Angle spread**
Original signal	12.9	118°
Regenerated signal	11.9	114°

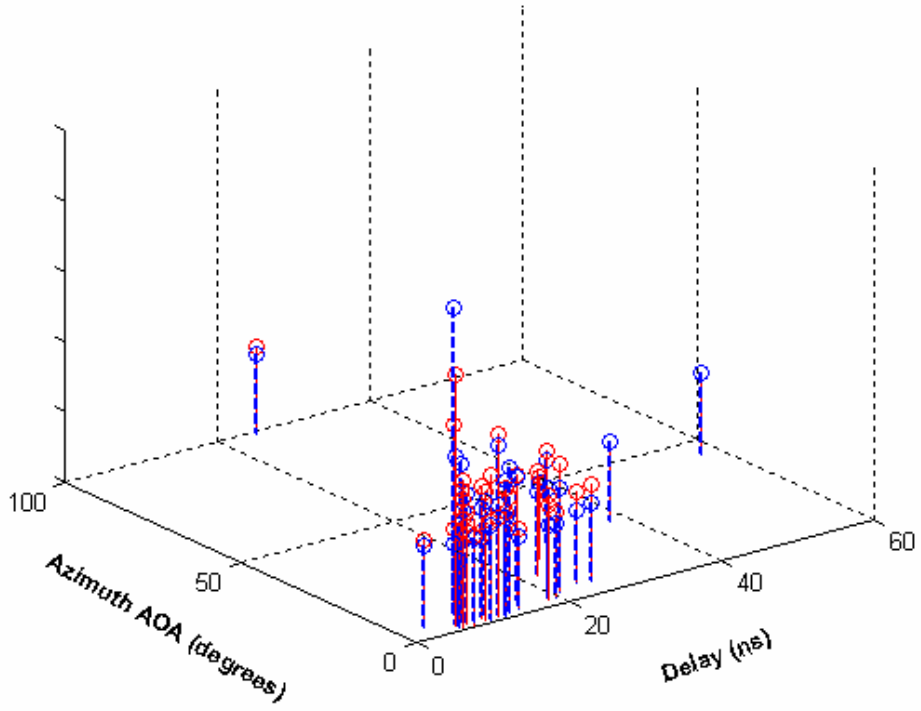

Figure 2-18 3-D plot of the original and the regenerated CIRs

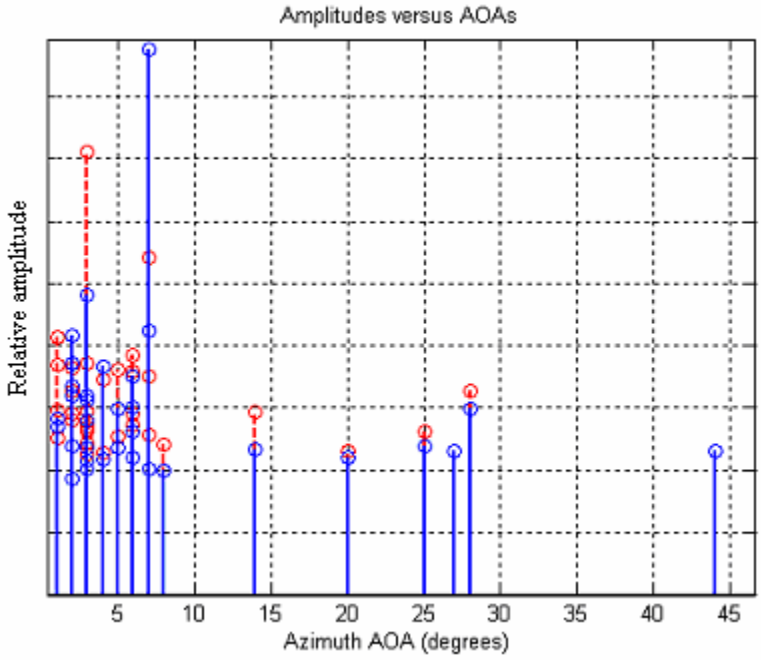

Figure 2-19. Plot of the Amplitudes against the AOAs for the original and the regenerated CIRs

2.4 Conclusions

This chapter described the UWB NLOS indoor channel measurements that were conducted to aid channel characterization. The measurements were also tailored with a view to also explore the spatial characteristics of the channel. A two dimensional deconvolution algorithm that was used to obtain the AOA of the multipath was described. An insight into the performance of the algorithm was obtained by applying it to artificial channel data.

Chapter 3. Spatial Channel Characterization and Modeling

The use of antenna arrays is very common for narrowband and wideband communication systems. Apart from classical performance improvement using receive and/or transmit diversity, multi-sensor arrays are increasingly deployed for position location and tracking as well as for interference cancellation applications. In order to study the performance of such systems when UWB signals are used, the spatial properties of the UWB channel need to be characterized and used to create spatial channel models for designing multiple antenna systems.

This chapter explores some of the spatial aspects of the UWB channel. In order to aid channel characterization and modeling efforts a number of NLOS and LOS measurements were taken over a 1m x 1m grid using UWB pulses as described in Chapter 2. Distributions of the received signal energy are presented, illustrating the immunity to spatial fading. Amplitude statistics of the received signal are fit to different distributions. Angle-of-Arrival distributions obtained using the Sensor-CLEAN algorithm presented in Chapter 2 are used to develop a two-dimensional channel model incorporating the spatial and temporal characteristics of the UWB channel.

3.1 Statistics of the received signal energy

The received total energy ${E_{total}}^{l}{}_{i,j}$ at the $(i,j)^{th}$ position of location l is calculated as

$$ {E_{total}}^{l}{}_{i,j} = \frac{\int_0^T \left| {r^l}_{i,j}(t) \right|^2 dt}{R} \tag{3.1} $$

where ${r^l}_{i,j}(t)$ is the received signal profile after filtering[2] at grid location (i,j) of measurement location l, and T is the observation interval. Note that R is referenced to

[2] The received profiles were filtered in the time domain. The 3 dB cutoff frequencies were 0.1 GHz and 12 GHz. See Chapter 2 for more details

1Ω in all the energy calculations. The relative path attenuation at a location l and position (i, j) is defined as [Win02]

$$F_{total}{}^{l}{}_{i,j}[dB] = 10\log_{10}\left(E_{total}{}^{l}{}_{i,j}\right) - 10\log_{10}(E_{ref}) \tag{3.2}$$

where E_{ref} is defined as the energy in the LOS path measured by the receiver located 1m from the transmitter, which remains constant for a particular pulse. The measurement of E_{ref} is described in Chapter 2.

First and second order local statistics of the total received energy were calculated for the measurement set at each location l as follows:

$$\hat{\mu}^{l}_{total} = \frac{1}{N}\sum_{i,j} F_{total}{}^{l}{}_{i,j} \tag{3.3}$$

$$\hat{\sigma}^{l}_{total} = \sqrt{\frac{1}{N-1}\sum_{i,j}\left(F_{total}{}^{l}{}_{i,j} - \hat{\mu}\right)^2} \tag{3.4}$$

where $\hat{\mu}^{l}_{total}$ and $\hat{\sigma}^{l}_{total}$ are the estimated means and standard deviations respectively at each location l and N is the number of multipath profiles in each location. These statistics are presented in Table 3-1 and Table 3-2 for the Gaussian and the Trapezoidal pulses[3] respectively.

Table 3-1 Statistics for the Gaussian Pulse (all in dB)

Location	Distance(m)	μ_{total}	σ_{total}	μ_{bin}	σ_{bin}	μ_{rake}	σ_{rake}
G1	4	-27.6237	0.3889	-42.4986	1.0708	-44.994	2.0427
G2	3.7	-29.3241	0.498	-43.5344	1.154	-45.7516	3.4479
G3	4.3	-28.2588	0.6002	-42.725	0.9358	-44.0068	1.4671
G4	4.7	-28.6882	0.6642	-40.8869	0.978	-42.5725	3.0364
G5	3.4	-26.8216	0.5702	-39.7201	1.1808	-40.6931	3.1006
G6	5.1	-24.2704	0.7113	-38.0054	1.4689	-39.504	2.2002
G7	6	-22.6872	0.588	-33.8582	0.9752	-34.8731	3.3445

[3] The Trapezoidal pulse had a width of approximately 2 ns and the Gaussian pulse a width of 200 ps. Chapter 2 provides more details regarding the measurements with these pulses.

Table 3-2 Statistics for the Trapezoidal Pulse (all in dB)

Location	Distance(m)	μ_{total}	σ_{total}	μ_{bin}	σ_{bin}	μ_{rake}	σ_{rake}
T1	8.9	-21.2309	0.7403	-31.3101	1.4477	-34.3981	2.3001
T10	3.8	-11.1958	0.5811	-19.814	1.3882	-23.0737	3.7363
T11	6.6	-21.8803	0.48	-32.5522	1.2126	-36.5914	4.0848
T12	5	-19.002	0.7186	-26.8937	1.2381	-27.5717	1.8071
T13	5.1	-16.1531	0.9472	-25.9624	1.6506	-28.4846	1.5673
T14	4.3	-14.0025	0.6834	-23.5426	1.1943	-25.151	1.7487
T15	6.9	-18.7137	0.7641	-28.9758	1.2714	-31.3439	2.9273
T2	6	-13.641	0.6234	-22.981	1.3484	-25.0081	1.7829
T3	7.9	-20.5783	0.7819	-30.8346	1.3143	-32.0177	2.5972
T5	8	-18.5943	0.8777	-28.2209	1.4337	-31.6484	3.9177
T6	2.5	-7.2942	1.0864	-15.299	2.2196	-15.5853	2.5934
T7	6.6	-16.2336	0.9029	-25.4324	1.6344	-26.4368	2.6539
T8	5.2	-13.7679	0.7365	-23.0145	1.7401	-26.6801	3.9225

Figure 3-1 plots the empirical CDF (i.e., cumulative histogram) of the received signal energy for the Gaussian pulse, at each location l where the x-axis is in dB. The empirical CDF for the trapezoidal pulse is shown in Figure 3-2. The immunity of UWB to multipath induced fading can be clearly discerned from both plots. In most cases the variation between the maximum and the minimum value as the receiver moves in the spatial grid is less than 3 dB. This is slightly less than [Win02] who reported a value of 4 dB in similar circumstances. Also compared to the 6 – 7 dB obtained for narrowband signals [Hibb04] the UWB signals are less prone to local area fading.

Lower spatial fading for UWB signals directly translates to smaller fading margin in designing communication systems and demonstrates its robustness in indoor applications. The Gaussian pulses on average exhibit slightly lower standard deviations than the Trapezoidal pulses. The smaller width of the Gaussian pulse implies larger bandwidth and consequently more robustness to fading.

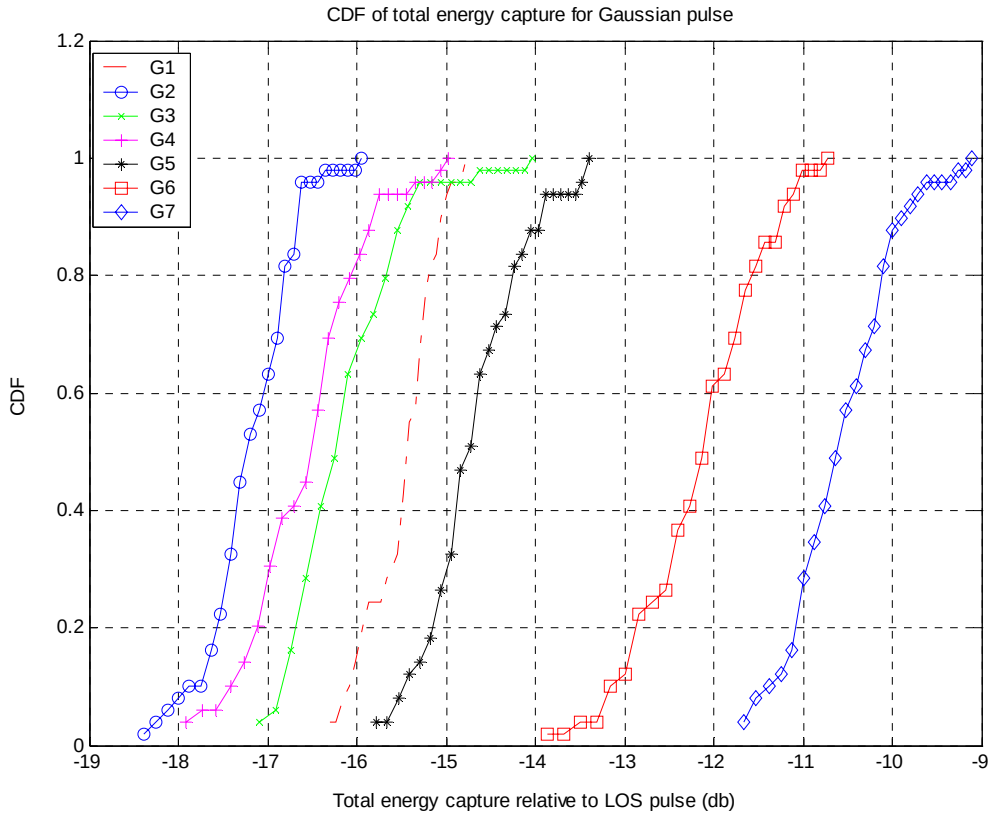

Figure 3-1 Empirical Cumulative Distribution Functions (CDF's) plotted for the total energy capture for the Gaussian Pulse at each Measurement location

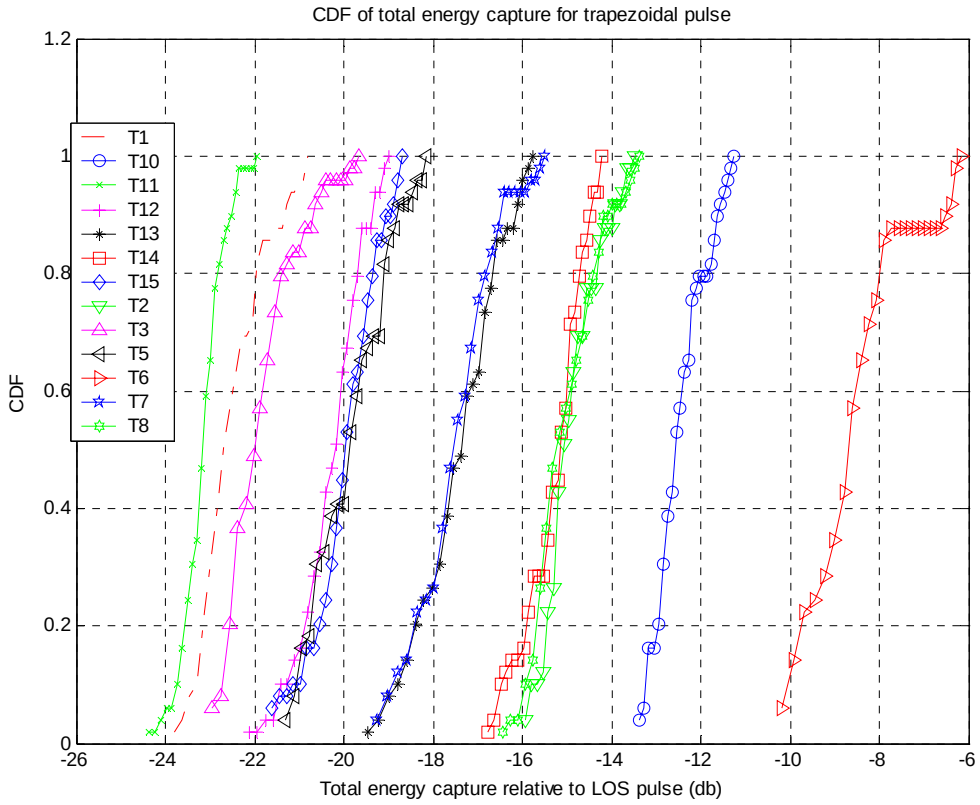

Figure 3-2 Empirical Cumulative Distribution Functions (CDF's) plotted for the total energy capture for Trapezoidal Pulse at each Measurement location

3.2 Rake receiver and Spatial Fading

3.2.(1) Fading at a specified delay

The variation of the received power at specific delays is of interest in designing Rake receivers for UWB communications. Specifically examining the statistics at a particular delay provides insight into the performance of a single finger Rake receiver collecting energy at a specific delay as it moves through the environment. For this analysis, the received signal profile is divided into different time bins, where each bin is of the order of one pulse width. It is assumed that each bin contains one resolvable multipath. The profiles at each location are aligned such that the first bin of each profile contains the direct path (if it exists).

The energy per bin is calculated as[4]

$$E^{k}{}_{bin}{}^{l}{}_{i,j} = \int_{(k-1)T_w}^{kT_w} \left| r_{total}{}^{l}{}_{i,j}(t) \right|^2 dt \tag{3.5}$$

where k is the bin-number and T_w is the length of each bin which is equal to the width of the received free space component.

The first and second order statistics are calculated similar to equations (3.3) and (3.4)

$$\hat{\mu}^{l}_{Rake} = \frac{1}{N} \sum_{i,j} F_{Rake}{}^{l}{}_{i,j} \tag{3.6}$$

$$\hat{\sigma}^{l}_{Rake} = \sqrt{\frac{1}{N-1} \sum_{i,j} \left(F_{Rake}{}^{l}{}_{i,j} - \hat{\mu}_{Rake} \right)^2} \tag{3.7}$$

where $F_{Rake}{}^{l}{}_{i,j}[dB] = 10\log_{10}\left(E^{k\max}{}_{bin}{}^{l}{}_{i,j}\right) - 10\log_{10}(E_{ref})$ and $k\max$ is the bin containing the highest average energy from a set of 49 measurement profiles at a given location l

The values of $\hat{\mu}^{l}_{Rake}$ and $\hat{\sigma}^{l}_{Rake}$ are shown in Table 3-1 and Table 3-2. The corresponding CDF's are shown in Figure 3-3 and Figure 3-4. It is clearly observed that the variance in signal energies for a 1-Finger Rake can be significantly higher as compared to the variance in the total energy. Additionally, the weaker signals (i.e., those with less average energy) show more variation than stronger signals.

[4] Note that all energy calculations are referenced to a 1 Ohm resistance.

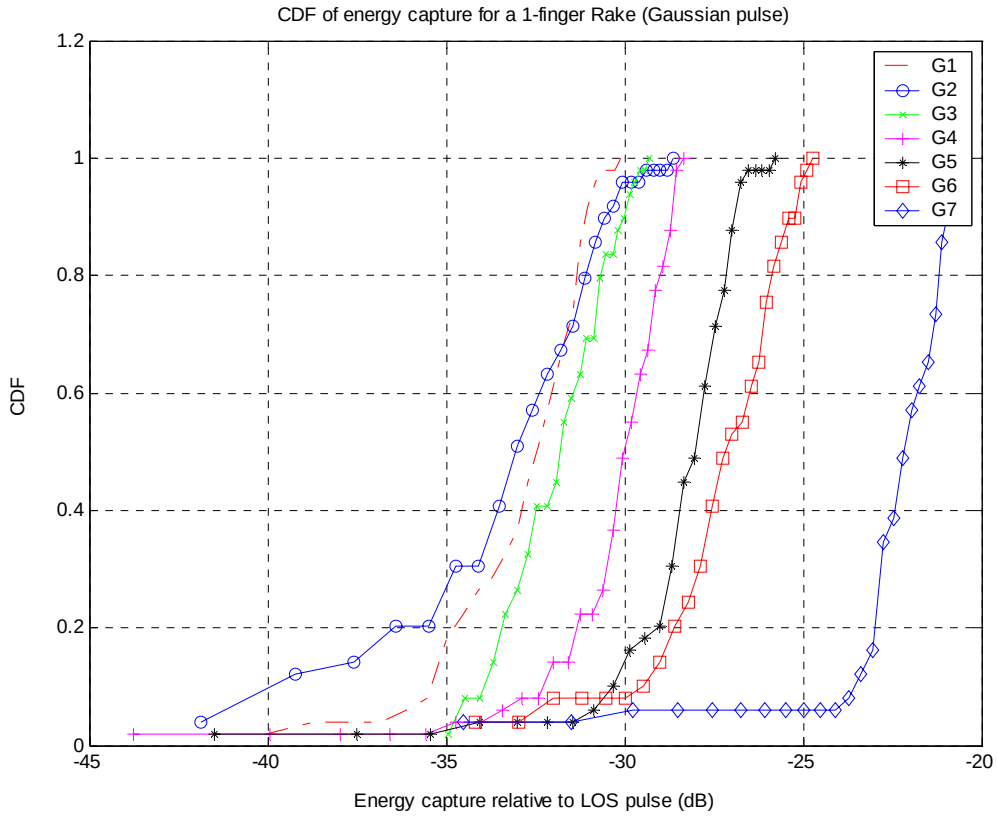

Figure 3-3. Empirical CDF's of the energy capture at a Constant Delay (bin with the highest mean energy) for Gaussian Pulse

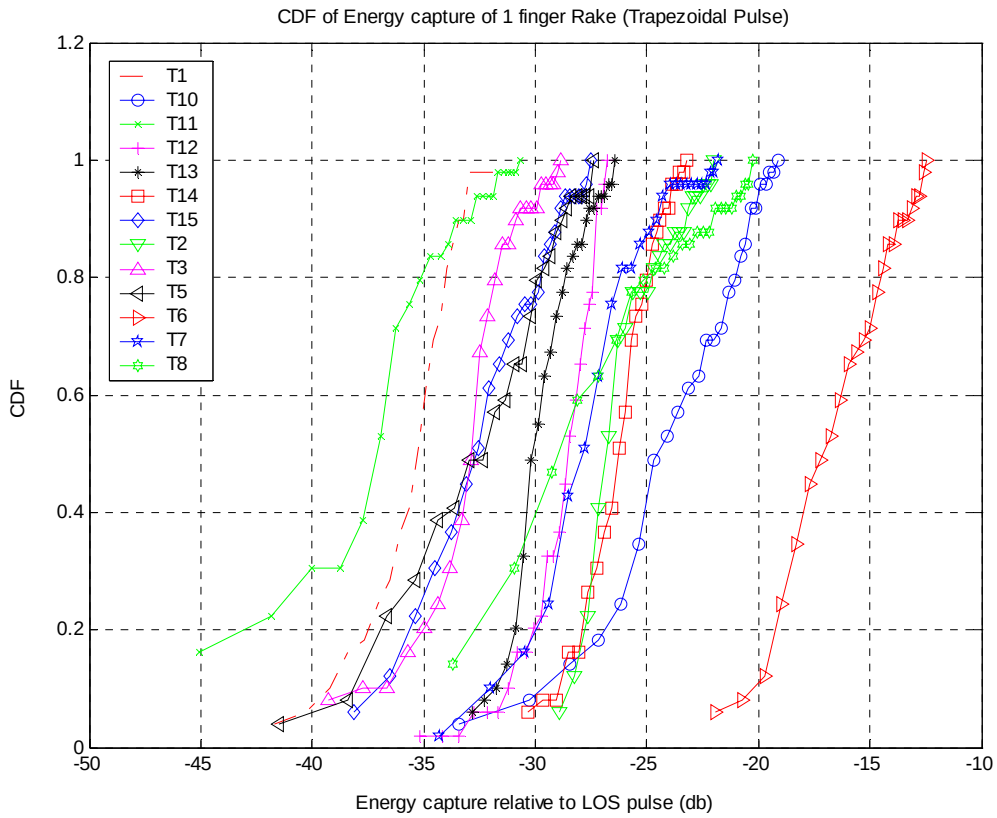

Figure 3-4. Empirical CDF's of the energy capture at a Constant Delay (bin with the highest mean energy) for Trapezoidal Pulse

3.2.(2) Rake receiver with multiple fingers

In typical scenarios a Rake receiver utilizes more than one finger. The variation in local fading when multiple-finger Rake receivers are used with different pulse widths is described in this section. The following procedure was adopted to examine spatial fading with multiple Rake fingers.

The signal energy in each bin is calculated for each received profile in the spatial grid. Thus for the trapezoidal pulse there are 50 bins of 2 ns width and for the Gaussian pulse there are 450 bins of ~200 ps width.

The bins are sorted in descending order of their mean energy content at a particular location. (For example at a location T3, the mean energy for each bin across the 49 positions is calculated and used to sort the bins.)

The energy collected by an N-finger Rake receiver is obtained by summing the energy of the N bins with the highest mean energy content. These energies are normalized by the mean energy of the N–finger Rake at that location. This process is repeated for all the locations for the Gaussian and the Trapezoidal Pulses. Thus, there are a total of 13 x 49 channel realizations for the Trapezoidal pulse and 6 x 49 realizations for the Gaussian pulse.

Empirical CDF's were prepared using this data and are plotted on the same graph in Figure 3-5 and Figure 3-6. The CDFs are compared to the situation where the entire signal energy is captured, as discussed in the previous section. It can be observed from the figures that even though the Gaussian Pulse exhibits a lower standard deviation for the case with total received energy it exhibits a higher standard deviation when a limited number of fingers are used. Note that because the energies were all normalized the impact of energy capture (mean energy v/s number of fingers) is ignored. This is studied in [Donl04c].

Table 3-3 presents the standard deviations for the Rake receiver with different numbers of fingers for both the pulses. While the 1-Finger Rake exhibits the highest variance in the received signal energy, we can see that even for a modest number of Rake fingers (5) there is a substantial reduction in the variation of the signal power (approximately 1.5dB versus 2.9dB).

Table 3-3 Standard Deviation for energies collected by Rake receiver over a $1m^2$ grid with different fingers

	Standard Deviation (dB)	
Fingers	**Trapezoidal pulse (~ 2 ps)**	**Gaussian Pulse (~200 ps)**
1	2.89	3.67
2	2.19	2.81
5	1.55	2.18
10	1.17	1.67
15	1	1.43
Total energy capture	0.77	0.58

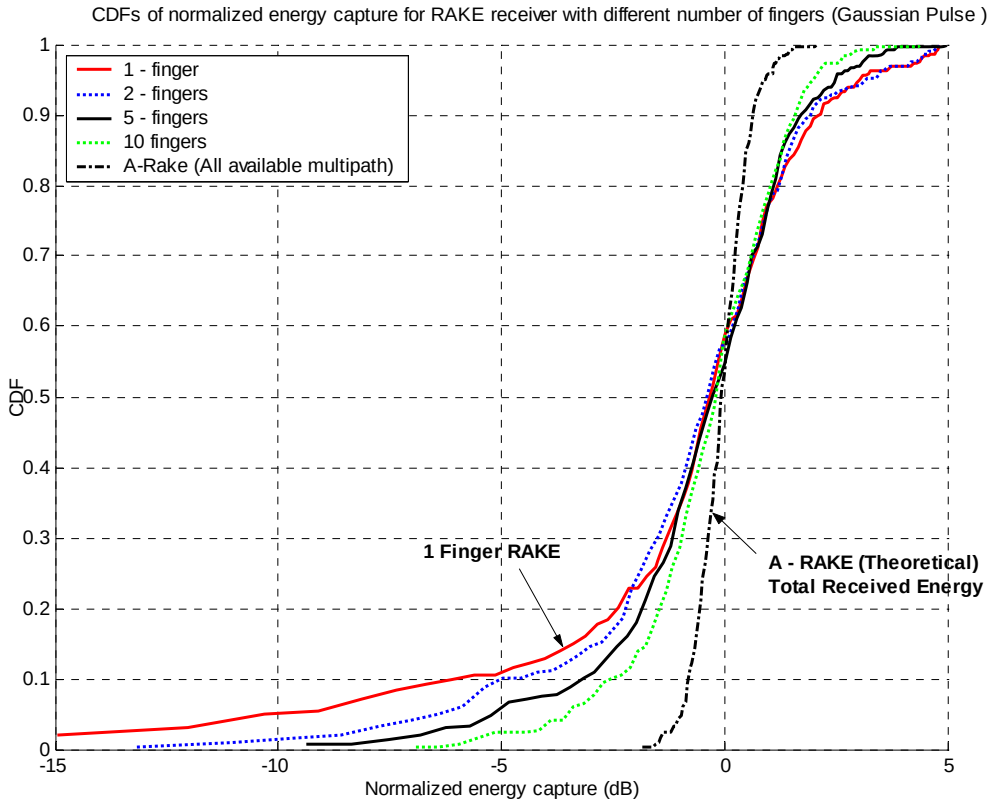

Figure 3-5 Empirical CDF's for energy capture of Rake receiver's with multiple fingers for the Gaussian Pulse (over all locations)

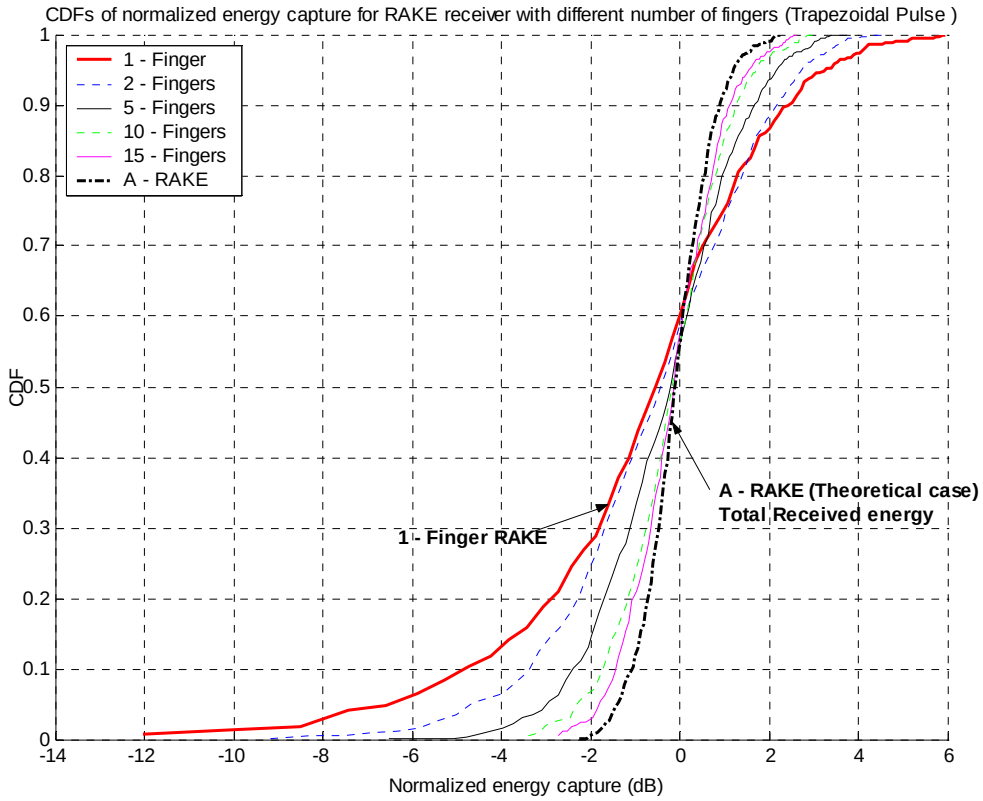

Figure 3-6 Empirical CDF's for energy capture of Rake receiver's with multiple fingers for the Trapezoidal Pulse (over all locations)

3.3 Highest energy in a bin (Delays not constant)

The fading margin of a system is the allowance for fading incorporated into the system link budget and is usually defined as the additional margin required to assure coverage over 90% of the area. This can be easily calculated from the CDF of the signal energy over a local area. In order to examine the effect of UWB waveforms on fading margin for a single finger Rake receiver (i.e. a simple correlator), the received signals at each grid point are first aligned so that the direct component (if it exists) would line up at the same excess delay. The profile is then divided into bins of approximately the width of one pulse duration. The statistics of the bin with the highest energy for every grid position at

a particular location were then calculated. In this calculation, the bin with the largest energy in each profile is selected. The bins may be of different delays at each position. Note that this is calculated differently than in the previous two sections. Whereas previously Rake fingers at fixed delays across the entire grid were examined, in this calculation the Rake receiver is allowed to pick the best delay at each grid location. This situation corresponds to the spatial statistics observed by a collection of Rake receivers (each at one grid location) where each Rake is allowed to find the strongest possible signal. The corresponding CDF's are shown in Figure 3-7 and Figure 3-8 for the Gaussian and Trapezoidal pulses respectively. The standard deviation (σ_{bin}) and mean (μ_{bin}) are listed in Table 3-1 and Table 3-2 for both sets of pulses. It is seen that σ_{bin} is substantially lower than that the standard deviation seen at a specific delay (σ_{Rake}) due to the selection diversity. It is interesting to note that μ_{bin} is roughly 15dB below μ_{total}. This is due to the fact that the first path represents a small fraction of the total energy. In most cases, the 90% level for both the Gaussian and the Trapezoidal pulses was less than 2 dB. This is significantly less than the fading margin employed in narrowband systems and further demonstrates the robustness of UWB to fading.

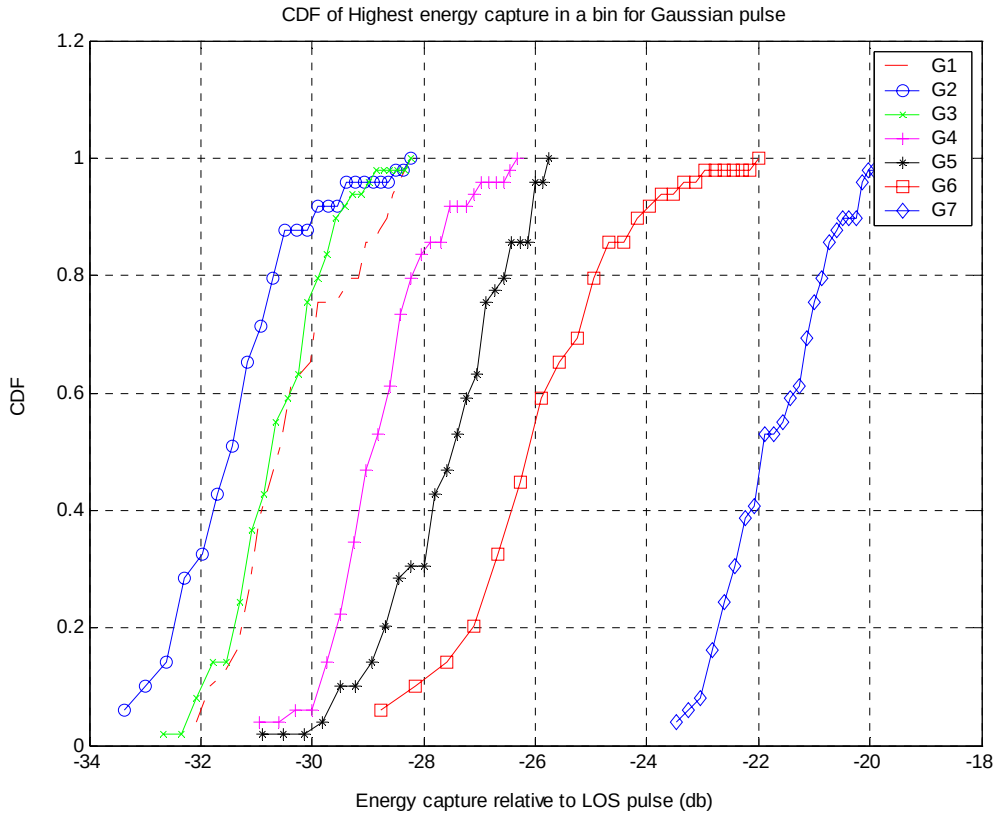

Figure 3-7. CDFs for the highest energy capture in a bin for Gaussian Pulse. The Rake receiver picks the best bin(position) at each location.

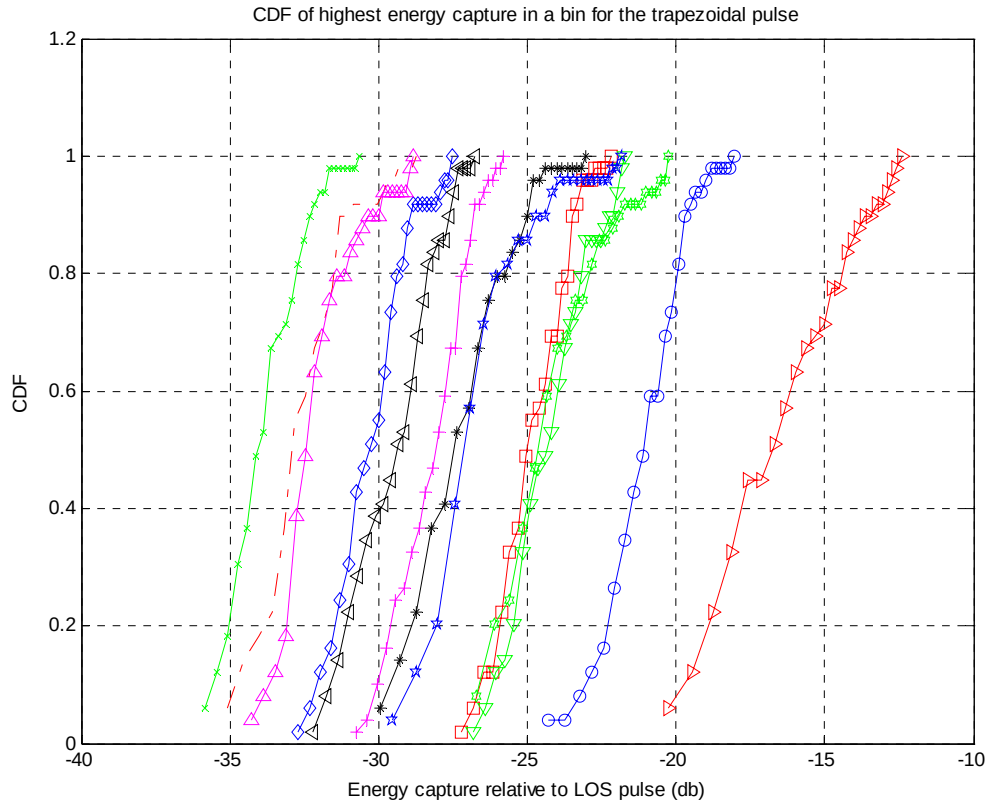

Figure 3-8. CDFs for the highest energy capture in a bin for Trapezoidal Pulse. The Rake receiver picks the best bin(position) at each location.

3.4 Multipath Amplitude distributions

The amplitude distribution of multipath components in a received UWB signal are important when creating channel models. This section provides insight into the amplitude distributions based on the channel measurements conducted at MPRG. Two perspectives are considered. Firstly, global amplitude distributions at different excess delays are examined. Secondly, local amplitude distributions at different excess delays are studied.

The Kolmogorov – Smirnov test [Mass51] is used to test the goodness of fit of the empirical data to standard distributions. It compares the distributions of values in the two sets of data samples X_1 and X_2 of length n_1 and n_2, respectively. The null hypothesis for this test is that X_1 and X_2 have the same continuous distribution. The

alternative hypothesis is that they have different continuous distributions. The hypothesis is rejected if the test is significant at the 5% level. For each potential value x, the Kolmogorov-Smirnov test compares the proportion of X_1 values less than x with proportion of X_2 values less than x.

Three probability distributions discussed in literature have been considered in this thesis, the log-normal distribution, the Weibull distribution, and the Rayleigh distribution. The Log-Normal CDF can be written as

$$F\left(x \mid \mu, \sigma\right) = \frac{1}{\sigma\sqrt{2\pi}} \int_0^x \frac{e^{\frac{-\left(\ln(t)-\mu\right)^2}{2\sigma^2}}}{t} dt \tag{3.8}$$

This is equivalent to the normal distribution when the amplitudes and the statistics are expressed in log scale $20\log_{10}(A)$. The received signal amplitudes are expressed in dB and the mean and the standard deviation were calculated using dB values. The Weibull CDF is given as

$$F\left(x \mid a, b\right) = 1 - e^{-\left(\frac{x}{a}\right)^b} \tag{3.9}$$

The Weibull parameters a and b are known as the normalization factor and the shape factor respectively. The Weibull distribution simplifies to the Rayleigh distribution when $b = 1$. The Rayleigh CDF is given as

$$F\left(x \mid b\right) = 1 - e^{-\left(\frac{1}{2}\sqrt{\frac{x}{a}}\right)} \tag{3.10}$$

The Rayleigh distribution is popular in representing pure scattering models in the absence of a strong LOS component. The parameter b is obtained using a maximum likelihood estimate from the sample data.

3.4.(1) Global Amplitude Statistics after binning the received signal at different excess delays

The received data was binned so that the amplitude of each bin would signify the amplitude of the composite multipath component in that bin. Data from bins at specific excess delays from the entire measurement set (all NLOS measurements) were matched to theoretical distributions. Figure 3-9 and Figure 3-10 show the results for the Gaussian

and Trapezoidal pulses respectively. It can be observed that the Lognormal Distribution gives the best match to the obtained data. The Kolmogorov – Smirnov test was carried out to test which distribution best fit the data. After considering all excess delays, it was found that the Lognormal passed the test with 95% confidence for 87% of the cases. The Weibull and the Rayleigh were able to achieve only 35% and 12% pass rates respectively at the 95% confidence level. The distributions have lower means and larger variance as the excess delay increases.

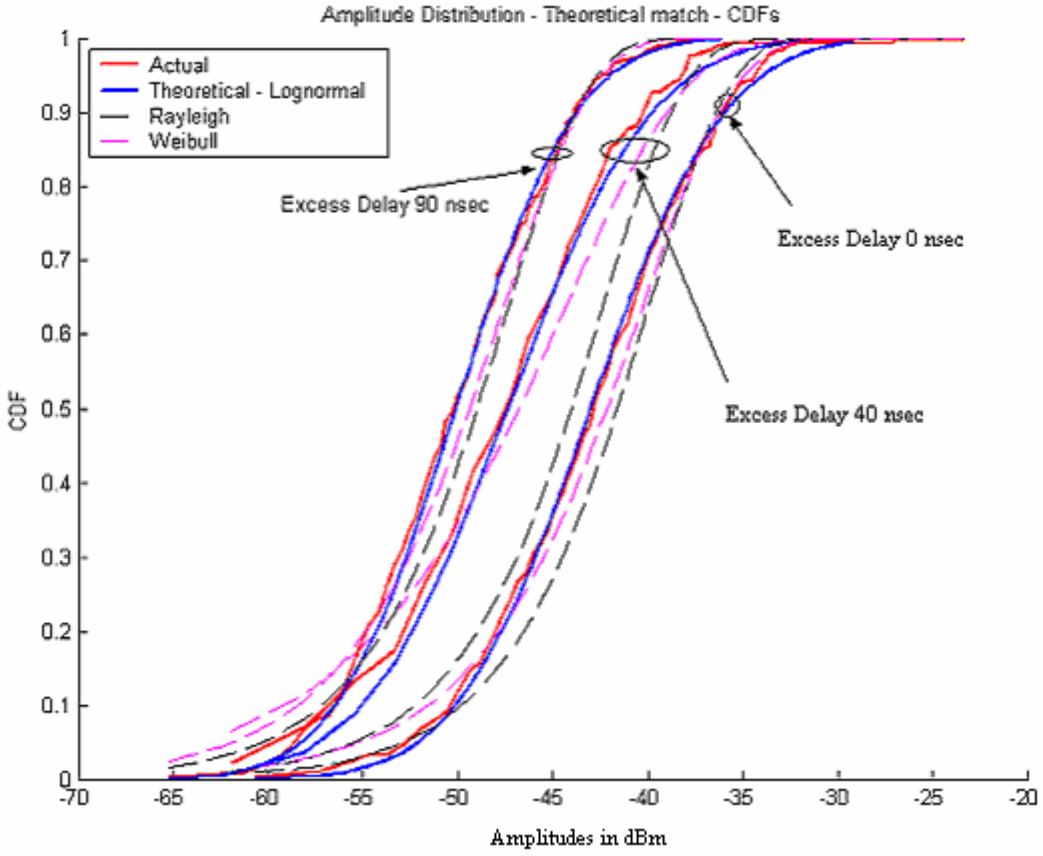

Figure 3-9 Amplitude Statistics matched to 3 different distributions at different excess delays for the Gaussian pulse over all locations. It is seen that the Lognormal is the best fit for most cases.

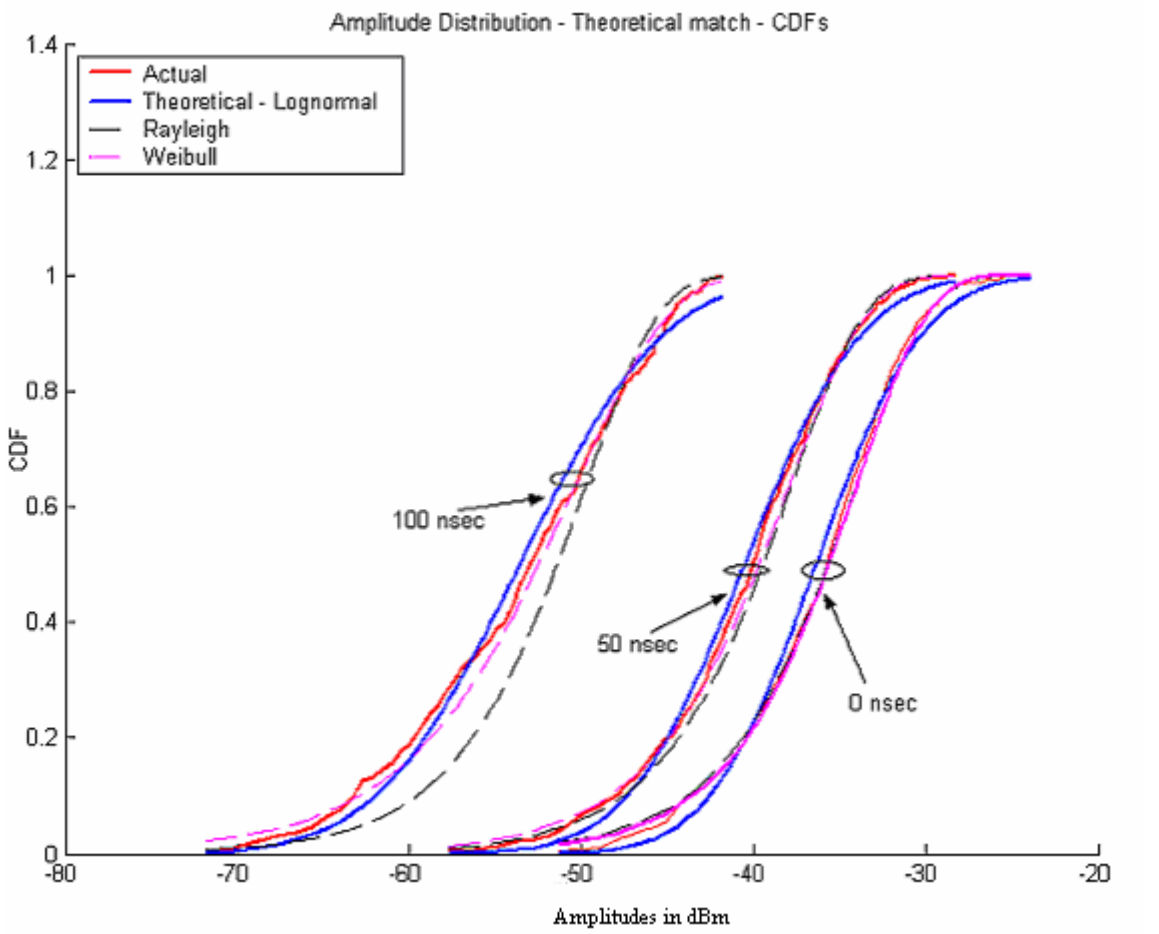

Figure 3-10 Amplitude Statistics matched to 3 different distributions at different excess delays for the Trapezoidal pulse over all locations. It is seen that the Lognormal is the best fit for most cases.

3.4.(2) Amplitude Distribution at different excess delays

Figure 3-11 shows the amplitude distribution at different excess delays for the Gaussian pulse when only the one location (consisting of 49 points) is considered. To increase the number of points, 5 adjacent histogram bins were combined, making the total bin size 1 ns. In channel modeling the paths are modeled as having a lognormal distribution about an exponentially distributed mean.

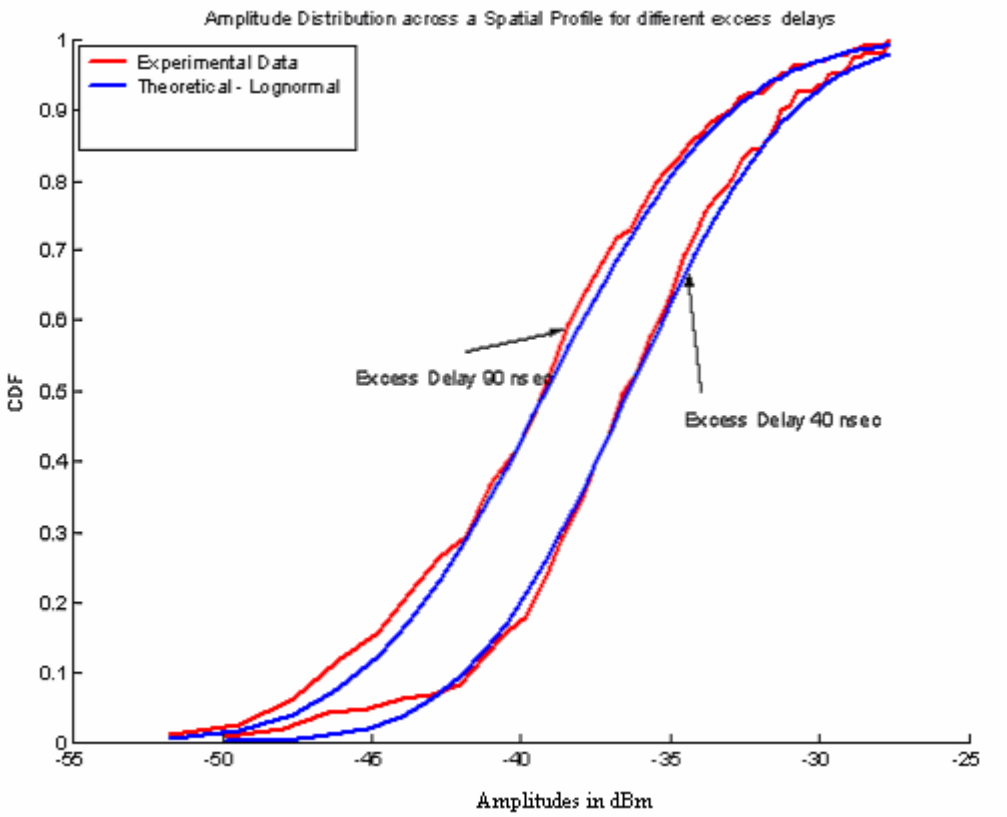

Figure 3-11. Amplitude distribution for one sample location (Location 3) using Gaussian Pulse. Other locations exhibited a similar match

3.4.(3) Temporal Correlation (Correlation within a profile)

In an office environment there are a uniform number of scattering objects, thus different multipath components arriving from these scatterers should exhibit a low degree of correlation. In Figure 3-12 the observed autocorrelation function of the received signal versus the excess delay is plotted for both pulses. It is seen that the components are uncorrelated after an excess delay roughly equivalent to the pulse duration. There is no correlation introduced by the channel. As expected, the trapezoidal pulse shows more temporal correlation than the Gaussian pulse since it has a duration of roughly 2ns as opposed to 200ps. Note that the sampling interval was equal to the width of the pulses (approximately 200 ps for the Gaussian pulse and 2 ns for the Trapezoidal pulse).

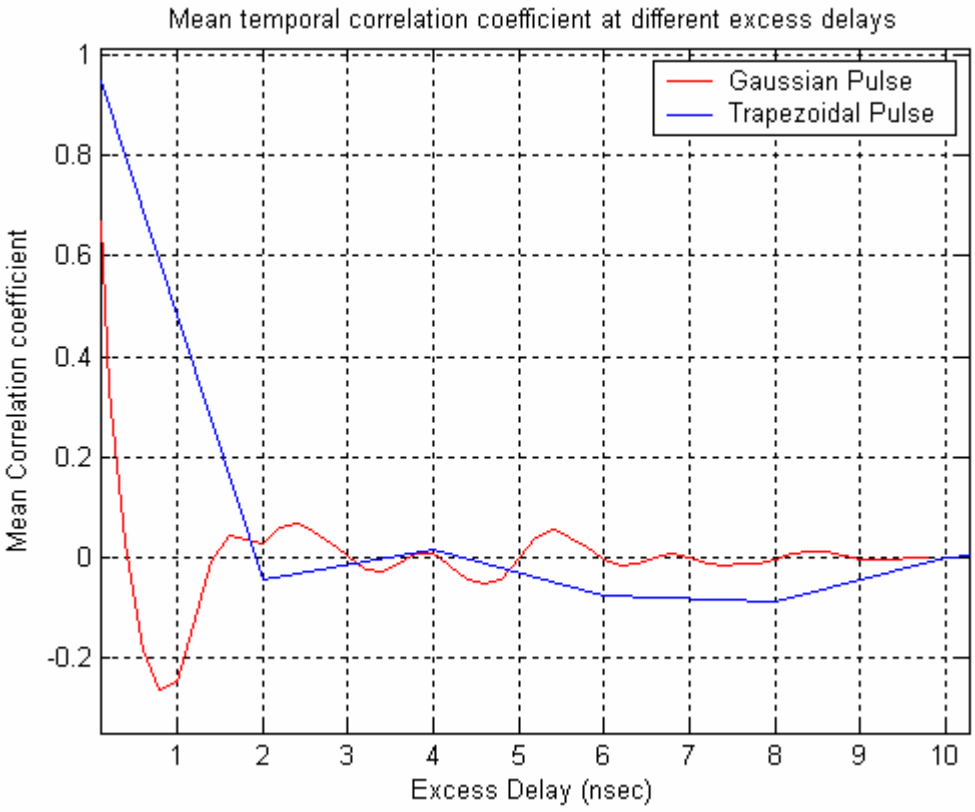

Figure 3-12 The mean correlation coefficient between multipath components at any 2 excess delays. Components are uncorrelated after the first few nanoseconds

3.5 Spatial Correlation of UWB signals

It is useful to characterize the correlation of UWB signals to determine the effectiveness of diversity combining schemes or beam-forming techniques. Conventional diversity combining schemes work best when the received signals exhibit a low degree of correlation whereas beam-forming schemes rely on a high degree of correlation.

The normalized correlation coefficient between the UWB received signal voltages at antennas x and y during one symbol interval can be obtained as

$$r_{\text{int}_{x,y}} = \frac{\int_0^{T_s} r_x(t) r_y^*(t) dt}{\sqrt{\int_0^{T_s} r_x^2(t) dt \int_0^{T_s} r_y^2(t) dt}} \tag{3.11}$$

where $r_x(t)$ *and* $r_y(t)$ are the received signals at antennas *x* and *y* respectively.

Relatively few spatial correlation measurements have been undertaken for UWB bandwidths. In [Prettie 02] measurements of spatial dependence were conducted at frequencies from 2-8 GHz in a residential environment using a vector network analyzer. The spatial correlation of UWB signals at separation distances ranging from 2 to 6 inches (5 cm to 15 cm) were characterized. The angle spread was reported to be lower than that observed in [Cramer]. However no information regarding the distribution of the AOA was provided. [Li 03] reported some findings related to the spatial correlation between adjacent antenna elements at different antenna separations. A 2 ns pulse was used in the experiment and the measurements were performed in indoor office/research lab environments. They observed that the spatial correlation is a function of both the distance and the excess delay. This trend was also observed in the measurements presented in this chapter and forms the basic idea in developing the spatial-temporal channel model.

Figure 3-13 and Figure 3-14 present the correlation vs. distance for the trapezoidal and the Gaussian pulses. The correlation coefficients were calculated using equation (3.11) between all combinations of the 49 points in one location for the entire length of the received profile and for the first 10, 20, 30, 40, 60 and 80 ns of the received signal. The

correlation coefficient values at the same distance were averaged to obtain one value for each value of antenna separation.

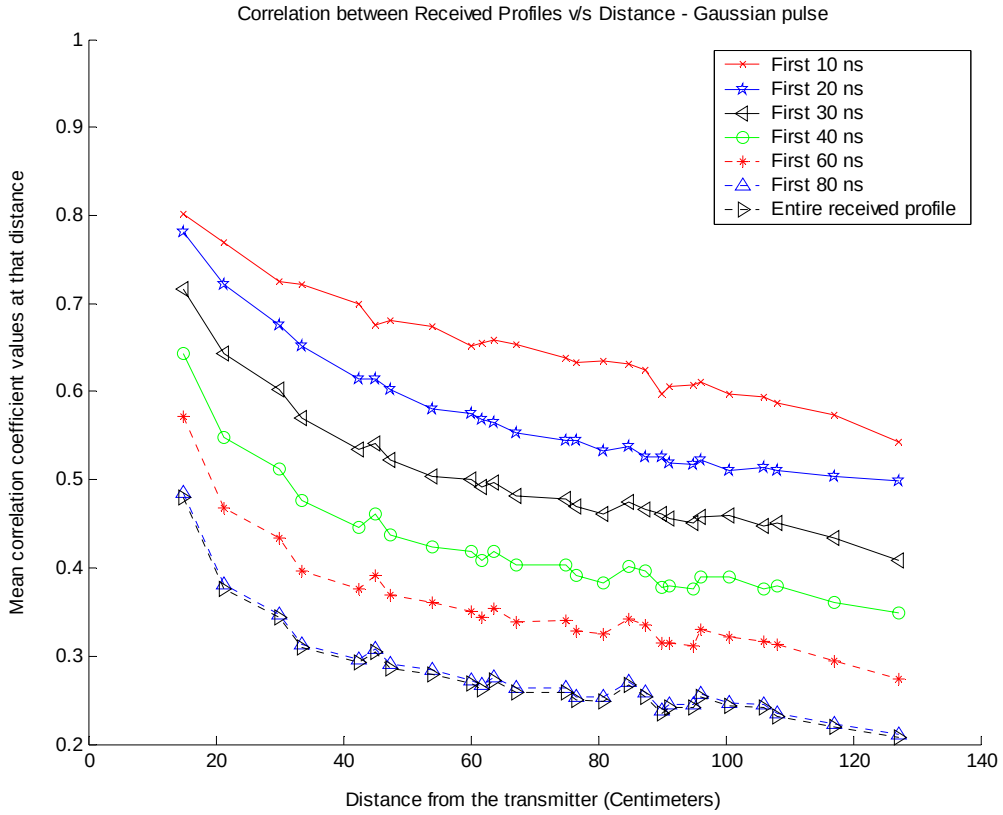

Figure 3-13. Correlation Coefficients vs. Distance from the transmitter for different lengths of the profile (Gaussian Pulse)

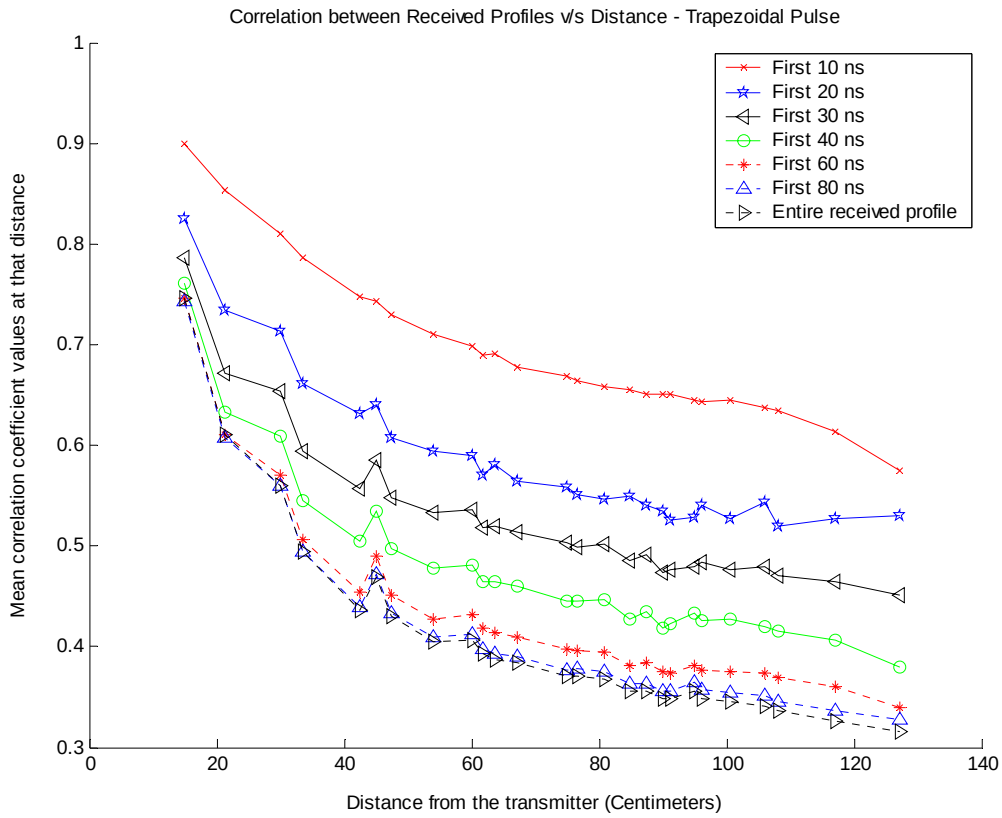

Figure 3-14. Correlation Coefficients vs. Distance from the transmitter for different lengths of the profile (Trapezoidal Pulse)

From the plots it can be discerned that the Gaussian pulse exhibits slightly higher spatial correlation than the trapezoidal pulse. The smaller pulse width (and thus greater bandwidth) would imply more resolvable multipath which can increase the spatial correlation.

Moreover, the initial portion of the received pulse exhibits a moderate to high degree of spatial correlation, particularly as compared to the entire received signal. This means that the direct path and the first few multipath components exhibit high correlation. This however does not extend to the entire profile. The longer the time duration of the received profile used for correlation the smaller the coefficient values. Thus, it can be concluded that UWB signals as a whole exhibit little spatial correlation, but portions of the signal exhibit moderate to high spatial correlation. This has an impact

on the use of diversity arrays. If a Rake receiver is being used which collects only a portion of the signal energy, it is possible that diversity antennas will be ineffective.

The implication from these results is that the early arriving components of the signal correspond to a main scatterer or reflector. There is a high degree spatial correlation exhibited in this first 20ns or so since it is dominated by a single angle of arrival. Later time segments are likely comprised of components arriving uniformly in angle and thus exhibit a low degree of spatial correlation. The angle-of-arrival statistics will be examined shortly.

Correlation coefficients were also calculated for the first 20ns along the 2 axes of the grid that was used to take the measurements in the local area, termed 'Parallel' and 'Perpendicular' (as compared to the LOS direction). Plots of this correlation for the Gaussian and the trapezoidal pulse are provided in Figure 3-15 and Figure 3-16. In this case the first 10ns of the profile was used for correlation. It can be discerned that the variation of correlation for the 'parallel' and the 'perpendicular' case are similar and thus should exhibit a similar drop with increasing antenna separation. This implies that diversity antennas can be placed in either direction for NLOS applications. It is possible that for LOS measurements the correlation between the parallel and perpendicular directions would be different as seen in hallway measurements [Hibb04].

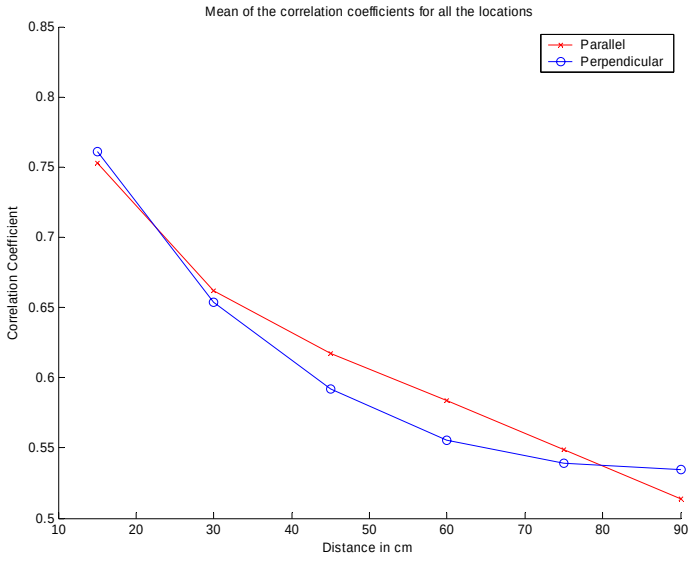

Figure 3-15. Correlation vs. Distance curves in each direction for Gaussian Pulse. The X-axis indicates the distance from the transmitter

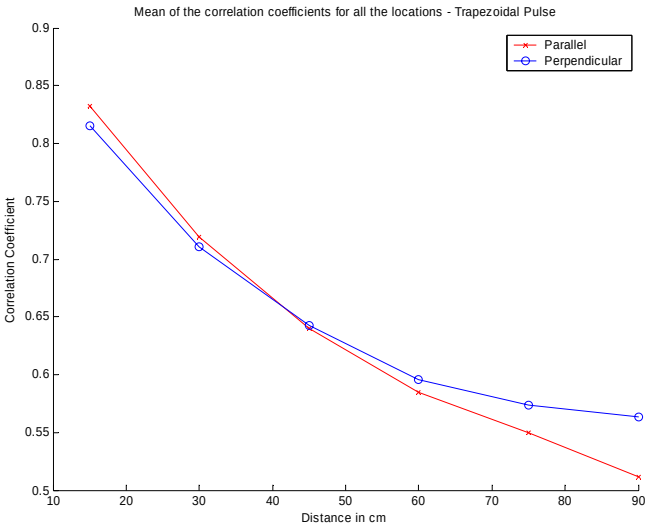

Figure 3-16. Correlation vs. Distance curves in each direction for Trapezoidal Pulse. The X-axis indicates the distance from the transmitter

3.6 Spatial Channel Modeling for UWB signals

Developing accurate channel models is extremely important for studying the performance of UWB systems. Numerous efforts have so far focused on modeling the temporal characteristics of the UWB channel. The use of two or more antenna elements necessitates an approach where the temporal and the spatial properties of the channel are modeled simultaneously. The goal of this section is to arrive at an accurate and flexible spatial channel model that incorporates the spatio-temporal features of the channel.

In general, spatial channel models may be geometric or statistical. Geometrically based spatial channel models specify a region in space where scattering and reflecting objects are located. Additionally information about the distribution in space of these objects is provided which is used to model the TOA and AOA statistics of the channel. Various geometric channel models have been proposed for narrowband and wideband channels. Reference [Erte99] provides an overview and a review of previous literature of spatial channel models for narrowband and wideband antenna array communication systems. The advantage of geometric spatial channel modeling is that the joint TOA and

AOA statistics can be easily specified in a compact form and adjusted for different T-R separation distances. While in some sense the models represent the physical properties of the channel, in order to closely model these effects geometric channel models generally must be location specific and thus do not provide much flexibility in the independent selection of channel parameters.

Statistical spatial channel models use statistical distributions to represent signal parameters. The user is free to choose different distributions to characterize the different channel parameters such as TOA, AOA etc. The parameters characterizing these distributions are obtained from extensive measurement data. Refinements in the model are a direct consequence of increasing the volume and accuracy of the measurement set. Since this thesis focuses primarily on statistical spatial models, Section 3.6.(1) provides a brief overview of previous work in statistical spatial channel modeling focusing on UWB signals.

The term angle spread has been used consistently in this chapter and is defined as follows.

$$\sigma_{ang} = \sqrt{\frac{1}{n-1}\sum_{i=1}^{n}\left(\theta_i - \hat{\theta}\right)^2} \tag{3.12}$$

where θ_i is the AOA of the i^{th} multipath component and $\hat{\theta}$ is the mean AOA of n multipath components. σ_{ang} is a measure of how spread the AOA values are.

3.6.(1) Previous work in UWB spatial channel characterization

The most significant attempt at spatial modeling of wideband signals is the joint time-space model proposed in [Spen97], [Spen00] based on a dedicated spatial measurement campaign conducted in an indoor building environment. A system that collected time and angle-of-arrival data at 7 GHz was used in the measurement campaign. A chirp signal with a bandwidth of 500 MHz was transmitted resulting in an effective pulsewidth of approximately 3 ns. The system was capable of resolving multipath arrivals in space and time with a resolution of 6° and 3 ns respectively. Analysis of the measurement data showed the existence of a clustering pattern in the AOA and the TOA. The mean angle of each cluster was found to be uniformly distributed over all angles. The distribution of

AOA within the clusters was approximately Laplacian, with angular spreads (σ_{ang}) ranging from $22°$ to $26°$ per cluster. The TOA information was fit to a slightly modified version of the Saleh-Valenzuela model. Another important point worth mentioning is that the model assumed independence between the time and the angle-of-arrival statistics. i.e. there was no correlation between excess delay of the multipath component with its angle of arrival. Even though the measurements were not quite UWB bandwidth, it was one of the first efforts to comprehensively model the spatial and temporal features of the channel since most of the research efforts previously had focused on the temporal nature only.

The other significant work in ultra-wideband spatial channel modeling was done by Cramer [Cram02a] based on the measurements conducted by the Ultra-Lab at USC. A 500ps UWB pulse was used to sound the channel and data collection was attempted for various locations with 49 closely spaced points (over a 1m grid) per location. A variant of the CLEAN algorithm called the Sensor-CLEAN algorithm (presented in Chapter 3) was used to obtain the TOA and AOA of the resolvable multipaths. The findings for the AOA distribution were similar to [Spen97]. However, the measured angular spreads were slightly larger (although comparable) at $38°$. It is suggested that σ may be a function of the architecture of the building. It would also be possible that this difference may be due to the different fractional bandwidths and center frequencies employed in the experiments.

In any case, this motivates the need to take additional measurements directed towards understanding the spatio-temporal nature of the channel. One of the objectives of the MPRG measurement campaign that was described in Chapter 2 was to collect such information.

3.6.(2) Angle of Arrival (AOA) Distribution

A new channel model termed the Split-Poisson Model was presented in [Venka04], which consists of the generation of a *fixed* number (the exact number depends on the transmit power) of time-shifted clusters of Poisson arrivals. This models the temporal small-scale statistics of the measurement data extremely accurately. It was demonstrated in terms of delay statistics and Rake receiver energy capture that the Split-Poisson model

was a better statistical match to the measured data than the Saleh-Valenzuela, Δ − K and other models. The goal of this section is to arrive at an accurate spatial model for the measurement data in terms of the AOAs of multipath components and as a result, spatial correlation.

Based on the results of the Sensor-CLEAN algorithm applied on the NLOS measurement data certain intuitive patterns in the distribution of the AOA's could be observed. Figures Figure 3-17 and Figure 3-18 show the AOA and the TOA of the different multipath components at two different measurement locations. The early arriving multipaths appear to be clustered in a relatively small range of AOA's. This can be clearly discerned from Figure 3-19 which is an Amplitude vs. AOA plot for the first 20 ns and the last 70 ns obtained for all measurement locations (by normalizing the AOA from each set of measurements by the LOS direction)

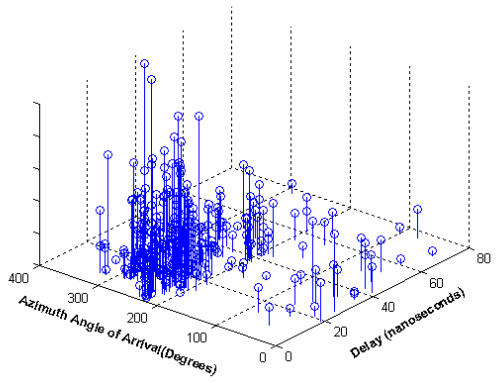

Figure 3-17 Amp and AOA vs TOA for Position 6

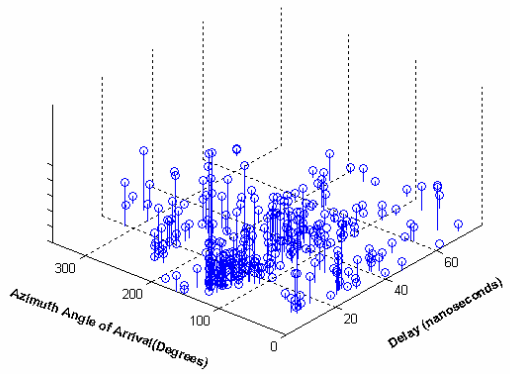

Figure 3-18 Amp and AOA vs TOA for Position 2

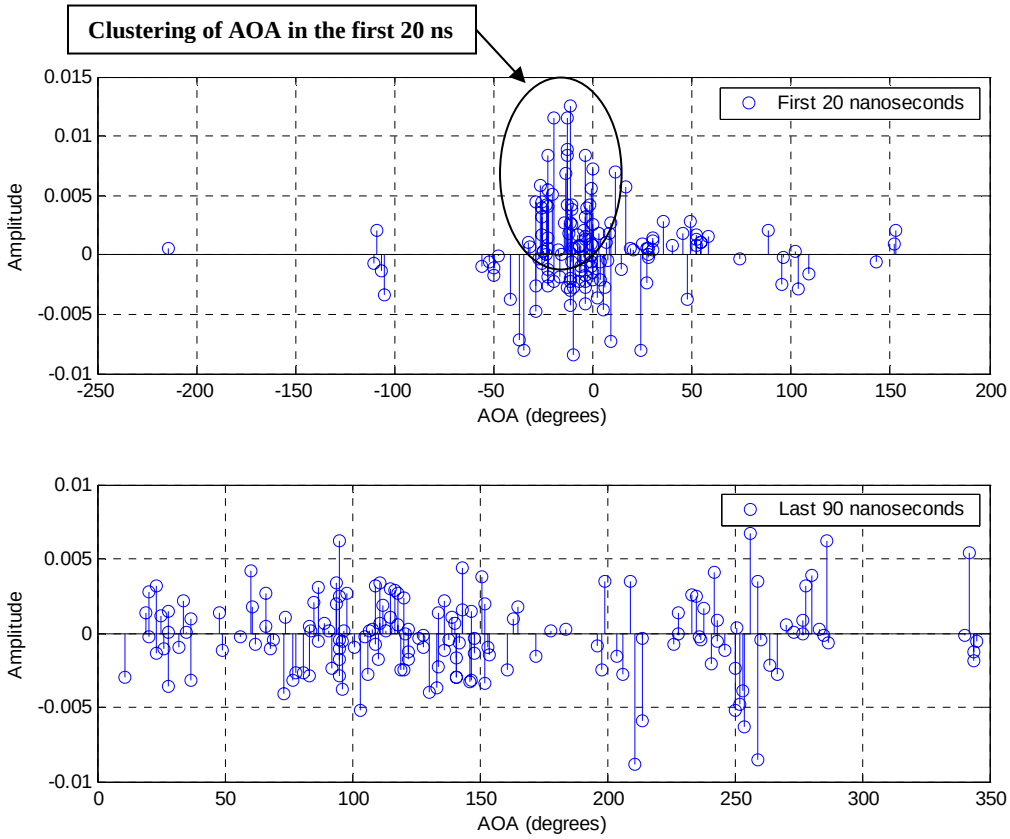

Figure 3-19 AOA distribution for the first 20 ns and last 70 ns (for all measurement locations)

The following conclusions can thus be drawn based on the results from all measurement locations.

- The AOAs corresponding to the (stronger) earliest arriving paths (first 20 ns) appear to arrive principally from the same direction (consistent with the LOS direction)
- The AOAs corresponding to the subsequent diffuse multipath do not appear to be concentrated in any specific direction and appear to be distributed uniformly over all directions.

Assuming an elliptical model for the scatters as was shown earlier in Figure 2-7 it is evident that the variance in the AOA's in the initial 20 ns part of the signal is less than the variance after 20 ns. In addition to clustering of multipath in the temporal domain, clustering in angles is also observed in the intial (roughly 20 ns) part of the signal.

PDF's of the multipath AOA's for the first 20 are presented in Figure 3-20 and Figure 3-21 for two measurement positions. Significant clusters at azimuth angles of 60 and 120 degrees are observed in the initialpart of the signal for the two figures. The mean value of the AOA is related to the Tx-Rx orientation relative to the geometry of the location. The data appears to be well-modeled by a Laplacian distribution with a standard deviation of approximately 10 degrees. Figure 3-22 and Figure 3-23 plot the empirical histogram of the received AOA for the latter 70ns. It can be seen that that the data is closer to a uniform distribution. Other measured locations exhibit a similar trend.

The observations can be explained as follows. The first arriving paths are most likely to coincide with either a direct path (even in NLOS measurements) or from a single dominant reflection and tend to be more prominent in the received signal. However, later delays may undergo multiple reflections or reflect from more numerous and distant reflectors. Since those reflectors are more evenly distributed around the transmitter and receiver, paths are received from all directions. This also coincides nicely with the observations from the spatial correlation measurements presented in Section 3.5

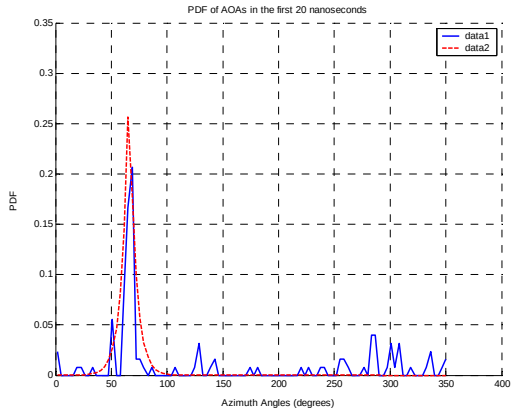

Figure 3-20 Histogram of AOAs and Postulated PDF for initial 25 nanoseconds for Position 1.

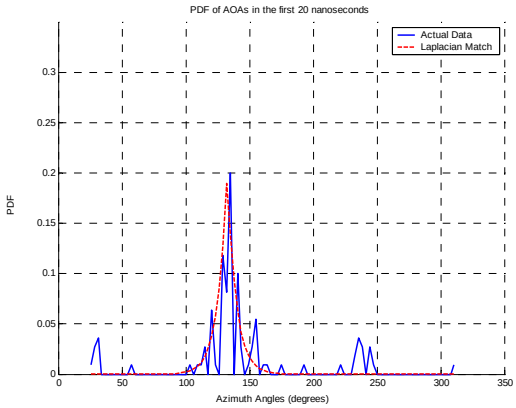

Figure 3-21 Empirical Histogram and Postulated PDF of AOAs for initial 20 ns for Position 2

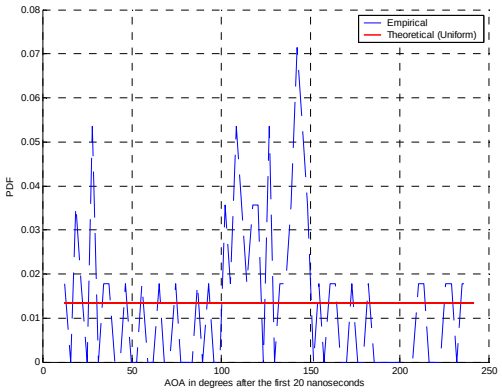

Figure 3-22 Distribution of AOAs after the first 20 nanoseconds for Position 1.

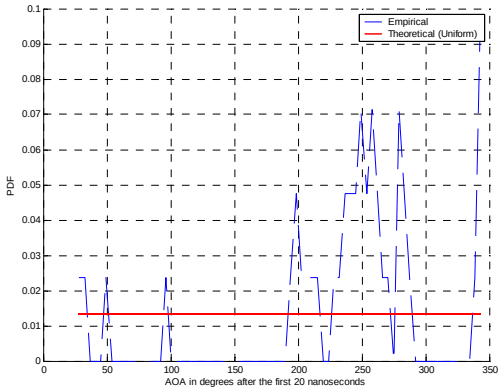

Figure 3-23 Distribution of AOAs after the first 20 nanoseconds for Position 2.

The path AOA's from all the measurement locations obtained in the first 20 ns are normalized around the approximate LOS direction (for each measurement set) and plotted on the same graph in Figure 3-24. A Laplacian distribution with $\sigma = 10^{\circ}$ is fit to the data. Also, Figure 3-25 shows the AOA distribution after the first 20 ns from the entire measurement set approximated to a uniform distribution. In addition to the simplicity in generating the uniform distribution, it is shown later through spatial correlation statistics that this approximation is a good one.

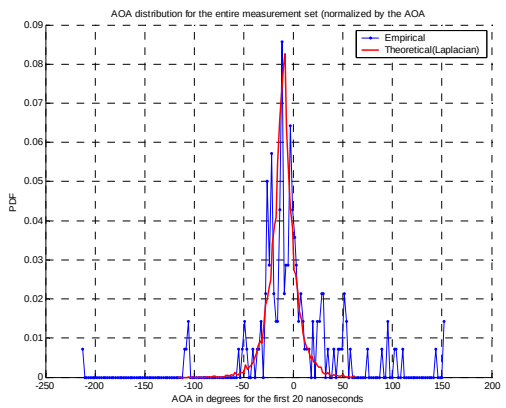

Figure 3-24 AOA for the first 20 ns over the entire measurement set obtained by normalizing the AOA's in the LOS direction. A Laplacian distribution with a standard deviation of 10 degrees is fit to the empirical data

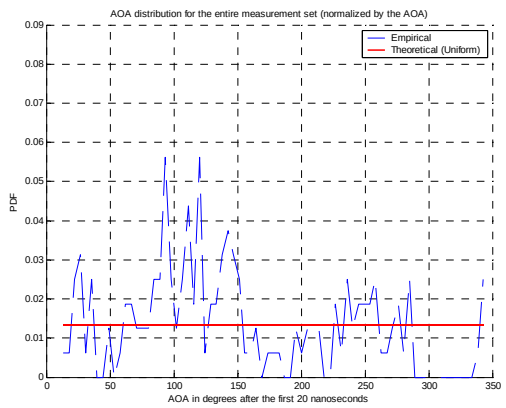

Figure 3-25 AOA after the first 20 ns from the entire measurement set roughly approximated by a uniform distribution.

3.7 A Spatial-Temporal Channel model for UWB indoor propagation

The observations in Section 3.6 are incorporated into a spatial channel model by extending the temporal model from [Venka04] into the spatial domain by taking the AOA information into account. Specifically, components arriving in the first several nanoseconds will be modeled as coming from roughly the same direction. In contrast, paths arriving later in the signal will be modeled as arriving uniformly from all directions.

Like the two "clusters" modeled in the temporal domain, the spatial-temporal model also has two "clusters" in the spatial domain. Every multipath component belonging to the first cluster is assigned an AOA angle taken from a Laplacian distribution. The mean AOA corresponds to the LOS direction and standard deviation is taken to be 10° based on the distribution of measured AOA's. Note that the mean is related to the relative transmitter-receiver orientation. Each path in the second cluster is assigned an AOA taken from a uniform distribution over $[0^{\circ}\ 360^{\circ}]$. This is shown in Figure 3-26

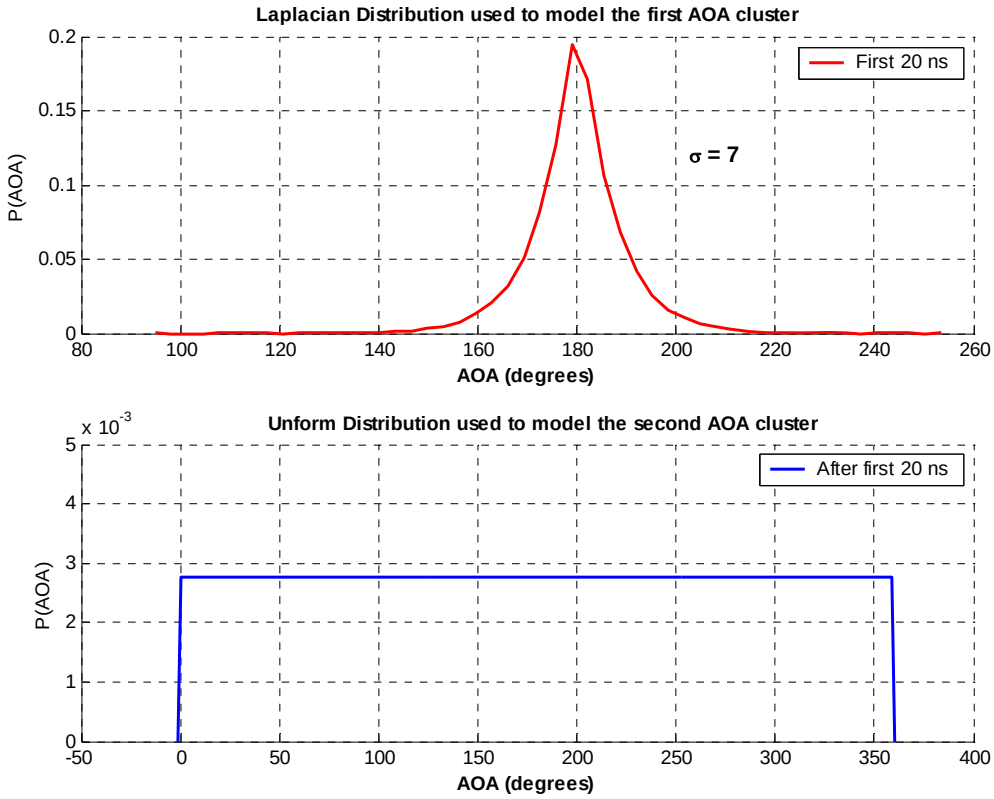

Figure 3-26. Laplace and uniform distributions to model initial and latter AOAs

The procedure for generating a set of CIR's based on the Spatial-temporal model is as follows:

1. Assign the number of grid elements, the spacing between grid positions and a reference position on the grid. The relative orientation of the grid is such that the grid is either perpendicular or parallel to the straight line drawn from the transmitter to the reference position on the grid. The model would generate a CIR for every position in this grid.
2. Generate a CIR using the parameters of the Split-Poisson model. This is considered the CIR seen at the reference position of the grid. The procedure for generating a single Split-Poisson CIR can be obtained from [Venka04]. For current purposes, it can be assumed that the CIR consists of two temporal clusters, each cluster having a different decay rate.
3. Assign an AOA to each multipath component in the following manner

a. The paths corresponding to the first 20 ns of the profile are assigned an AOA corresponding to a Laplacian distribution with a mean value equal to the LOS direction and standard deviation of 10^o.
b. The path's corresponding to the temporal segment after the first 20 ns are assigned an AOA drawn from a uniform distribution from 0^o to 360^o.

4. For spatial locations other than the original reference position, each path is shifted by a delay that corresponds to the AOA of the specified multipath component and the relative location of the receive antenna. In other words, the relative time delay of the path at a position on the grid would be dependent on the AOA of that path. This is similar to the algorithm used to generate the template waveform in Section 2.3.(1)
5. The set of profiles obtained correspond to the channel at different positions in a local area. Note that it is assumed that the number of paths for all the positions is the same for one instance of the model. These can be convolved with the transmitted pulse shape to obtain the received signal at each position.

Comparison with measurement data

In order to compare the performance of this modified model with the measured data, we generate the spatial correlation of both the measured and model received signals over distance. The correlation is calculated separately for the early and late arriving paths. The pulse used to generate the received signals is a 200 ps Gaussian pulse.

Figure 3-27 shows that a good match is achieved between the modeled and the measured spatial correlation curves for both clusters. The correlation is stronger in the first cluster, because the path AOAs variance is small.

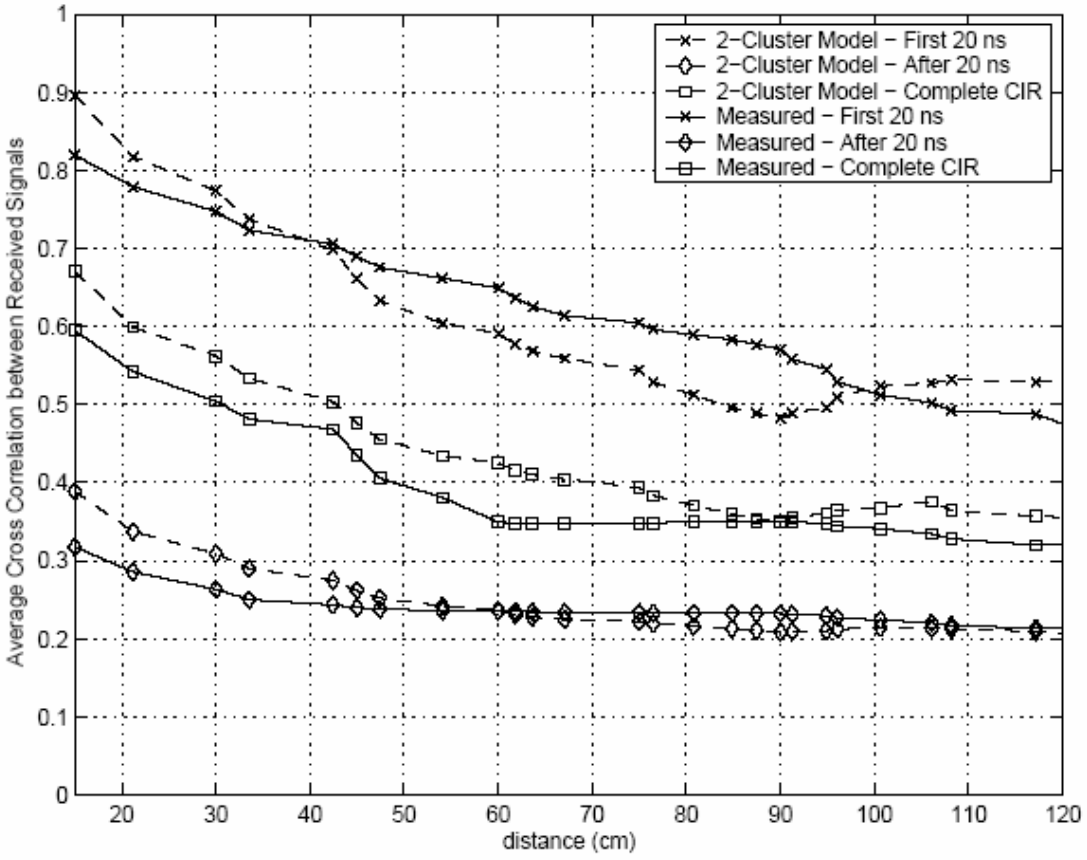

Figure 3-27. Results of the 2-D model compared with actual data. The average correlation co-efficient between adjacent signals in the profile is plotted versus the distance between the positions

It must be noted that there are significant differences between the model proposed in this thesis to the ones proposed in [Cram02a] and [Spen97]. Firstly, this model assumes a degree of dependence between AOA and the TOA. In other words paths arriving earlier(within 20 ns or so) constitute one cluster and are modeled as a Laplace distribution with a much smaller variance than the paths arriving later and constituting another large cluster (uniform distribution from 0 to 360 degrees).

Both of the above mentioned references assume independence between the temporal and the spatial features of the channel and the existence of multiple clusters. Additionally, each cluster had its angles following a Laplacian distribution, whose standard deviation was greater than the results presented in this thesis.

Apart from the impact of the environment (number of scatterers etc.), various other factors like the transmit power of the pulse and the accuracy of the deconvolution

algorithm influence the results to some extent. For example it is possible that had a much stronger pulse (>5 watts) been used to sound the channel, a different clustering pattern may have been obtained with potentially different distributions. With that in mind, it is stressed that the model presented in this thesis would be a good fit for low power (<1 Watt) indoor NLOS UWB channels, which is the range of interest for most indoor UWB applications.

3.8 Conclusions

UWB signals are relatively immune to spatial fading in terms of total received energy. However the energy captured by a 1-finger Rake exhibits wide variation. The spatial correlation (i.e. correlation between closely spaced points) was investigated for UWB signals. It was seen that the correlation is both a function of the spatial distance and the excess delay. Earlier parts of the signal appear more correlated than the rest of the signal. This was also seen in the AOA distribution of the received multipaths. The paths arriving in the first 20 ns had a smaller angle spread while paths arriving later appeared almost uniformly distributed in AOA. This observation was incorporated into an extension the Split-Poisson model [Venka04] to a 2-dimensional model that incorporated spatial and temporal statistics of the channel. The model was compared to empirical data and shown to be a good match.

Chapter 4. Antenna Diversity applied to Interference Mitigation

Ultra Wideband systems will necessarily co-exist with narrowband systems. The interference to and from narrowband services is a function of the number and the distribution of the narrowband devices, their spectral content and their radiated power levels. The FCC mask restricts UWB radiated power for communication systems to -41.3 dBm/MHz in the frequency range from 3.1 – 10.6 GHz. Even though UWB systems with moderate to high data rates still enjoy a high spreading gain relative to narrowband systems due to the large transmission bandwidth, the low energy per pulse makes them susceptible to nearby narrowband radio systems using a bandwidths up to a few MHz. In many such cases, the received power of the narrowband interferer (NBI) is a few tens of a dB higher than both the desired signal and the noise power. If such an interferer is not properly suppressed, the receiver may be jammed and the system performance will be seriously degraded. Classic techniques that have been successfully applied in spread spectrum systems to suppress NBI may be applied with slight modification to mitigate NBI and improve performance in a UWB system. However, many of these techniques assume at least chip-rate sampling. Such sampling rates may make such interference mitigation techniques impractical in UWB systems. Thus, we seek techniques which can be simply implemented in analog, explicitly those which exploit the spatial properties of the UWB channel.

This chapter introduces a simple NBI mitigation scheme using multiple receive antennas based on the spatial fading properties of UWB signals. The difference in spatial fading between UWB signals and narrowband signals is highlighted and the concept of interference diversity is described. The SINR improvement is investigated through statistical analysis. The performance of the system is evaluated through BER simulations.

4.1 Interference cancellation techniques for UWB

While NBI suppression has been investigated thoroughly for wideband spread spectrum systems (particularly CDMA), techniques specific to UWB signals are still limited. In

[Hamm02] the level of interference caused by different narrowband and other wideband radio systems like UMTS/WCDMA on UWB is studied. Two different types of UWB systems are considered, time hopped (TH) and Direct Sequence Spread Spectrum (DSSS). The impact of a narrowband interferer on the UWB receiver is most severe when the pulse is at the same frequency as the narrowband signal and the signal and the interferer are 180° out of phase [Hama02]. The effect of the proper selection of pulse shape in terms of the derivatives of the Gaussian pulse to lessen the effect of NBI is also illustrated.

The effect of NBI on a DSSS UWB system is also mentioned in [Foer02c]. The reference suggests the importance of the spreading code design for a DSSS UWB system to provide robustness to certain forms of NBI

If the interferer's frequency is known then it may simply be removed using a notch filter. It is however of more interest to develop an adaptive solution capable of canceling interference at any frequency across the band. Solutions which are applied in the analog front end are preferable to digital backend solutions since the latter require extremely high rate sampling. Reference [Donl04b] discusses two analog front-end interference cancellation techniques. The first technique digitally estimates the narrowband interference (without sampling the UWB signal) and produces an RF estimate to perform the narrowband cancellation in the analog domain. Two estimation techniques, an LMS algorithm and a transversal filter, are compared according to their error performances. Such techniques have been applied successfully previously for NBI cancellation in CDMA systems and also for the UWB domain [Mck03b]. The second solution performs real-time Fourier analysis using transform domain processing. The signal is converted to the frequency domain using a chirp Fourier transform and filtered according to the UWB spectrum. This technique is also characterized in terms of bit error rate performance. Further discussion is provided on chirp filter bandwidths, center frequencies, and the applicability of the technology to UWB.

The use of the MMSE algorithm in mitigating NBI using a Rake receiver is presented in [Boub03]. In this technique, the received signal is sampled at the pulse repetition frequency after passing through a Rake receiver. The samples are linearly combined using the MMSE criteria and the weights are chosen to suppress the NBI. The

decision is based on these linearly combined samples. It is shown that a P-Rake that selects the first L_p paths performs almost as well as the S-Rake that combines the strongest L_p paths for SIR levels as high as -20 dB. A major advantage of the MMSE scheme is that explicit knowledge of the interference parameters is not required. The selection of the best L_p paths to combine is a multi-dimensional optimization problem and may be explored further.

It must be mentioned that most of the current interference suppression schemes assume that the UWB signal has already been acquired. Unfortunately, acquisition can be difficult to achieve at low SINR's. Schemes (such as the one presented in this chapter) that can suppress interference before synchronization are thus desirable.

4.2 Introduction to Interference Diversity

Traditional diversity techniques exploit the spatial fading characteristics of wireless channels in order to combat temporal fading. A number of diversity schemes are implemented successfully in wireless systems including spatial diversity, temporal diversity and frequency diversity. Spatial diversity through the use of antenna arrays is particularly useful in narrowband systems that have slow temporal fading properties. An antenna array system is composed of a collection of spatially separated antenna elements. The spacing depends on the type of environment and frequency band. The outputs from these elements are typically combined to improve the overall SNR of the system. The combining types are often divided into two classes: diversity combining techniques and beam-forming techniques. Diversity combining schemes include Maximal Ratio Combining, Equal Gain Combining and Selection Diversity, which have been examined extensively in the literature[Jak93].

This chapter introduces the concept of 'interference diversity' using multiple receive antennas based on the spatial fading properties of UWB signals and narrowband interferers. Like traditional diversity, this scheme takes advantage of spatial fading properties but is closer to the concept of interference averaging that is exploited in CDMA systems.

4.2.(1) Spatial Energy variation of UWB signals and NBI

Consider a UWB system where $p(t)$ is the transmitted pulse and $i(t)$ is a narrowband interferer in the vicinity of the UWB receiver. If the pulse duration of $p(t)$ is sufficiently small $i(t)$ can be modeled as a tone over the duration of the UWB pulse even if it is digitally modulated.

Neglecting the effect of the antennas, the received UWB signal $s_p(t)$ at the p^{th} antenna is the transmitted signal convolved with the channel impulse response between the transmitter and the p^{th} antenna ($h_{sp}(t)$). This can be represented as

$$s_p(t) = \int_{-\infty}^{+\infty} p(t) * h_{sp}(t) dt \tag{4.1}$$

Similarly, the interference seen at the p^{th} antenna can be expressed as

$$i_p(t) = \int_{-\infty}^{+\infty} i(t) * h_{ip}(t) dt \tag{4.2}$$

where $h_{ip}(t)$ is the channel impulse response between the narrowband interference source and the p^{th} antenna.

The received total UWB signal energy in one symbol duration can be calculated as $E_s = \int_0^{T_s} {s_p}^2(t) dt$ where T_s is the symbol duration which is assumed to be longer than the maximum multipath delay. Similarly, the total received interference energy is $E_i = \int_0^{T_s} {i_p}^2(t) dt$.

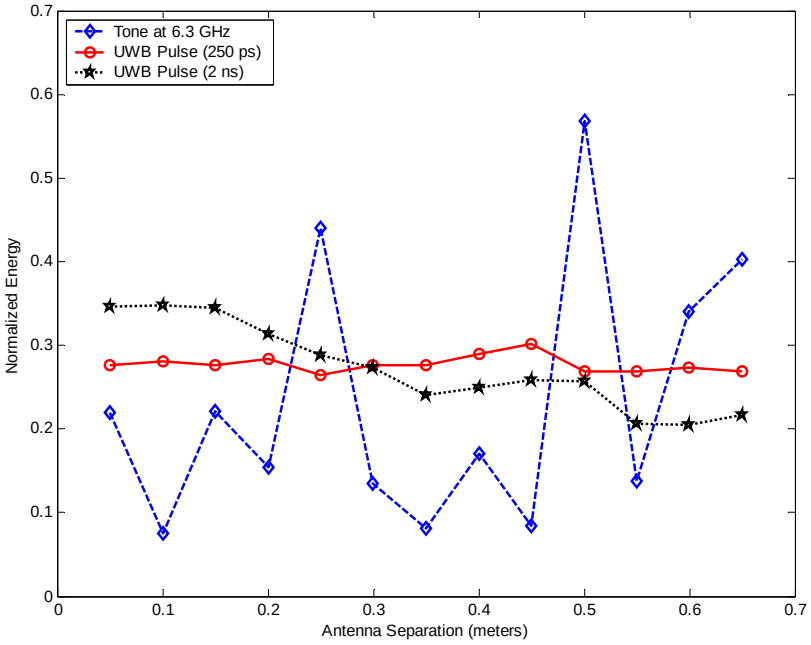

Figure 4-1 Received signal energies at different antenna separations

Figure 4-1 shows the energy content of an example NBI and the UWB signal over a 70cm linear segment obtained using the NLOS channel model described in Chapter 3. Note that the energy is normalized such that it is unity on average. The energy content of the NBI varies wildly over the linear region as compared to the energy content of the UWB signal. Further, the 200 ps UWB pulse shows less variation in energy across the grid than the 2 ns pulse due to more resolvable paths (i.e., larger bandwidth). In this chapter, it is shown how this relative immunity of the UWB signal to spatial fading can be exploited to provide "interference diversity".

4.2.(2) Probability distribution of Signal-to-Interference Ratio (SIR) at the receiver

Consider a received signal containing a UWB signal and a NBI in a NLOS channel. The received signal after perfect matched filtering (i.e., assuming perfect energy capture for the UWB signal) is

$$r(t) = \gamma_s s(t) + \gamma_i i(t) \tag{4.3}$$

where s(t) and i(t) are unit power signals representing the UWB desired signal and the NBI respectively after matched filtering. γ_s and γ_i are the resulting (possibly complex) amplitudes of the signals after matched filtering. The distribution of γ_s^2 (normalized to the mean) and assuming real pulses is shown in Figure 4-2 . The standard deviation is approximately 0.7 dB.

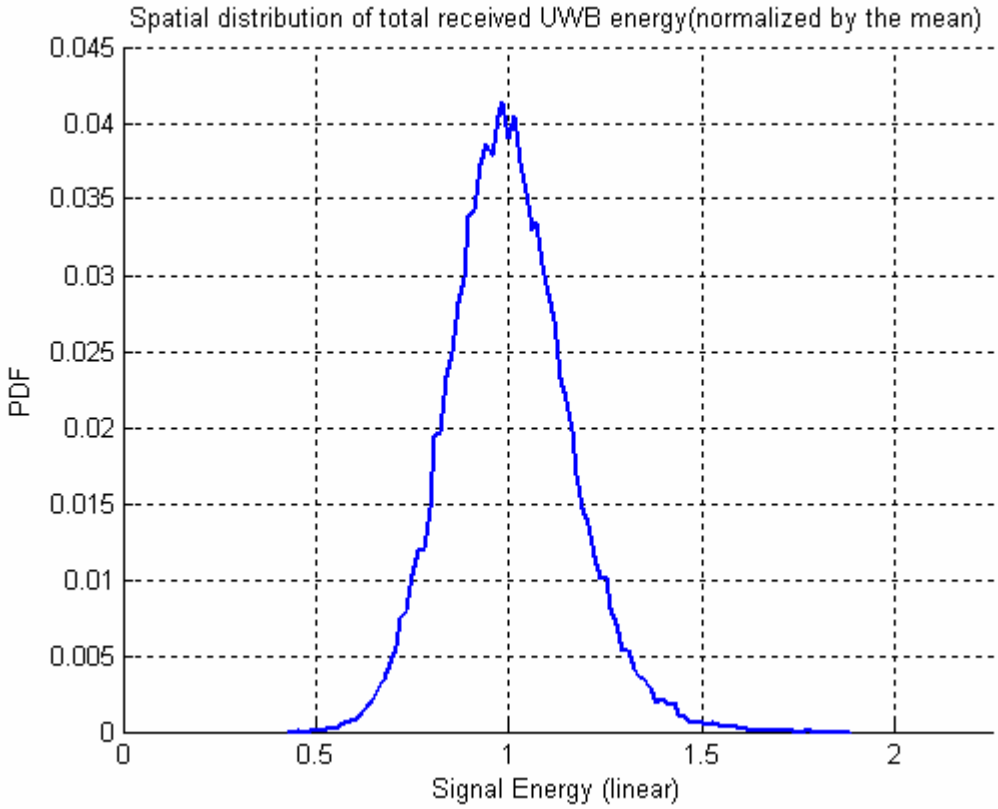

Figure 4-2 Empirical distribution of total received UWB energy using Gaussian pulse (See Chapters 2 and 3)

Due to the low spatial variation, γ_s^2 can be approximated to be a constant $\overline{S}$ over a local area. The approximation is fairly accurate due to the low value of σ, particularly when compared to the variation of a narrowband signal. It is shown later that the error due to this approximation is negligible. Thus, we can model the desired signal energy distribution to be

$$f_S(S) = \delta\left(S - \overline{S}\right) \tag{4.4}$$

Now, since this is a NLOS channel, the classic Rayleigh fading model can be applied to the narrowband interference signal (i.e. γ_i is approximately a Gaussian random variable) and if the scatterers are assumed to be uniformly distributed about the receiver, signals received on antennas separated by more than one half the carrier wavelength are independent. The resulting energy, $|\gamma_i|^2$ over a local area is therefore Chi-square distributed with 2 degrees of freedom, which is also an exponential distribution. Figure 4-3 shows the energy distribution for the NBI obtained through simulation using the channel model described in Chapter 3 and the resulting distribution is closely modeled by a Chi-square distribution.

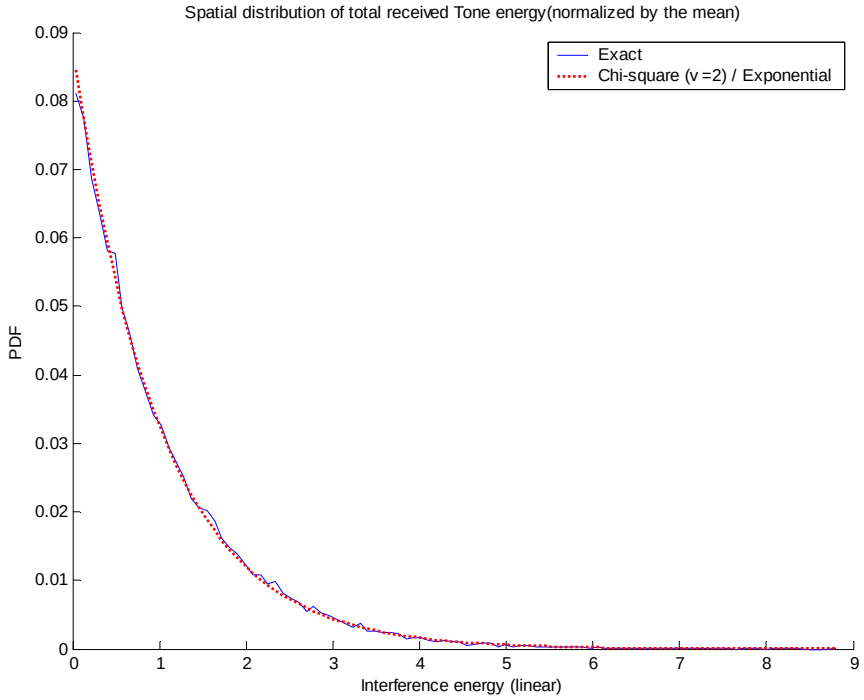

Figure 4-3 Simulated and Theoretical Distributions of Interference Energy captured by the optimum matched filter

Hence,

$$f_I(I) = \frac{1}{\bar{I}} e^{-\frac{I}{\bar{I}}} \tag{4.5}$$

where $\bar{I}$ is the average interference energy

Let χ be the ratio of the signal power to the interference power at the output of the matched filter. We need to obtain the distribution of χ. Now, since *S* is approximated by a constant value $\overline{S}$,

$$\chi = \frac{\overline{S}}{I} \tag{4.6}$$

or,

$$I = \frac{\overline{S}}{\chi} \tag{4.7}$$

The distribution function (probability density function) of χ is given as [Papo02]

$$\begin{aligned} f_\chi(\chi) &= f_I(I)\left|\frac{d}{d\chi}(I)\right| \\ &= f_I\left(\frac{\overline{S}}{\chi}\right)\left|\frac{d}{d\chi}\left(\frac{\overline{S}}{\chi}\right)\right| \\ &= f_I\left(\frac{\overline{S}}{\chi}\right)\left|-\frac{\overline{S}}{\chi^2}\right| \\ &= \frac{\overline{S}}{\chi^2} f_I\left(\frac{\overline{S}}{\chi}\right) \end{aligned} \tag{4.8}$$

Substituting the value of $f_I(I)$ from Equation (4.5)

$$\begin{aligned} f_\chi(\chi) &= \frac{\overline{S}}{\chi^2}\frac{1}{\overline{I}} e^{-\overline{S}/\chi\overline{I}} \\ &= \frac{\overline{\chi}}{\chi^2} e^{-\overline{\chi}/\chi} \end{aligned} \tag{4.9}$$

where $\overline{\chi} = \frac{\overline{S}}{\overline{I}}$ is approximately the average Signal-to-Interference ratio (SIR)

Figure 4-4 shows the distribution of SIR's obtained using the theoretical distribution given in equation (4.8) and a plot using the simulated channel model in Chapter 3 for the

UWB signal energies narrowband interference. Note that the approximation of the spatial distribution as a constant causes negligible mismatch.

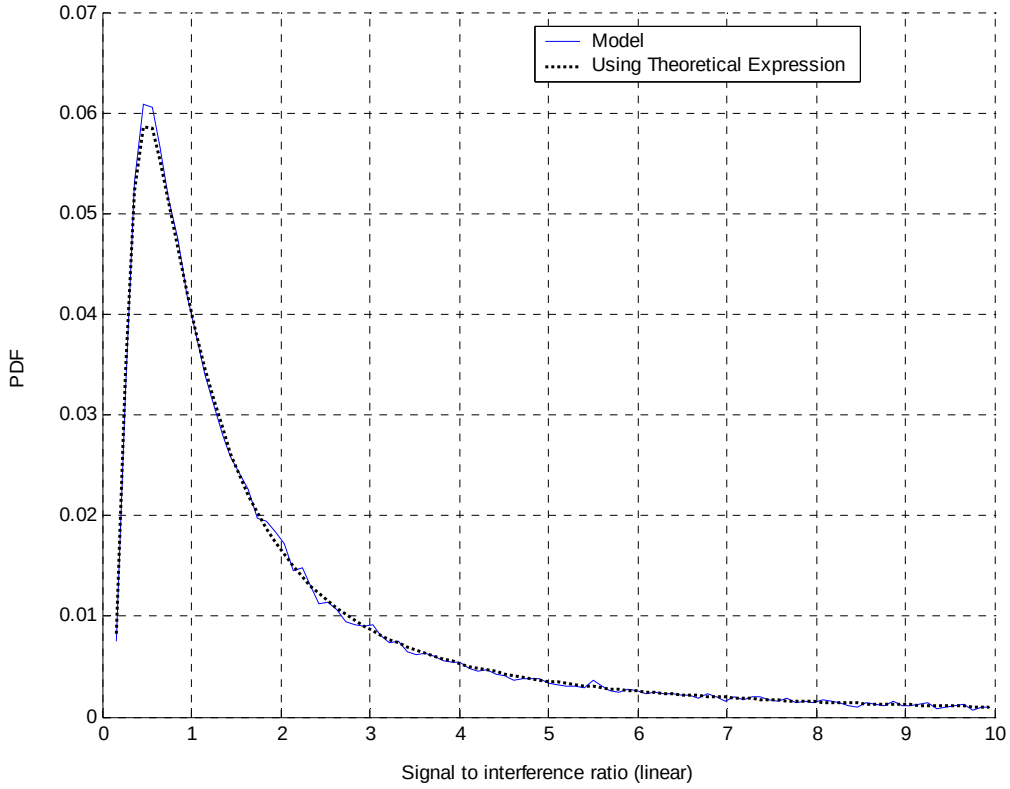

Figure 4-4 Theoretical and Simulated (based on measurement data) SIR distribution when optimum matched filter is used

4.3 Selection Diversity Improvement

In a conventional selection diversity scheme the desired signal power varies substantially across spatially separated antennas (provided the antenna separation is greater than one half of a wavelength in NLOS channels), whereas the noise power remains constant. The received signal with the highest instantaneous power among all antennas is fed to the demodulator improving the effective SNR of the system. In the case of UWB, the desired signal energy exhibits little variation across different antennas and hence it is possible

that diversity techniques may not be needed. However, since the received power of a narrowband interferer varies substantially across multiple antenna elements, diversity schemes can improve the SIR or SINR of the system as opposed to the SNR.

Consider M independent fading channel realizations, i.e. a diversity array with M receive antennas. Let the instantaneous SIR on each branch be χ_i. As shown in the previous section, the pdf of χ_i is

$$p(\chi_i) = \frac{\overline{\chi}}{\chi_i^2} e^{-\overline{\chi}/\chi_i} \tag{4.10}$$

The probability that a single branch has an instantaneous SIR less than some threshold χ is

$$\begin{aligned} \Pr[\chi_i < \chi] &= \int_0^{\chi} p(\chi_i) d\chi_i \\ &= \int_0^{\chi} \frac{\overline{\chi}}{\chi_i^2} e^{-\overline{\chi}/\chi_i} d\chi_i \end{aligned} \tag{4.11}$$

Making the substitution,

$$\begin{aligned} &\frac{1}{\chi_i} = t \\ &\therefore -\frac{d\chi_i}{\chi_i^2} = dt \end{aligned} \tag{4.12}$$

and changing the limits of integration:

$$\begin{aligned} &\chi_i = 0, t = \infty \\ &\chi_i = \chi, t = \frac{1}{\chi} \end{aligned} \tag{4.13}$$

we have

$$\begin{aligned}\Pr[\chi_i < \chi] &= \int_{\infty}^{\frac{1}{\chi}} -\bar{\chi} e^{-\bar{\chi}t} dt \\ &= \frac{-\bar{\chi}\left[e^{-\bar{\chi}t} \right]_{\infty}^{\frac{1}{\chi}}}{-\bar{\chi}} \\ &= e^{-\frac{\bar{\chi}}{\chi}}\end{aligned} \tag{4.14}$$

Now since the diversity branches are independent[5] (a reasonable assumption indoors),, the probability that all M independent diversity branches receive signals which are simultaneously less than some specific SIR threshold χ is

$$\begin{aligned}P_M(\chi) &= \Pr[\chi_1, \chi_2 ...., \chi_M < \chi] \\ &= \left(\Pr[\chi_i < \chi]\right)^M \\ &= \left(e^{-\frac{\bar{\chi}}{\chi}} \right)^M \\ &= e^{-\frac{M\bar{\chi}}{\chi}}\end{aligned} \tag{4.15}$$

The simulated (using measurement based model) and the theoretical CDF's for the received SIR's when interference diversity is used is shown in Figure 4-5. Note that the *y*-Axis is in log-scale. This figure illustrates the maximum achievable SIR when the system is operating at a particular outage probability when multiple antennas are used. For example consider that the system is operating at an outage probability of 0.1, the maximum achievable SIR would improve by approximately 3 dB with the addition of 1 antenna and 3 more 3 dB when 4 antennas are used. Conversely, the figure can also be interpreted as follows; If the operating SIR is known the outage probability can be calculated for different antenna configurations.

[5] Spatial correlation for UWB signals based on empirical results was presented in (Section 3.5). UWB signals on a whole exhibit less spatial correlation, although parts of the signal may.

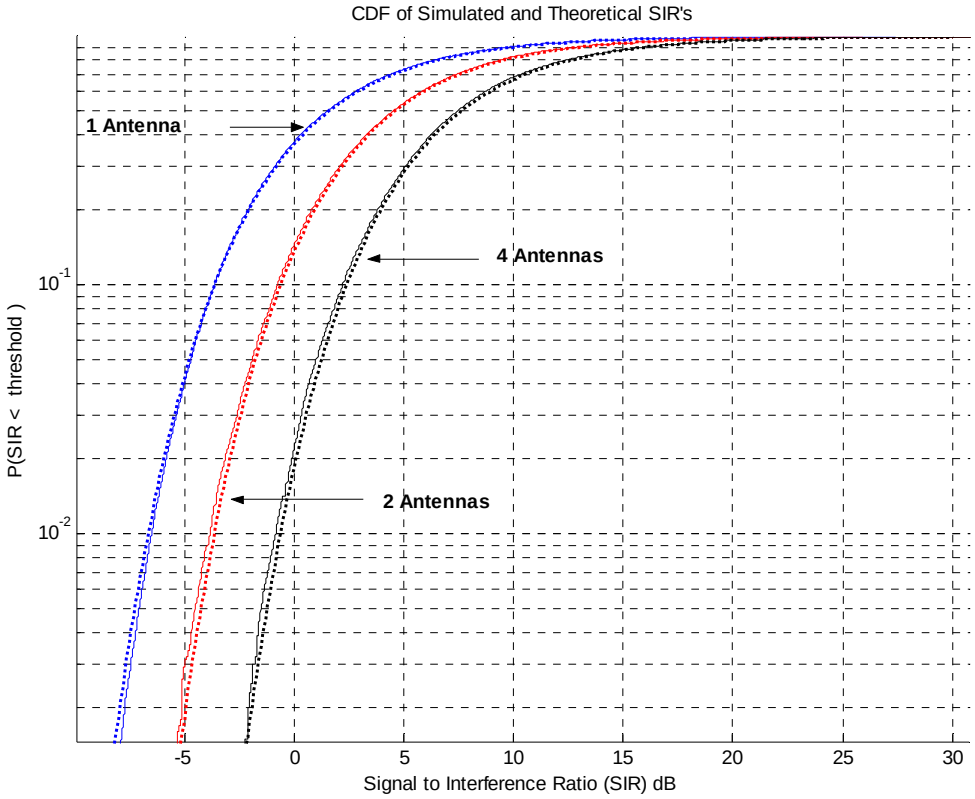

Figure 4-5. Theoretical and simulated CDF's for SIR with and without interference diversity

The theoretical and the simulated values match very well for the case when no diversity is used (i.e. 1 Antenna) and also for the cases where interference diversity is employed. The SIR improves by approximately 3 dB when 2 antennas are used compared to the scenario where there is only one receive antenna. Additionally it can be seen that the diversity advantage is obtained at low values of SIR. At very high values this advantage diminishes.

4.3.(1) Probability density function

The PDF of χ when M branches are used can be obtained by differentiating the CDF $P_M(\chi)$

Thus,

$$
\begin{aligned}
p_M(\chi) &= \frac{d}{d\chi} P_M(\chi) \\
&= \frac{d}{d\chi}\left(e^{-\frac{M\bar{\chi}}{\chi}}\right) \\
&= \frac{M\bar{\chi}}{\chi^2} e^{-\frac{M\bar{\chi}}{\chi}}
\end{aligned}
\tag{4.16}
$$

Figure 4-6 shows the inverse CDF (or $\Pr[\chi_i > \chi]$) plotted against SIR

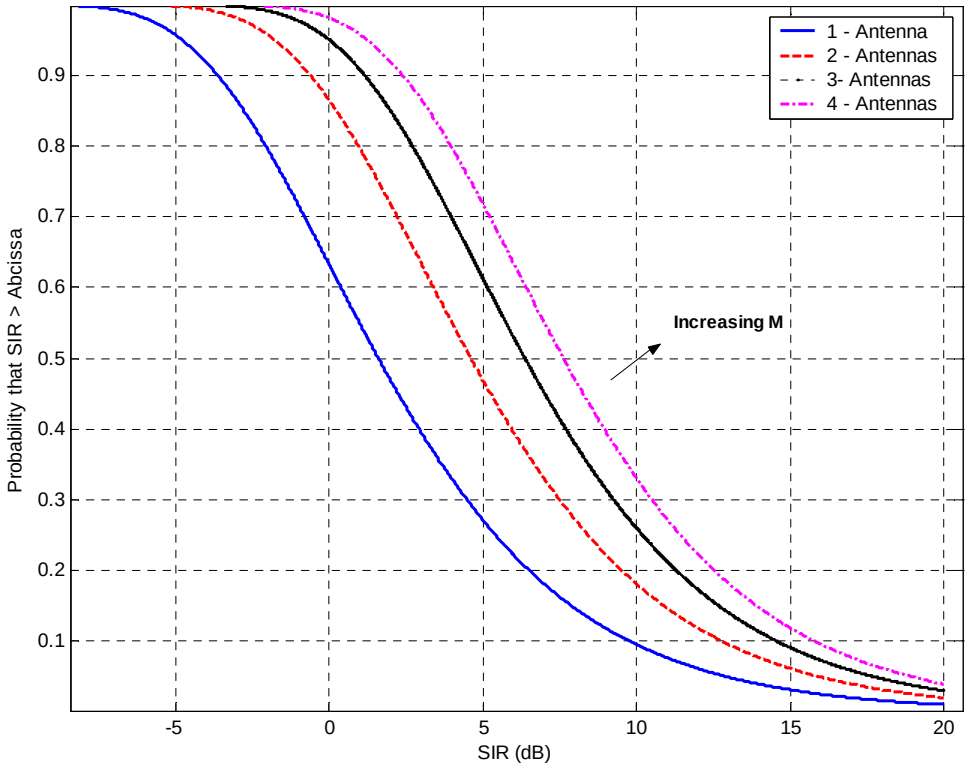

Figure 4-6 Inverse CDF's for the SIR with increasing number of antennas using theoretical expression

4.3.(2) Improvement using Interference diversity

$P_M(\chi)$ is the probability of all M simultaneously branches failing to achieve an instantaneous $SIR = \chi$. The probability that $SIR > \chi$ for one or more branches is given by

$$\begin{aligned} \Pr[\chi_i > \chi] &= 1 - P_M(\chi) \\ &= 1 - e^{-\frac{M\bar{\chi}}{\chi}} \end{aligned} \tag{4.17}$$

In order for the effective SIR to be greater than χ for at least 90 percent of the time,

$$\begin{aligned} 1 - e^{-\left(\frac{M}{\bar{\chi}/\chi}\right)} &= 0.9 \\ \bar{\chi} &= -\frac{\chi}{M}\ln(0.1) \end{aligned} \tag{4.18}$$

We thus require that the average SIR ($\bar{\chi}$) be greater than $-\frac{\chi}{M}\ln(0.1)$. Obviously, increasing M reduces the average SIR requirement. In fact, every doubling of the number of antennas M, reduces the required SIR by 3dB, similar to the SNR improvement for coherent antenna arrays.

4.4 Introduction of noise in the system

So far, we have assumed that only interference was present in the system. Consider the scenario where there is also noise present and the noise power and the interference power are roughly equal (i.e., the system is not interference dominated). In this scenario the system is both interference and noise limited. Figure 4-7 compares the distribution of only the interference signal and the interference and noise when the powers are equal. Notice the slight mismatch between the 2 distributions (with only interference and with interference and noise). Figure 4-8 shows that there is negligible difference between the theoretical SIR distribution (without noise) and the SIR

distribution considering the noise and the interferer (Note that in this case the SNR is identical to the SIR)

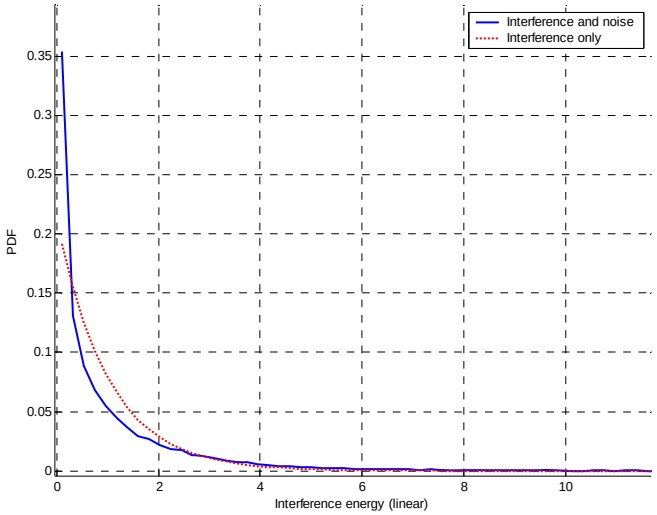

Figure 4-7 Distribution of interference and interference with comparable noise power.

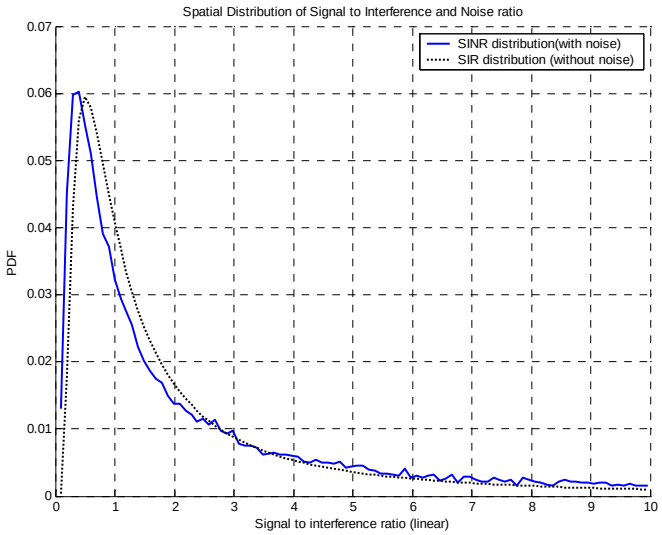

Figure 4-8 SIR distribution with noise and the theoretical distribution assuming no noise is present.

4.5 System Implementation

In conventional selection diversity systems selection diversity is practically implemented by feeding the signal with highest average received power (as opposed to measuring SNR) to the demodulator. This is effective due to the fact that the noise power is constant from antenna to antenna and thus the signal with the greatest received power is most likely to have the largest desired signal power. In the proposed interference diversity system, the weakest signal is chosen to be fed to the demodulator. This can be explained as follows. The UWB signal power is approximately constant while the interference power is Chi-square distributed and thus varies form antenna to antenna. Thus, an increase in the SIR of the system is equivalent to less interference power and consequently lower overall received power.

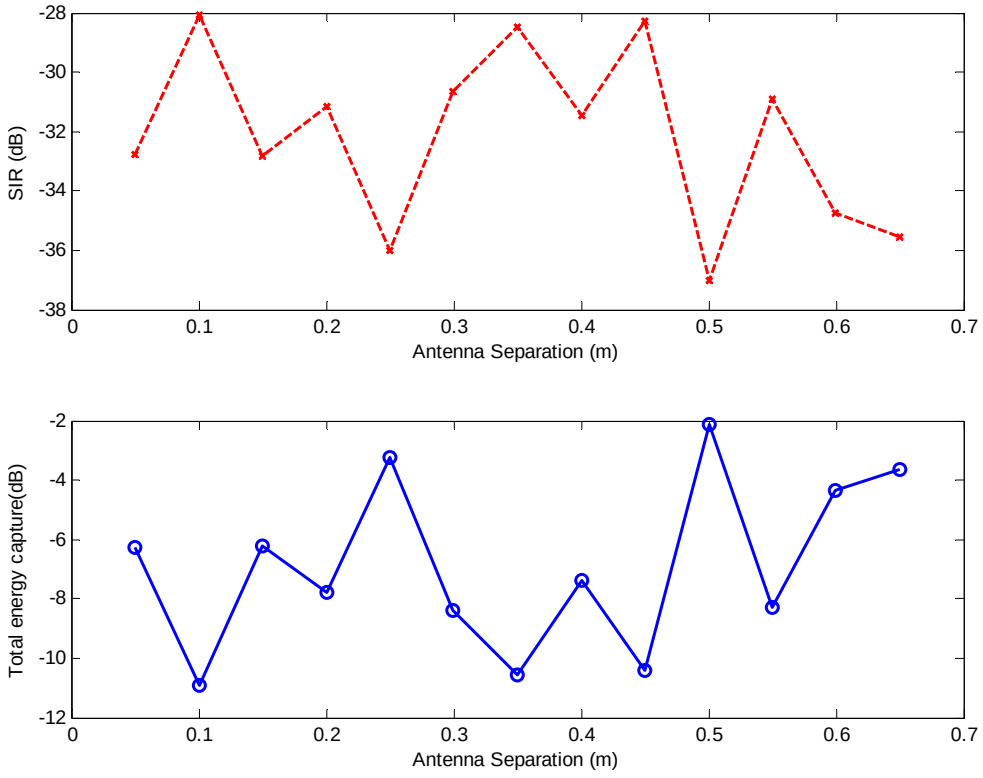

Figure 4-9 Simulation of total energy capture (normalized by LOS pulse, bottom) and the actual SIR (top) using channel model of Chapter 3

Plots of the simulated (using the channel model of Chapter 3) SIR and received energy values are shown in Figure 4-9. When, the SIR increases the actual received energy at the output of the antenna decreases. As the pulse-width increases the UWB signal varies more substantially in space (i.e. across different antenna elements) violating our constant energy assumption and degrading performance. It is possible that for small changes in the power of the interferer, this scheme may not function perfectly. However as long as the variance of the NBI fading is greater than that of the UWB signal this scheme on an average would improve the performance of the system. The system model is shown in Figure 4-10

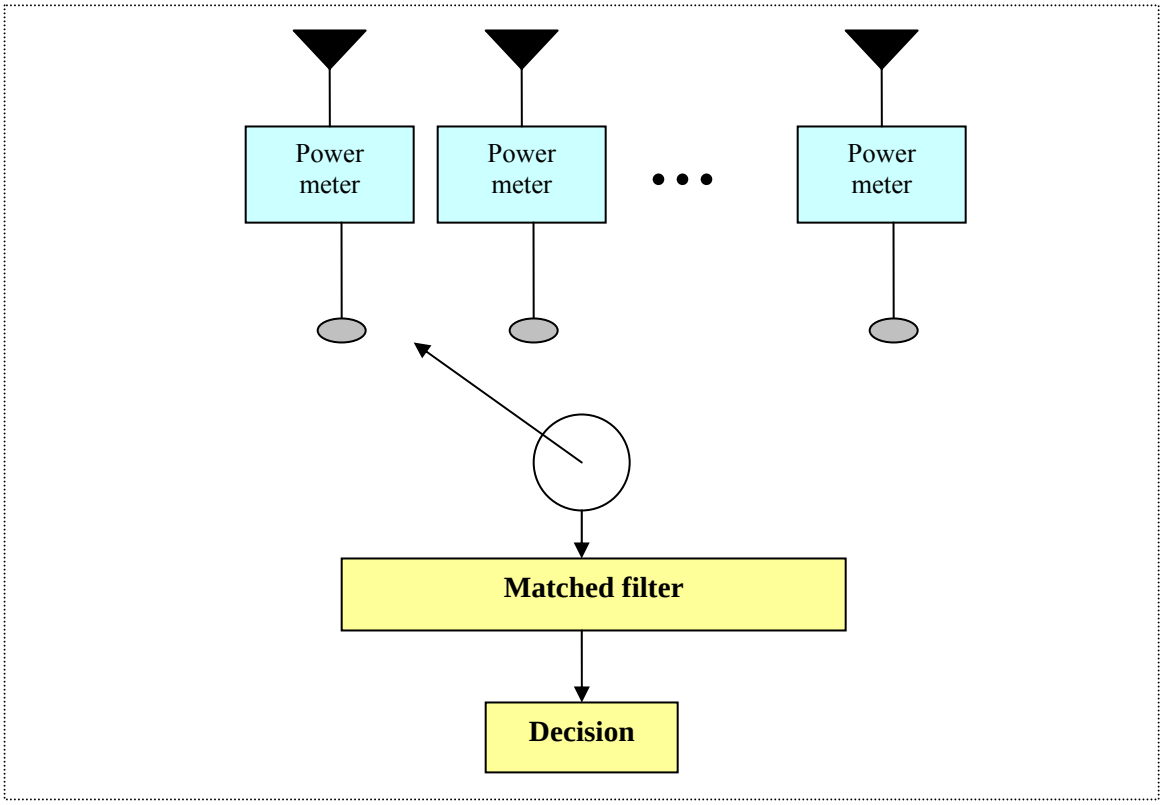

Figure 4-10 System model for the interference diversity scheme

A simulation using BPSK modulation at an E_b / N_o of 6 dB was carried out with 1, 2 and 4 receive antennas to gauge the performance of the system. The Spatial-Channel model presented in Chapter 3 was used in the simulations. As described above the signal having the lowest power was fed to the demodulator. The BER performance of the system is shown in Figure 4-11. It is observed that there is a 2-3 dB improvement in performance

with respect to NBI with the addition of one extra antenna and 5-7dB improvement with four antennas depending on the target BER. Note that only a single receiver is required. Note also that the performance benefits are the most when the system is not noise limited and yet the BER is not so high that little gain is achievable.

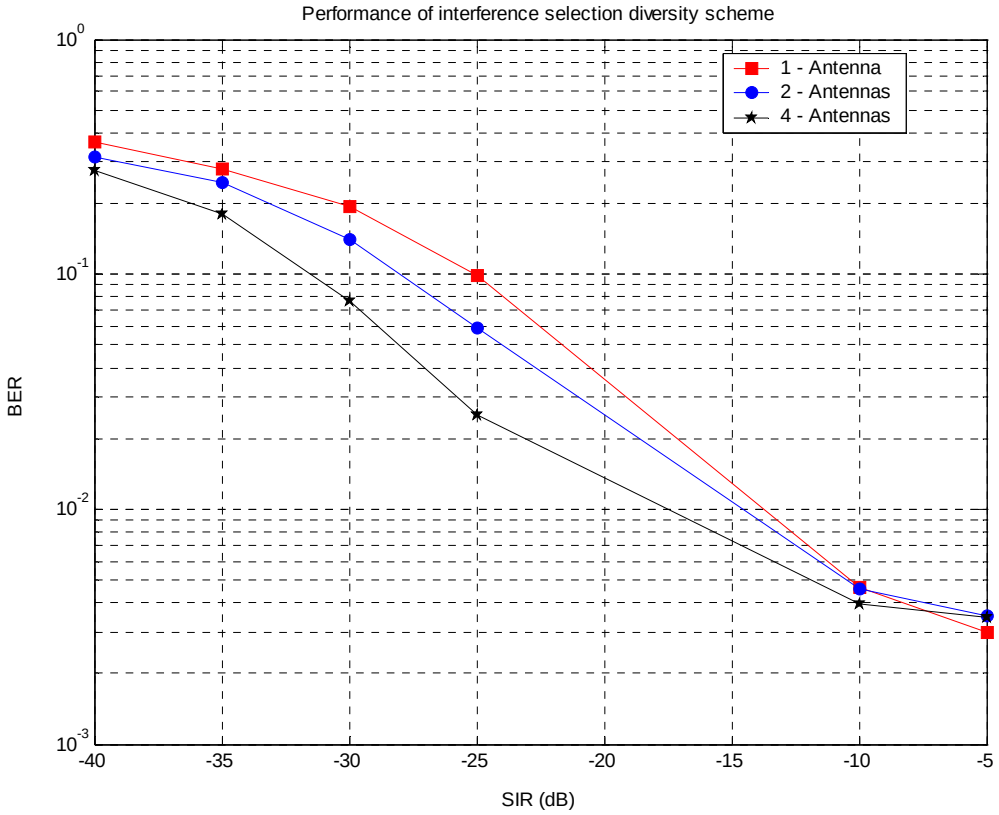

Figure 4-11. Simulated BER Performance of the interference diversity scheme

4.6 No interference scenario

The practical implementation of the scheme described above selects the signal with smallest average power and feeds it to demodulator. In cases where there is no interferer in the system (i.e. only noise is present) this could result in degraded performance since we will lose signal SNR.

The CDF of the received signal energy is plotted in Figure 4-12 for the following two scenarios.

a. When there is only one antenna

b. When 2 antennas are used and the signal with lower energy is selected.

This is equivalent to evaluating the performance without interference and only noise. As expected there is a slight loss in performance (< 0.25 dB), although the loss is negligible and can practically be ignored.

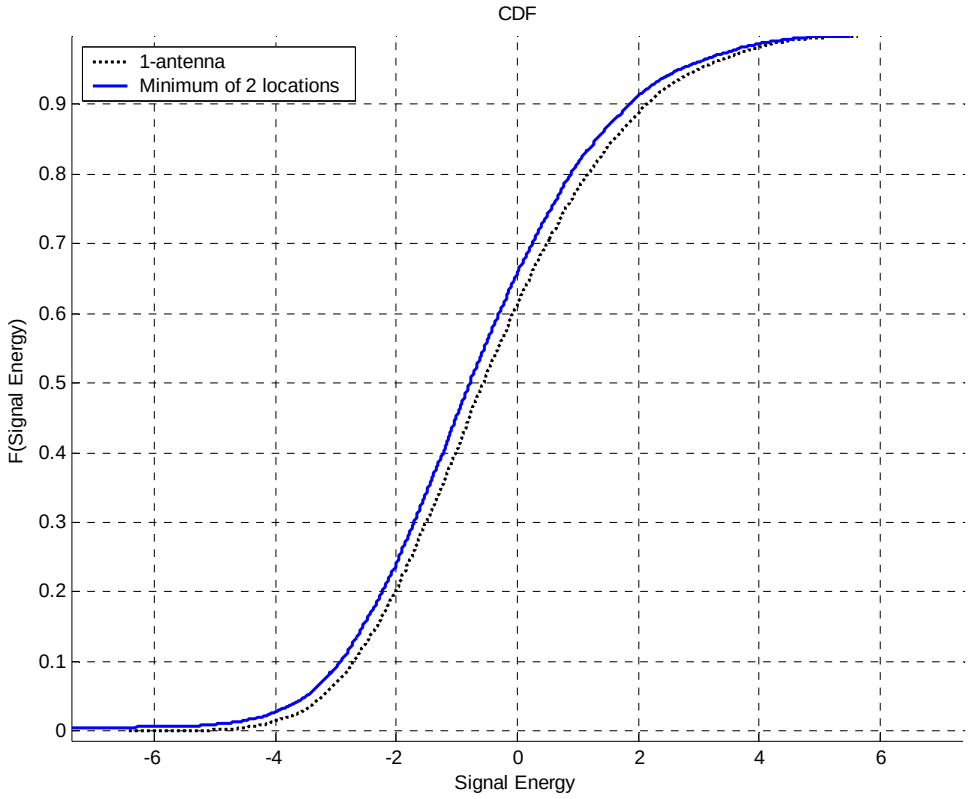

Figure 4-12 Comparison of the CDF's of received SIR's when there is no interferer in the system

4.7 Theoretical performance of the system

The interference diversity combiner selects the signal with the smallest interference power. The interference powers follow a Rayleigh distribution. Hence,

$$f_x(x) = \frac{1}{\bar{X}} e^{-\frac{x}{\bar{X}}} \tag{4.19}$$

The CDF is given by

$$F_x(x) = 1 - e^{-\frac{x}{\bar{X}}} \tag{4.20}$$

Order statistics can be used to determine that distribution of the minimum of the interference powers. To explain, let $X_1 ..., X_M$ be a sample of M variates (in this case interference powers at the outputs of M antennas). Let them be re-ordered so that $Y_1 < Y_2 ... < Y_M$. Then Y_i is called the i^{th} order statistic [Hogg95]

If X has probability function $f(X)$ and distribution function $F(X)$, then the probability function of Y_R is given as

$$f_{Y_r} = \frac{M!}{(r-1)!(M-r)!}\left[F(\beta)\right]^{r-1}\left[1-F(\beta)\right]^{M-r} f(\beta) \tag{4.21}$$

A special case is the minimum order statistic $Y_1 \equiv \min_j \left(X_j\right)$

Substituting $r = 1$ in equation (4.21),

$$f_{Y_r} = M\left[1-F(X)\right]^{M-1} f(X) \tag{4.22}$$

From equation 4.21

$$\begin{aligned} f_{y1}(y_1) &= M\left[1-\left(1-e^{-\frac{x}{\bar{X}}}\right)\right]^{M-1} \frac{1}{\bar{X}} e^{-\frac{x}{\bar{X}}} \\ &= \frac{M}{\bar{X}} e^{-\frac{Mx}{\bar{X}}} \end{aligned} \tag{4.23}$$

The first moment of this distribution is given by

$$\begin{aligned} \bar{X}_M &= \frac{M}{\bar{X}} \int_0^\infty x e^{-\frac{Mx}{\bar{X}}} dx \\ &= \frac{M}{\bar{X}} \left(\frac{\bar{X}}{M}\right)^2 \\ &= \frac{\bar{X}}{M} \end{aligned} \tag{4.24}$$

In effect the mean interference power is reduced by the number of antennas used. This expression can be used to predict the performance of the system, when M diversity branches are used in the interference diversity scheme.

The transmitted signal can be represented as:

$$s_{tr} = \sum_{k=1}^{N} d_k w_{tr}\left(t - kT_f\right) \tag{4.25}$$

where $w_{tr}(t)$ is the pulse shape used. The energy contained in the pulse is given by $E_p = \int_{-\infty}^{\infty} N_p w_{tr}^{\ 2}(t)dt$ where N_p is the number of pulses used to represent one bit. The normalized auto-correlation of the pulse is given by $R(\tau) = \frac{\int_{-\infty}^{\infty} w_{tr}(t)\, w_{tr}(t-\tau)\, dt}{E_p}$. d_k is the value of the k^{th} bit and is equal to -1 or 1 and they are assumed to occur with equal probability at a rate T_f^{-1}. It is assumed that the channel stays constant over the time that the N_p bits are sent.

The signal received at the j^{th} antenna can be expressed as

$$r_j(t) = \sum_{l=0}^{L-1}\sum_{k=1}^{N} \alpha_l d_k w_{tr}\left(t - kT_f - \tau_l\right) + i_j(t) + n(t) \tag{4.26}$$

where $n(t)$ is the additive white Gaussian noise with a power spectral density $N_o/2$. $i_j(t)$ is the interfering signal received at the j^{th} antenna.

The receiver structure consists of one or more antennas but one correlator (or matched filter). The template waveform is given by $p(t) = \sum_{l=0}^{L-1} \alpha_l w_{tr}\left(t - \tau_l\right)$.

Consider the case with one received antenna. The matched filter output for the k^{th} bit is given by

$$\begin{aligned} Z^1{}_k &= \int_0^{T_b} r_1(t)p_1(t)dt \\ &= \int_0^{T_b} \left(\sum_{l=0}^{L-1} \alpha_l d_k w_{tr}\left(t-\tau_l\right) + i_j(t) + n(t) \right).p_1(t)dt \\ &= S^j{}_k + I^j{}_k + N^j{}_k \end{aligned} \tag{4.27}$$

where, $N^{j}{}_{k} = \int_{0}^{T_b} n(t)\, p_1(t)\, dt$ is the variance of the noise term and is equal to $\frac{N_0}{2}$.

$S^{j}{}_{k} = d_k \int_{0}^{T_b} \sum_{l=0}^{L-1} \alpha_l{}^2 w_{tr}{}^2 (t-\tau_l) dt$ is the energy of the signal and $I^{1}{}_{k} = \int_{0}^{T_b} i_1(t)\, p_1(t) dt$ where

$= E_p$ $= R_{it}(0)$

$R_{it}(\tau) = \int_{0}^{T_b} i_1(t)\, p_1(t-\tau) dt$

Thus the contribution of the interference to the matched filter output is the cross-correlation between the matched filter template and the interfering signal. The distribution of this term depends on number of antenna elements used. The variance of this term $\sigma_I{}^2$ is related to frequency and the strength of the interferer and the width of the template waveform.

The decision statistic is Gaussian with a mean that is equal to the energy of the UWB pulse. The variance of the decision statistic is given by

$$\sigma^2 = \sigma_I{}^2 \big/ M + \sigma_n{}^2 \tag{4.28}$$

The BER probability at the output of the matched filter is given by

$$\begin{aligned} P_e &= Q\left(\sqrt{\frac{Ep}{\sigma^2}}\right) \\ &= Q\left(\sqrt{\frac{Ep}{\sigma_I{}^2 / M + \sigma_N{}^2}}\right) \end{aligned} \tag{4.29}$$

For the purpose of this analysis assume that there is no noise in the system (i.e. $\sigma_n{}^2 = 0$), Equation (4.29) reduces to

$$P_e = Q\left(\sqrt{\frac{E_p}{\sigma_I^2 / N}}\right)$$
$$= Q\left(\sqrt{\frac{NE_p}{I_o}}\right) \qquad (4.30)$$
$$= Q\left(\sqrt{N \cdot SIR}\right)$$

Note that the SIR is defined as $\frac{E_p}{I_o}$. The theoretical expression is compared to simulation (assuming a Rayleigh distribution for the interferer) in Figure 4-13. The simulation framework for the same was prepared by Jihad Ibrahim of MPRG. Note that the simulated and the theoretical curves match well in the absence of noise.

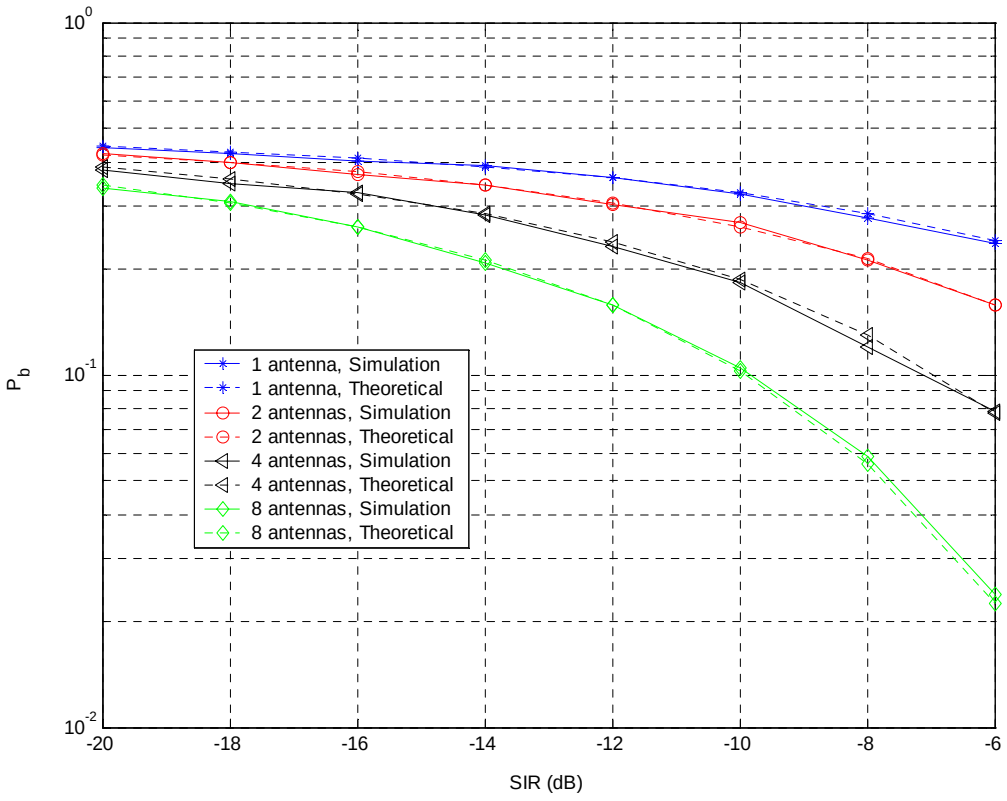

Figure 4-13 Theoretical and simulated curves for the interference diversity scheme in the absence of noise. (This simulation was carried out by Jihad Ibrahim of MPRG)

4.8 Conclusions

This chapter has shown that improvement in the SIR performance of UWB signals can be obtained using simple selection diversity. While the optimum matched filter was considered (i.e., total energy capture), similar analysis could also be applied to a Rake receiver with similar results. Note that for less than full energy capture, the UWB signal will exhibit more variation in the received signal energy, thus mitigating the effectiveness of the technique. Additionally, for situations where a line-of-sight component exists, the Rayleigh distribution should be exchanged for a Ricean distribution. This slightly reduces the effectiveness of the scheme and allows for further study.

Chapter 5. Conclusions and suggestions for future work

This thesis addresses two areas of interest in UWB, spatial channel modeling and interference suppression. Based on collected UWB measurement data, spatial characteristics of the UWB channel were discovered. Using information gleaned from these statistics a spatial channel model was postulated which matches the empirical data well. Further, the spatial characteristics of the UWB channel are utilized in introducing an interference mitigation scheme for narrowband interferers in the UWB domain.

In Chapter 1, a brief introduction to UWB was presented with an emphasis on impulse UWB. Chapter 2 provided a description of the UWB indoor measurement campaign conducted at the MPRG labs. Channel models for UWB are refined with the availability of more data and the indoor measurements presented in this thesis have contributed towards that goal. A two-dimension deconvolutional technique called the Sensor-CLEAN was applied to obtain AOA information of different multipath components. The implementation of this algorithm for the purpose of this thesis was discussed. A brief understanding of the performance limitations of the Sensor – CLEAN algorithm was achieved based on known artificial channel data.

Chapter 3 discussed the spatial characteristics of the UWB indoor channel. First and second order statistics of the received signal energy for an optimum matched filter and a Rake receiver were provided. Based on intuitive clustering observed in AOA, a new spatial channel model was proposed that incorporates the temporal and the spatial characteristics of the channel. This channel model differs from previous work in the sense that it assumes a level of dependence between the excess delay (in the form of multipath clusters) and AOA. Accuracy was verified by comparing the model to empirical data through spatial correlation statistics. This spatial model allows the simulation of multiple antenna UWB systems with good accuracy and greater simplicity since it consists of just two clusters.

A scheme to suppress NBI in UWB systems was presented in Chapter 4. This scheme uses multiple antennas and utilizes the low spatial fading of the UWB signal seen in Chapter 3. In contrast narrowband signals experience Rayleigh fading. This difference in fading statistics is utilized to propose a new interference mitigation scheme based on selection diversity. This simple technique allows for significant gain using multiple antennas. As opposed to schemes that provide superior performance after signal acquisition, this scheme mitigates the interference power before synchronization, proving particularly useful in scenarios where synchronization of the UWB signal is itself a difficult task. Since the scheme is based on the principle of selection diversity, only one receiver is required. Extension of the interference diversity scheme when there is a strong LOS component (and the narrowband interferer is Ricean) would be a useful addition. The gains accrued in this case would typically be lower than when the interferer is Rayleigh. Further a more practical scenario of employing a Rake receiver with different number of fingers could be considered in this scheme instead of the optimum matched filter.

5.1 Original contributions of this thesis

This thesis has made following original contributions to existing UWB literature

- Characterization of the spatial features of the UWB channel based on indoor channel measurements.
- Development of a spatial-temporal channel model
- A NBI mitigation scheme using multiple receive antennas

5.1.(1) List of Publications

B. M. Donlan, S. Venkatesh, V. Bharadwaj, R. M. Buehrer, "The Ultra-Wideband Indoor Channel", *Presented at the IEEE VTC Spring 2004*

V. Bharadwaj, R. M. Buehrer, "An interference suppression scheme for UWB using multiple receive antennas," accepted for publication, *IEEE Communication Letters*

S. Venkatesh, V. Bharadwaj, R. M. Buehrer, "Spatial Characterization of Ultra-Wideband Channels", To be presented *IEEE VTC Fall 2005*

References

[Bat03] A. Batra and al. Texas Instruments/Intel and al. Proposal for IEEE 802.15.3a Alternate PHY. IEEE 802.15.3a/document 267r3, November 2003.

[Boub03] N. Boubaker and K. B. Letaif, "A Low Complexity MMSE-RAKE Receiver in a Realistic UWB Channel and in the Presence of NBI," *IEEE*, pp. 233 – 137, 2003.

[Bueh03] R. M. Buehrer, W. Davis, A. Safaai-Jazi, and D. Sweeney, "Characterization of the Ultra-Wideband Channel," *2003 IEEE Conference on Ultra-Wideband Systems and Technologies*, pp. 26–31, Nov. 2003.

[Bueh04] R.M. Buehrer, W.A. Davis, A. Safaai-Jazi, and D. Sweeney, "Ultra-wideband Propagation Measurements and Modeling," DARPA NETEX Program Final Report, Jan. 2004.

[Cass01] D. Cassioli, M Z. Win, and A. F. Molisch, "A Statistical Model for the UWB Indoor Channel," in *Proc. IEEE VTS 53rd Vehicular Technology Conference*, vol. 2, pp. 1159–1163 , May 2001.

[Cass02] D. Cassioli, M.Z. Win, and A. F.Molisch, "The Ultra-Wide Bandwidth Indoor Channel: From Statistical Study to Simulations," *IEEE Journal on Selected Areas in Communications*, vol. 20, no. 6 , pp. 1247–1257, Aug. 2002

[Cram99] R. J.-M. Cramer, R. A. Scholtz, and M. Z. Win, "Spatio-Temporal Diversity in Ultra-wideband Radio," in *Proc IEEE Wireless Communications and Networking Conference*, vol. 2, pp. 888-892, 1999.

[Cram00] R.J.-M. Cramer, "An Evaluation of Ultrawideband Propagation Channels", PhD Dissertation, Dept. Elect. Eng., Univ. of Southern Calif., Los Angeles, CA, Dec. 2000.

[Cram02a] R. J.-M. Cramer, R. A. Scholtz, and M. Z. Win, "Evaluation of an Ultra-Wide-Band Propagation Channel," *IEEE Transactions on Antennas and Propagation*, vol. 50, no. 5, pp. 561–570, May 2002.

[Cram02b] R. J.-M. Cramer, R. A. Scholtz, and M. Z. Win , "Evaluation of an Indoor Ultra-Wideband Propagation Channel (doc.: IEEE P802.15-02/286-SG3a and IEEE P802.15-02/325-SG3a)," submitted to IEEE P802.15 Working Group for Wireless Personal Area Networks (WPANs), June 2002.
Available:http://grouper.ieee.org/groups/802/15/pub/2002/Jul02/

[Darp04] R. M. Buehrer et al, "UWB Channel Characterization and modeling", DARPA NETEX program final report, 2004.
Available: http://www.mprg.org/people/buehrer/ultra/darpa_netex.shtml

[Donl04a] B. M. Donlan, S. Venkatesh, V. Bharadwaj, R. M. Buehrer, and J.-A. Tsai, "The Ultra-Wideband Indoor Channel," *IEEE Vehicular Technology Conference,* 2004.

[Donl04b] B. M. Donlan, "Ultra-wideband Narrowband Interference Cancellation and Channel Modeling for Communications," Master's Thesis, Dept. of Electrical and Computer Engineering, Virginia Tech, Blacksburg, VA, Feb 2005.

[Erte99] R. B. Ertel, "Antenna Array Systems: Propagation and Performance," PhD. Dissertation, Dept. of Electrical and Computer Engineering, Virginia Tech, Blacksburg, VA, 1999.

[FCC02] Federal Communications Commission, First Report and Order, ET Docket 98-153,April 2002.

[Foer02a] J. Foerster, "Channel Modeling Sub-committee Report Final (doc.: IEEE 802-15-02/490r1-SG3a)," submitted to IEEE P802.15 Working Group for Wireless Personal Area Networks (WPANs), Feb. 2002. Available: http://grouper.ieee.org/groups/802/15/pub/2002/Nov02/

[Foer02b] J. Foerster and Q. Li, "UWB Channel Modeling Contribution from Intel (doc: IEEE P802.15-02/279-SG3a)," submitted to IEEE P802.15 Working Group for Wireless Personal Area Networks (WPANs), June 2002. Available: http://grouper.ieee.org/groups/802/15/pub/2002/Jul02/.

[Foer02c] J. Foerster, "The Performance of a Direct-Sequence Spread Ultra-Wideband System in the Presence of Multipath, Narrowband Interference, and Multiuser Interference," *IEEE Conference on Ultra Wideband Systems and Technology*, 2002.

[Fow90] C. Fowler, J. Entzminger, J. Corum, "Report: Assessment of Ultra-Wideband (UWB) Technology," OSD/DARPA Ultra-Wideband Radar Review Panel, R-6280,1990.

[Hama02] M. Hämäläinen, V. Hovinen, ., Tesi, R., Iinatti, J., M. Latva. "On the UWB System Coexistence With GSM900, UMTS/WCDMA, and GPS". *IEEE Journal Sele. Area. Comm. Vol 20. No 9.*, 2002.

[Hash93] H. Hashemi, "The Indoor Radio Propagation Channel," *Proceedings of the IEEE*, vol. 81, no. 7, pp. 943–968 , July 1993.

[Hogb74] J.A. Hogbom. "Aperture Synthesis with a Non-Regular Distribution of Interferometer Baselines", *Astron. and Astrophys. Suppl. Ser,* vol. 15,1974.

[Hogg95] Hogg, R. V. and Craig, A. T. *Introduction to Mathematical Statistics, 5th ed.* New York: Macmillan, 1995.

[Hibb04] D. J. Hibbard, "The impact of signal bandwidth on Indoor Wireless Systems in Dense Multipath Environments," Master's Thesis, Dept. of Electrical and Computer Engineering, Virginia Tech, Blacksburg, VA, 2004.

[Jak93] W. C. Jakes, Ed., *Microwave Mobile Communications*, New York: IEEE Press, 1993.

[Kein02a] J. Keignart and N. Daniele, "Subnanosecond UWB Channel Sounding in Frequency and Temporal Domain," *2002 IEEE Conference on Ultra Wideband Systems and Technology*, pp 25–30, May 2002.

[Kum04] N. Kumar, "MAC and Physical layer design for Ultra-Wideband Communication," Master's Thesis, Dept. of Electrical and Computer Engineering, Virginia Tech, Blacksburg, VA, 2004.

[Licu03] S. Licul, W. A. Davis, and W. L. Stutzman, "Ultra-Wideband (UWB) Communication Link Modeling and Characterization," *2003 IEEE Conference on Ultra-Wideband Systems and Technologies*, pp. 310–314, Nov. 2003.

[Mass51] Massey, F. J. Jr. "The Kolmogorov-Smirnov test of goodness of fit," *Journal of the American Statistical Association*, Vol. 46. 1951

[McK03a] D. R. McKinstry, "Ultra-Wideband Small Scale Channel Modeling and its Application to Receiver Design," Master's Thesis, Dept. of Electrical and Computer Engineering, Virginia Tech, Blacksburg, VA, 2003.

[McK03b] D. R. McKinstry and R. M. Buehrer, "LMS Analog and Digital Narrowband Rejection System for UWB Communications," *2003 IEEE Conference on Ultra-Wideband Systems and Technologies*, pp. 91–95, Nov. 2003.

[Muq03] A. H. Muqaibel, "Characterization of Ultra Wideband Communication Channels," Ph.D. Dissertation, Dept. of Electrical and Computer Engineering, Virginia Tech, 2003.

[Muqa03a] A. H. Muqaibel, A. Safaai-Jazi, A. M. Attiya, A. Bayram, and S. M. Riad, "Measurements and Characterization of Indoor Ultra-Wideband Propagation," *2003 IEEE Conference on Ultra-Wideband Systems and Technologies*, pp 295–299, Nov. 2003.

[Muqa03b] A. H. Muqaibel, A., Safaai-Jazi, A., Bayram, A., S. M. Riad, "Ultra wideband material characterization for indoor propagation", *2003 IEEE Antennas and Propagation Society International Symposium*, vol. 4, pp. 623–626.

[Papo02] A. Papoulis, and S. Unnikrishna Pillai, *Probability, Random Variables, and Stochastic Processes*. Fourth Edition, Boston, MA: McGraw Hill, 2002.

[Pret02] C. Prettie, D. Cheung, L. Rusch, and M. Ho, "Spatial Correlation of UWB Signals in a Home Environment," *2002 IEEE Conference on Ultra Wideband Systems and Technology*, pp. 65–69, May 2002.

[Qui02] R. C. Qui, "A Study of the Ultra-Wideband Wireless Propagation Channel and Optimum UWB Receiver Design," *IEEE Journal on Selected Areas in Communications*, vol. 20, no. 9, pp. 1628-1637, Dec. 2002.

[Rapp02] T.S. Rappaport, Wireless *Communications: Principles and Practice*, Second Edition, Upper Saddle River, NJ: Prentice Hall, 2002.

[Reed04] J. H. Reed, Ed., *An Introduction to Ultra Wideband Communication Systems*, Prentice-Hall, 2005.

[Rusc03] L. Rusch, C. Prettie, D. Cheung, Q. Li, M. Ho, "Characterization of UWB Propagation from 2 to 8 GHz in a Residential Environment," *IEEE Journal on Selected Areas in Communications*, submitted for publication

[Sale87] A. A. Saleh and R. A. Valenzuela, "A Statistical Model for Indoor Multipath Propagation," *IEEE Journal on Selected Areas in Communications*, vol. SAC-5, no. 2, pp. 128-137, Feb. 1987.

[Scha03] H. G. Schantz, "Introduction to Ultra-Wideband Antennas," *2003 IEEE Conference on Ultra-Wideband Systems and Technologies*, pp. 1–9, Nov. 2003.

[Scho98] R.A. Scholtz, M.Z. Win, J.M. Cramer, "Evaluation of the Characteristics of the Ultra-Wideband Propagation Channel," *1998 Antennas and Propagation Society International Symposium*, vol.2, pp.626–630.

[Scho93] R. Scholtz, "Multiple Access with Time-Hopping Impulse Modulation," *IEEE Military Communications Conference*, 1993, vol. 2, pp. 447-450.

[Scho97] R. A. Scholtz and M. Z. Win, "Impulse Radio," *Personal Indoor Mobile Radio Conference*. Sept. 1997.

[Spen97] Q. Spencer, M. Rice, B. Jeffs, and M. Jensen, "A statistical model for the angle-of-arrival in indoor multipath propagation," in *Proc. IEEE Veh.Technol. Conf.*, 1997, pp. 1415-419.

[Spen00] Q. Spencer, B. Jeffs, M. Jensen, and A. Swindlehurst, "Modeling the statistical time and angle of arrival characteristics of an indoor multipath channel," *IEEE J. Select. Areas Commun.*, vol. 18, pp. 347–360, Mar.2000.

[Venka04] Venkatesh, S.; Ibrahim, J.; R. M. Buehrer, "A new 2-cluster model for indoor UWB channel measurements," Antennas and Propagation Society Symposium, 2004. IEEE Volume 1, 20-25 June 2004 Page(s):946 - 949 Vol.1.

[Wel01] M. L. Welborn, "System Considerations for Ultra-wideband Wireless Networks," *IEEE Radio and Wireless Conference*, 2001, pp. 5-8.

[Win02] M. Z. Win and R. A. Scholtz,"Characterization of Ultra-Wideband Indoor Wireless Channels: A Communication theoretic view. *IEEE J. Select. Areas Commun.*, vol. 20, No. 9, Dec.2002.

[Yano02] S.M. Yano, "Investigating the Ultra-Wideband Wireless Channel," *IEEE 55th Vehicular Technology Conference*, pp. 1200–1204, May 2002.

[Yang04] L. Yang, "The Applicability of the Tap-Delay Line Channel Model to Ultra Wideband," Master's Thesis, Dept. of Electrical and Computer Engineering, Virginia Tech, Blacksburg, VA, 2004.

Vita

Vivek Bharadwaj was born in Bombay (Mumbai), India on August 14, 1980. He obtained a Bachelors degree in Electronics and Telecommunications Engineering from the University of Bombay in June 2002. In the same year, he was awarded the J.N Tata Endowment scholarship for pursuing higher studies abroad. From Aug 2002 to July 2004 he attended Virginia Polytechnic Institute and State University where he worked towards his Masters in Electrical Engineering, his advisor being Dr. R. Michael Buehrer. He was part of the MPRG group since February 2003. Since July 2004 he has been working with Qualcomm Inc. in San Diego, California in the WCDMA ASIC Performance group.